Study of the Effects of Inhibition of Epigenetic Regulators on the Proliferation of Hematological Malignant Tumor Cells

January 2021

Kazuhide NAKAYAMA

Study of the Effects of Inhibition of Epigenetic Regulators on the Proliferation of Hematological Malignant Tumor Cells

A Dissertation Submitted to

the Graduate School of Science and Technology,

University of Tsukuba

in Partial Fulfillment of Requirements

for the Degree of Doctor of Philosophy in Science

Doctorial Program in Biology,

Degree Programs in Life and Earth Sciences

Kazuhide NAKAYAMA

Table of Contents

Abstract

Epigenetics is the study of changes in gene function and expression that are heritable and that are not accompanied by alterations of the DNA sequence. The epigenetic modification consists of specific covalent modifications of chromatin components, which include DNA methylation and post-translational histone modifications. DNA methylation in promoter region represses gene expression by recruiting transcriptional repressor proteins or by inhibiting the binding of transcription factors to DNA. Histone modifications including methylation, acetylation, phosphorylation and ubiquitylation can modulate chromatin structure and hence influence gene expression, though the effect of these modifications on gene expression is largely context dependent. It is well known that genetic aberrations, such as point mutations, chromosomal mutations or changes in the gene copy number play an important role in cancer cell initiation and progression. In addition, recent growing evidences have indicated that the vast majority of human cancers harbor not only genetic, but also epigenetic abnormalities. Targeting these epigenetic aberrations in an attempt to restore a more normal condition seems an important treatment strategy for cancer. In fact, there are the large amount of effort that has been directed towards the development of epigenetics-targeting anti-cancer drugs. A few drugs targeting epigenetic enzymes have been approved by U.S. Food and Drug Administration (FDA), and a wide range of epigenetics-targeted drugs are undergoing clinical trials.

To investigate novel therapeutic strategies that modulate epigenetic dysregulation in cancer cells, I have researched lysine specific demethylase 1 (LSD1) and protein arginine methyltransferase 4 (PRMT4) as anti-cancer drug targets. In part 1, I investigated a synergistic interaction between LSD1 inhibitor, T-3775440, and NEDD8-activating enzyme (NAE) inhibitor, pevonedistat, in acute myeloid leukemia (AML) cells, highlighting the molecular mechanisms underlying the synergy and robust *in vitro* and *in vivo* antileukemic effects. In part 2, I found TP-064, which was a potent, selective, and cell-active chemical probe of human PRMT4 and its anti-proliferative activity in multiple myeloma (MM) cells. These results suggest that simultaneous suppression of LSD1 and NAE activities and suppression of PRMT4 activity can serve as novel therapeutic strategies for the treatment of AML and MM, respectively.

Abbreviations

ADMA	asymmetric dimethylarginine
AML	acute myeloid leukemia
ASH1L	ASH1-like histone lysine methyltransferase
BAFF155	BRG1-associated factor 155
CARM1	coactivator associated arginine methyltransferase 1
CDT1	Chromatin licensing and DNA replication factor 1
CEBPA	CCAAT/enhancer-binding protein alpha
CI	combination index
CoREST	REST corepressor
CRISPR	clustered regularly interspaced short palindromic repeats
CRL	cullin-RING E3 ubiquitin ligase
CUL4	cullin-4
DDB1	DNA damage-binding protein 1
DMSO	dimethyl sulfoxide
DNMT	DNA methyltransferase
DOT1L	DOT1-like histone H3K79 methyltransferase
DSLS	differential static light scattering
DTL	denticleless protein homolog
EZH2	enhancer of zeste homolog 2
FDA	U.S. Food and Drug Administration
Fbxw7	F-box/WD repeat-containing protein 7
γ H2AX	phosphorylated H2A histone family member X
GAPDH	glyceraldehyde 3-phosphate dehydrogenase
GATA1	GATA-binding factor 1
GFI1	growth factor independent 1
GFI1B	growth factor independent 1B

GLP	G9a-like protein
HDAC1	histone deacetylase 1
KDM1A	lysine (K)-specific demethylase 1A
KLF1	kruppel-like factor 1
LSD1	lysine-specific demethylase
MDS	myelodysplastic syndrome
MED12	mediator complex subunit 12
MLL	mixed-lineage leukemia
MM	multiple myeloma
MMA	monomethylarginine
NAE	NEDD8-activating enzyme
Nedd8	neural precursor cell expressed developmentally down-regulated protein 8
NRF2	nuclear factor erythroid 2-related factor 2
NSD	nuclear receptor binding SET domain protein
PARP	poly ADP-ribose polymerase
PRDM9	PR domain zinc finger protein 9
PRMT	protein arginine methyltransferase
PTM	post-translational modification
SAM	S-adenosyl-L-methionine
SAH	S-adenosyl-L-homocysteine
SCF	Skp, Cullin, F-box protein
SDMA	symmetric dimethylarginine
SETD	SET domain
SETDB1	SETD bifurcated 1
SMYD	SET and MYND domain-containing
SPA	scintillation proximity assay
SPR	surface plasmon resonance

SUV39H	suppressor of variegation 3-9 homolog
SUV420H	suppressor of variegation 4-20 homolog
UHRF1	ubiquitin-like with PHD and RING finger domains 1

General introduction

Epigenetics is generally referred to as the study of changes in gene function and expression that are mitotically and/or meiotically heritable and that do not include a change in DNA sequence. The epigenetic modification consists of specific covalent modifications of chromatin components, which include DNA methylation and post-translational histone modifications. Such epigenetic modifications result in alteration of chromatin structure and subsequent activation or inactivation of a gene's expression [1].

The most widely studied mechanism of epigenetic regulation is DNA methylation, the covalent addition of methyl groups to the fifth carbon on the cytosine base within the CpG islands of the promoter region of a gene, which catalyzed by DNA methyltransferases. DNA methylation represses gene expression by recruiting transcriptional repressor proteins or by inhibiting the binding of transcription factors to DNA [2]. Histones, the component of nucleosomes that are the building blocks of chromatin, can be acetylated, methylated, phosphorylated or ubiquitylated. These modifications can modulate chromatin structure by altering non-covalent interactions within and between nucleosomes. They also serve as binding sites for "reader" proteins with unique domains which specifically recognize these modifications. Enzymes which regulate the post-translational modifications (PTMs) of histones include histone acetyltransferase, histone deacetylase, histone methyltransferase, histone demethylase, kinases, E3-ubiquitin, etc. [3]. It is generally thought that the summation of all these PTMs determines the chromatin structure and biological outcome. The effects of the histone modifications are largely context dependent, as the same combination of marks may result in distinct biological outcomes at different genes within the same cells [4].

Cancer is the second leading cause of death among the most common diseases globally, accounting for an estimated 9.6 million deaths in 2018 [5]. Historically, cancer was mostly considered as a genetic disease, that is, a progressive series of genetic aberrations are thought to be the root cause of cancer cell initiation and progression. Specific gene mutations including oncogenes and tumor suppressor genes have been considered as the main causes of cancer [6]. A point mutation, a chromosomal mutation or a change in the gene copy number can lead to the oncogene activation by its enhanced expression or enhanced function. For example, TP53 tumor suppressor gene, which plays an

important role in regulation of cell cycle, apoptosis and genomic stability, is the most well-known mutated gene identified in human cancers [7].

Recent growing evidences have indicated that the vast majority of human cancers harbor not only genetic, but also epigenetic abnormalities. Large-scale cancer genome sequencing efforts have revealed that almost half of human cancers bear mutations in the genes encoding chromatin proteins including chromatin modifiers [8]. In addition, malignant cells show CpG islands hypermethylation, mostly in tumor suppressor genes, a reduction of total DNA methylation, and progressive changes in histone modifications [9]. It was recently hypothesized that these epigenetic aberrations and chromatin states may cause extensive oncogenic gain of function properties and may influence all of the hallmarks of cancer [10]. Targeting these aberrations in an attempt to restore a more normal epigenetic condition seems a viable treatment strategy for cancer. In fact, there are the large amount of effort that has been directed towards the development of epigenetics-targeting anti-cancer drugs. A few drugs targeting epigenetic enzymes, such as DNA methyl transferase and histone acetyl transferase, have been approved by FDA, and a wide range of epigenetics-targeted drugs are undergoing clinical trials [11].

To investigate novel therapeutic strategies that modulate epigenetic dysregulation in cancer cells, I have researched LSD1 and PRMT4 as anti-cancer drug targets. In part 1, I described a synergistic interaction between lysine specific demethylase 1 (LSD1) inhibitor, T-3775440 and NEDD8-activating enzyme (NAE) inhibitor, pevonedistat in acute myeloid leukemia (AML) cells, highlighting the molecular mechanisms underlying the synergy and robust *in vitro* and *in vivo* antileukemic effects. In part 2, I described the discovery of TP-064, which was a potent, selective, and cell-active chemical probe of human protein arginine methyltransferase 4 (PRMT4) and its anti-proliferative activity in multiple myeloma (MM) cells. These results suggest that simultaneous suppression of LSD1 and NAE activities and suppression of PRMT4 activity can serve as novel therapeutic strategies for the treatment of AML and MM, respectively.

Part 1

Synergistic anti-AML effects of the LSD1 inhibitor T-3775440 and the NEDD8-activating enzyme inhibitor pevonedistat via transdifferentiation and DNA rereplication

Abstract

Lysine-specific demethylase 1A (LSD1, KDM1A) specifically demethylates di- and monomethylated histones H3K4 and K9, resulting in context-dependent transcriptional repression or activation. I previously identified an irreversible LSD1 inhibitor T-3775440, which exerts antileukemic activities in a subset of acute myeloid leukemia (AML) cell lines by inducing cell transdifferentiation. The NEDD8-activating enzyme inhibitor pevonedistat (MLN4924, TAK-924) is an investigational drug with antiproliferative activities in AML, and is also reported to induce cell differentiation. I therefore tested the combination of these two agents in AML models. The combination treatment resulted in synergistic growth inhibition of AML cells, accompanied by enhanced transdifferentiation of an erythroid leukemia lineage into granulomonocytic-like lineage cells. In addition, pevonedistat-induced rereplication stress during the S phase was greatly augmented by concomitant treatment with T-3775440, as reflected by the increased induction of apoptosis. I further demonstrated that the combination treatment was markedly effective in subcutaneous tumor xenograft models as well as in a disseminated model of AML, leading to tumor eradication or prolonged survival in T-3775440/pevonedistat cotreated mice. These findings indicate the therapeutic potential of the combination of LSD1 inhibitors and pevonedistat for the treatment of AML.

Introduction

Acute myeloid leukemia (AML) is a highly aggressive hematological disorder caused by the malignant transformation of hematopoietic stem cells or myeloid progenitor cells, and is also the most common form of adult acute leukemia. Approximately 19,950 new cases are reported annually in the United States and the 5-year survival is reported to be 26% [12]. Despite advances in the understanding of this disease, the therapeutic strategy has changed little in recent decades. The standard induction chemotherapy comprises 7 days of cytarabine plus 3 days of anthracyclines (7+3 regimen), followed by consolidation of high-dose chemotherapy or stem cell transplantation. Despite intensive therapy, the relapsed/refractory disease rate remains a significant clinical problem. Therefore, novel therapeutic options are urgently needed.

Lysine-specific demethylase 1A (LSD1) is the first histone demethylase that had been discovered and specifically demethylates histone H3K4 and H3K9. This enzyme serves as a transcriptional corepressor or coactivator, depending on the target gene context [13, 14]. LSD1 functions as part of a multiprotein complex with corepressor proteins such as CoREST and histone deacetylase 1 (HDAC1) [15, 16]. It is overexpressed in a diverse set of solid tumors as well as hematopoietic malignancies [17, 18]. Selective small-molecule inhibitors for LSD1 have been reported to show antitumor efficacy in AML [19, 20, 21]. I have previously found that a novel LSD1 inhibitor, T-3775440, inhibits the growth of acute erythroid leukemia and acute megakaryoblastic leukemia cells through enforced transdifferentiation from their original lineages to a myeloid-like lineage [22]. Given the novel mechanism of action of LSD1 inhibitors, there is a growing interest in potential combinations of LSD1 inhibitors with chemotherapeutics or molecular targeting agents for the treatment of AML. In preclinical models, for example, an LSD1 inhibitor synergistically reduced AML cell viability in combination with cytarabine (Ara-C), a DNA-damaging agent widely used with daunorubicin as standard care for AML [21]. LSD1 inhibitors also showed synergistic antileukemic effects in combination with an HDAC inhibitor or all-trans retinoic acid in AML cell lines [23, 24].

Pevonedistat is an investigational drug that targets NEDD8-activating enzyme (NAE), leading to the suppression of Cullin-RING E3 ubiquitin ligase (CRL) activity [25, 26]. Many CRL substrate proteins have pivotal roles in cell cycle, DNA damage repair, and differentiation, making NAE a promising anticancer target [27, 28]. Pevonedistat exhibits significant antitumor activity in multiple preclinical models, including AML [29]. Notably, single agent clinical activity of pevonedistat has been investigated in AML/myelodysplastic syndrome (MDS) [30]. Several studies have been done to maximize the clinical activity of pevonedistat by combining it with DNA-damaging agents, such as cisplatin, for treating solid tumors [31, 32]. Pevonedistat triggers the cell cycle checkpoint in S phase and DNA rereplication, leading to cancer cell death [33]. In addition to its role in cell cycle machinery, pevonedistat promotes myeloid differentiation of AML cells, leading to antileukemic effects in a xenograft model [34]. These findings led me to examine the effect of combination treatments of an LSD1 inhibitor and pevonedistat in AML.

Materials and Methods

Cell culture and reagents

The human AML cell line TF-1a was purchased from the American Type Culture Collection (ATCC, Manassas, VA, USA; CRL-2451) in 2008. TF-1a cells and their derivatives were cultivated in RPMI1640 medium containing 10% fetal bovine serum, and maintained in an incubator at 37°C and 5% CO_2. Culture methods for other cell lines are available in Table 1. TF-1a and MOLM-16 were authenticated by short tandem repeat DNA profiling in 2016. Mycoplasma test was performed by Central Institute for Experimental Animals (Kawasaki, Japan) and all cell lines were confirmed to be negative for mycoplasma. A cytarabine-resistant TF-1a (TF-1a/Ara-C) cell line was developed from parental TF-1a cells by stepwise exposure to increasing concentrations of cytarabine. The resulting TF-1a/Ara-C cells were highly resistant to cytarabine (half-maximal inhibitory concentration value >10 μm) compared with the parental TF-1a cells (half-maximal inhibitory concentration value=0.053 μm). The LSD1 inhibitor T-3775440 and the NAE inhibitor pevonedistat were synthesized by Takeda Pharmaceutical Company (Fujisawa, Japan; Cambridge, MA, USA).

Establishment of TF-1a-luc stable cell line

TF-1-a cells were seeded into 6-well plates and left overnight to attach in media containing 0.1% fetal bovine serum. pGL-CMV-luc plasmids were transfected using FuGene HD transfection reagent (Promega, Madison, WI, USA) according to the manufacturer's instructions, at reagent-to-DNA ratios of 5:2. After transfection, cells were cultured in growth medium without antibiotics for 2 days and then in medium containing 350 μg/ml G418 (Life Technologies, Waltham, MA, USA) for selection. Stable clone cell mixtures (1×10^2), obtained following 3 weeks of selection, were reseeded in 6-well dishes with methylcellulose-based semisolid medium (ClonaCell-TCS medium; Stemcell Technologies, Vancouver, BC, Canada) containing 350 μg/ml G418 to select for transformed clones. After 1–2 weeks, individual colonies were picked and grown in 96-well plates with TCS medium

containing G418. The clone with the highest luciferase activity was selected and expanded for further experiments.

Cell proliferation assay

Cells were plated in tissue culture plates and test compounds were added simultaneously. After the treatment period, cells were lysed with CellTiter Glo (Promega) and the luminescent signal was measured using an ARVO MX1420 Microplate Reader (Perkin-Elmer, Waltham, MA, USA).

Analysis of drug combination effects

Calculation of combination metrics was performed as described previously [35]. Briefly, a nine- parameter response surface model was fitted to the relationship between normalized viability and drug concentration, after which an isobologram analysis was used to determine the effects of drug combinations [36]. To quantify the combined effects of the two drugs, the combination index (CI) with the concentrations of the single agents and combination that gave a normalized viability of 50% was computed [37, 38]. A CI value below 0.7 was classified as synergy, whereas a value above 1.3 was classified as subadditivity. A value in the range 0.7–1.3 was considered as additivity. Where the maximum inhibition by a single agent was <50%, nonlinear blending [39] were computed to determine the synergy. A blending value above 20 was classified as synergy, whereas a value above −20 was classified as antagonism.

Western blotting

Whole-cell extracts or immunoprecipitates were treated with 1 × Laemmli sample buffer (Tris-HCl 125 mM, pH 7.5, 1% sodium dodecyl sulfate, 20% glycerol) and were subejected to the sodium dodecyl sulfate–polyacrylamide gel electrophoresis. Fructionated proteins were then transferred to nitrocellulose membranes using an iBlot Transfer Stack and iBlot Gel Transfer Device (Thermo Fisher Scientific, Waltham, MA, USA). After incubation with StartingBlock T20 (phosphate-buffered saline) blocking buffer (Pierce Biotechnology, Waltham, MA, USA), membranes were labeled

with primary antibodies overnight, followed by incubation with horseradish peroxidase-conjugated secondary antibodies (Cell Signaling Technology, Danvers, MA, USA). Membranes were incubated with ImmunoStar Zeta (Wako, Osaka, Japan) and signals were detected using ImageQuant LAS-3000 (Fujifilm, Tokyo, Japan).

The following antibodies were used for western blotting analysis: CDT1 (sc-365305; Santa Cruz Biotechnology, Dallas, TX, USA), cleaved PARP (9541; Cell Signaling Technology), γH2AX (2577; Cell Signaling Technology), GAPDH (2118; Cell Signaling Technology), GATA1 (3535; Cell Signaling Technology), PU.1 (2258; Cell Signaling Technology), and c-Jun (9165; Cell Signaling Technology).

Cell cycle analysis

For measurement of DNA content to assess cell cycle distribution, cells were incubated with 70% ethanol/phosphate-buffered saline (v/v) overnight. Fixed cells were stained with propidium iodide and analyzed using a FACSCalibur or FACSVerse System (Becton-Dickinson, Franklin Lakes, NJ, USA).

Quantitative reverse transcription–polymerase chain reaction analysis and microarray

Following the designated treatment, total RNA was isolated from cells and purified using an RNeasy Mini Kit (Qiagen, Hilden, Germany). Reverse transcription (RT) reactions were performed using a Verso cDNA Synthesis Kit (Thermo Fisher Scientific). Quantitative real-time PCR analysis was performed with a ViiA7 System (Applied Biosystems, Foster City, CA, USA) and TaqMan Fast Advanced Master Mix with TaqMan probes against indicated genes (Applied Biosystems). The 2–ΔΔCt method was applied to analyze the data, using GAPDH mRNA expression as an internal control. The normalized abundance of target mRNAs was expressed relative to the corresponding value for cells treated with dimethyl sulfoxide (DMSO) or negative control siRNAs. The following TaqMan probes were used for quantitative RT–PCR (RT–PCR) analysis: LSD1 (KDM1A, Hs01002741_m1),

GFI1B (Hs01062469_m1), GFI1 (Hs01115757_m1), DTL (DTL, Hs00978565_m1), and GAPDH (Hs02758991_g1).

For microarray analysis, total RNA was purified as described above and the quality of RNA was verified using an Agilent 2100 Bioanalyzer (Agilent Technologies, Santa Clara, CA, USA). RNA was labeled and hybridized to Agilent SurePrint G3 Human Gene Expression 8 × 60 K arrays by Macrogen Company (Seoul, South Korea). Microarray data have been deposited in NCBI GEO (accession number: GSE89637). To examine transcriptome data at the level of gene signatures, gene set enrichment analysis was applied to the microarray data [40]. The reference signatures used in the analysis were generated from data published elsewhere [41].

siRNA transfection

The following siRNAs targeting each gene were obtained: siCTRL (D-001810-10; Dharmacon, Lafayette, CO, USA), LSD1 no. 1 (L-009223-00; Dharmacon), LSD1 no. 2 (118783; Ambion, Waltham, MA, USA), GFI1B no. 1 (s15850; Ambion), GFI1B no. 2 (s15851; Ambion), GFI1 no. 1 (s5706; Ambion), GFI1 no. 2 (s5707; Ambion), and DTL (s28248; Ambion). siRNAs were transfected into cells using GenomeONE-Si (Ishihara Sangyo, Osaka, Japan), or formulated into lipid-based nanoparticles.

Subcutaneous tumor xenograft models

All animal experiments were conducted in compliance with the guidelines of the Takeda Institutional Animal Care and Use Committee (IACUC; approval number, AU-00006241) in a facility accredited by the American Association for Accreditation of Laboratory Animal Care (AAALAC). Female C.B17/Icr-scid/scid Jcl mice (CLEA Japan, Tokyo, Japan) were maintained under specific pathogen-free conditions. AML cells were subcutaneously inoculated with Matrigel into the left flank of 6- to 7-week-old mice (day 0). Mice were randomized when the mean tumor volume reached ~120–180 mm^3. Mice were then treated with vehicle, T-3775440 (per os), pevonedistat (subcutaneous), cytarabine (intraperitoneal), azacitidine (subcutaneous) or combination treatment. Tumor volume was

measured twice weekly using Vernier calipers and calculated as (length × width^2) × 0.5. The percentage treated/control ratio (T/C %) was calculated by dividing the change in tumor volume in the treated mice by the change in volume in mice administered vehicle. Statistical comparisons were carried out using the one-tailed Williams' test or Aspin–Welch's t-test ($P<0.025$ or $P<0.05$ were considered statistically significant, respectively).

AML cell dissemination model

As a dissemination model, TF-1a-luc cells were inoculated via the tail vein into 7-week-old female NOG (NOD.Cg-Prkdcscid Il2rgtm1Sug/Jic) mice (1×10^6 cells per mouse, day 0). The mice (CLEA) were maintained under specific pathogen-free conditions and used in compliance with the guidelines of the Takeda IACUC (approval number, AU-00010345). Administration of T-3775440 alone (per os), pevonedistat alone (subcutaneous), T-3775440/pevonedistat in combination or vehicle was initiated 10 days after cell inoculation (day 10). Leukemic cell growth was monitored based on emitted bioluminescence (photons/s) 10 min after intraperitoneal administration of d-luciferin (150 mg/kg) using the *In Vivo* Imaging System (Xenogen, Waltham, MA, USA). Mice reaching the humane end points were killed. Statistical analysis was performed by a log-rank test using prism (GraphPad Prism Software, La Jolla, CA, USA).

Statistical analysis

The *in vitro* experiments were performed in duplicate or triplicate. Statistical significance was determined using multiple comparison procedures, such as Dunnett's multiple comparison test, as described in the figure legends. A log-rank test was performed to compare survival curves ($P<0.00555$ after the Bonferroni correction was considered statistically significant). GraphPad Prism Software (Version 5; GraphPad Software Inc., La Jolla, CA, USA) was used for the analyses.

Results

Combination of T-3775440 and pevonedistat synergistically inhibits AML cell growth

To analyze the interaction between T-3775440 and pevonedistat in AML cell proliferation, I performed *in vitro* combination studies in a series of AML cell lines. As shown in Table 2 and Figure 1, synergistic effects were observed in seven cell lines out of 15 and additive effects were observed in another seven cell lines, suggesting that this combination has a broad anti-AML spectrum. In contrast, T-3775440 had little effect on pevonedistat-mediated growth inhibition of CCRF-CEM and MOLT-3 (acute lymphoblastic leukemia cell lines), RPMI8226 and KMS28BM (multiple myeloma cell lines) or HepG2 (a hepatocellular carcinoma cell line), suggesting that the combination effects were specific for AML cells (Figure 2). Since the growth inhibition curve and isobologram indicated a clear synergism in TF-1a erythroloid leukemic cells (Figure 3a and b, and Table 3) and cytarabine-resistant TF-1a/Ara-C cells (Table 2 and Figures 1a and 4), I also evaluated the combination effects of T-3775440 with cytarabine, daunorubicine and azacitidine, which are used for the treatment of AML and/or MDS, in TF-1a cells (Figure 3c and Figure 5). T-3775440 exhibited synergistic effects with all agents tested. Among them, pevonedistat exhibited the greatest synergism in combination with T-3775440 in TF-1a cells (FAB-M6) as well as in Kasumi-1 cells (FAB-M2) with a combination index (CI) of 0.30 (Figures 1b and c) and 0.45 (Figure 6), respectively.

GFI1B inhibition by T-3775440 is involved in the combination effects with pevonedistat in TF-1a cells

LSD1 inhibits lineage-specific gene expression by forming transcription repressive complexes with several transcription factors, including CoREST and GFI1B [16]. The interaction between LSD1 and GFI1B is reported to be responsible for erythroid and megakaryocytic lineage specification [16, 42]. I have recently reported that the antileukemic activity of T-3775440 is mediated by its ability to disrupt the LSD1-GFI1B interaction in GFI1B-expressing AML cells, which leads to derepression of myeloid lineage genes and subsequent cell transdifferentiation [22]. To test whether

the combination effect of T-3775440 and pevonedistat was dependent on the disruption of the LSD1-GFI1B axis, LSD1 and GFI1B expressions were perturbed using small interfering RNA (siRNA) in the presence of pevonedistat in GFI1B-expressing TF-1a cells (Figure 3d). LSD1 or GFI1B knockdown derepressed the expression of GFI1, a target gene of the LSD1-GFI1B transcription repressive complex, at a level equal to the effect of T-3775440 (Figure 3d and Figure 7) [43] and significantly lowered the half-maximal effective concentration value of pevonedistat compared with that of the control (Figure 3e and Table 4). In contrast, knockdown of GFI1 did not alter the effect of pevonedistat on the viability of TF-1a cells. These results suggest that inhibition of LSD1-GFI1B by T-3775440 is involved in its synergistic interaction with pevonedistat.

T-3775440 enhances rereplication stress induced by pevonedistat, leading to apoptosis

Pevonedistat is known to induce DNA rereplication and DNA damage in cancer cells [44]. Hence, in order to determine whether T-3775440 affected the rereplication phenotype induced by pevonedistat treatment, I analyzed cell cycle profiles of cell treated with those drugs. T-3775440 treatment alone moderately increased the number of cells in the sub-G1 fraction, whereas pevonedistat treatment caused dysregulation of the cell cycle progression triggered by DNA rereplication (Figure 8a). The combination of these two agents significantly increased the cell population in the sub-G1 fraction, indicating potentiated apoptotic cell death (Figure 8a). To confirm that cell death was via apoptosis due to DNA damage, I performed western blot analyses. As a single agent, neither T-3775440 nor pevonedistat affected the expression levels of γH2AX and cleaved PARP, markers for double-strand DNA damage and apoptosis, respectively (Figure 8b). In contrast, cotreatment with T-3775440 and pevonedistat significantly increased the signal intensity of γH2AX as well as the cleaved form of PARP (Figure 8b). Apoptotic cell death induced by the combination was also confirmed by the amount of cleaved caspase-3 and caspase-3/7 activities (Figures 9a and b), while no clear additive or synergistic effects on proteins involved in the DNA damage response pathway, such as phospho-MCM2, FANCD2, phosho-Chk1 and Chk2, were observed with the cotreatment (Figure 9c). It has been reported that pevonedistat induces rereplication via inhibition of the ubiquitin ligase CUL4-

DDB1DTL and subsequent CDT1 accumulation, and that knockdown of DTL mimics the S-phase effect of pevonedistat [44]. Indeed, pevonedistat induced accumulation of CDT1 (Figure 8b) as well as other Cullin-RING ligase substrates p27 (Figure 9c) and NRF2 (data not shown). Therefore, I tested the effect of cotreatment with T-3775440 and DTL siRNA, which resulted in significant apoptotic cell death compared with perturbation alone, mimicking the synergistic apoptosis-inducing effect of T-3775440/pevonedistat combined treatment (Figure 8c, Figure 10 and Table 5). These results suggest that AML cells under rereplication stress are highly vulnerable to T-3775440 treatment.

Cotreatment with T-3775440/pevonedistat cooperatively induces transdifferentiation of erythroid leukemia cells

It has previously been reported that T-3775440 leads to differentiation of AML cells and thereby induces cell growth arrest and apoptosis [22]. Pevonedistat induces not only DNA rereplication-mediated genotoxic stress but also triggers the differentiation of AML cells [34]. I therefore examined how cotreatment with these two agents affects transcriptional networks that regulate lineage specificity in TF-1a erythroid leukemia cells. Microarray and gene set enrichment analysis revealed that treatment with T-3775440 or pevonedistat alone downregulated erythroid cell gene expression but upregulated neutrophilic cell gene expression (Figures 11a and b). Cotreatment with these two agents further augmented the degree to which the erythroid and neutrophilic gene signatures were depleted and enriched, respectively, as evidenced by the greater values of negative and positive enrichment scores. Consistent with the results from the gene set enrichment analysis, the expression of several representative erythroid and neutrophil marker genes was more significantly downregulated and upregulated, respectively, by the combination treatment than by treatment with either agent alone (Figures 12a and b). These results suggest that this combination cooperatively promoted transdifferentiation in the same direction, from the erythroid lineage to the myeloid-like lineage.

GATA1 is a master transcription factor responsible for erythroid lineage maintenance and commitment, while PU.1 is the counterpart for myeloid lineage [45]. Erythroid and myeloid lineage

commitment is regulated by the balance in activities of these two transcription factors. Thus, I examined the expression levels of these factors in TF-1a cells following treatment with T-3775440 alone, pevonedistat alone or the combination of both. The combination treatment decreased GATA1 levels to a greater extent than did either agent alone in TF-1a cells and in MOLM-16, a megakaryoblastic leukemia cell line (Figure 11c and Figure 12c). It also decreased KLF1 levels, which is a direct target of GATA1 in both cell lines (Figure 12c). In contrast, the effects of the combination as well as each single agent on PU.1 levels were modest. I next examined the protein expression level of c-Jun, a transcription cofactor known to enhance the transcriptional activity of PU.1. Consistent with previous reports that pevonedistat increases c-Jun by inhibiting SCF-type ubiquitin ligase Fbxw7-mediated degradation [46, 47], pevonedistat treatment increased c-Jun protein levels in TF-1a cells (Figure 11c). The PU.1 target genes CCAAT/enhancer binding protein α (CEBPA) and CD86 were additively upregulated by cotreatment with T-3775440 and pevonedistat (Figures 12d and e). These results suggest that T-3775440 and pevonedistat cooperatively promote cell differentiation by shifting the balance from GATA1 to PU.1/c-Jun in TF-1a cells.

To assess the durability of cotreatment-induced growth inhibition, a washout study in TF-1a cells were performed. After exposure to each agent alone or to the combination treatment, cells were replated into media free from either agent (Figure 11d). Pretreatment with T-3775440 alone did not significantly delay cell regrowth after washout, reflecting the cytostatic effect of T-3775440 at this concentration. Pretreatment with pevonedistat alone caused relatively durable cell growth inhibition up to 7 days after the washout. Cotreatment, however, demonstrated even more prolonged antiproliferative effects, with regrowth of cells not observed for almost 2 weeks.

Coadministration of T-3775440/pevonedistat exhibits significant antitumor activity in subcutaneous AML xenograft models

In vitro combination studies often overestimate the effect of combination treatment, as they do not consider potential dose reduction to mitigate adverse effects caused by coadministration. Therefore, we used AML xenograft mouse models to examine whether coadministration of T-

3775440/pevonedistat produced *in vivo* antitumor effects as observed *in vitro*. The combination of T-3775440 (15–20 mg/kg, orally, on a 5 days on/2 days off schedule) and pevonedistat (60–90 mg/kg, subcutaneously, three times per week on days 1, 3 and 5) was tolerated for 2 weeks (Figure 13a and Figures 14a and b). In a TF-1a subcutaneous tumor xenograft model, although treatment with each single agent exhibited a significant antitumor effect, tumors regrew shortly after cessation of treatment. The combination treatment, however, showed more significant antitumor effects during and even after the treatment period. Two mice out of six achieved complete tumor eradication, and all mice had no tumor recurrence throughout an extended observation period (until day 50). Such significant combination effects were also observed in mice that had received only a single cycle of coadministration, which consisted of 5 days of T-3775440 (20 mg/kg, days 1–5) and 2 days of pevonedistat (60 mg/kg, days 1 and 4) (Figures 15a and b). Furthermore, the potential of pevonedistat as a combination partner with T-3775440 was compared with that of cytarabine or azacitidine in the same xenograft models (Figures 13b and c). Although combinations with cytarabine or azacitidine resulted in significant tumor regression during the dosing period in the TF-1a models, neither of them achieved tumor eradication at the maximum-tolerated doses (Figures 14c–g). In addition, I examined the combination effect in a model of MOLM-16, a megakaryocytic leukemia cell line, where administration of each agent alone led to only modest tumor growth suppression, but where the combination resulted in sustained tumor regression during the dosing period (Figure 13d and Figure 14h).

Coadministration of T-3775440/pevonedistat reduces tumor burden and improves mouse survival in an erythroid leukemia dissemination model

To extend findings in subcutaneously implanted AML xenograft models as mentioned above, the combination effects of T-3775440/pevonedistat were further evaluated in a mouse dissemination model using TF-1a-luc cells, in which leukemic cell growth was monitored noninvasively via emitted bioluminescence. As shown in Figure 16a, tumor cells were disseminated into various organs, including the bone marrow and spleen, as early as 11 days after cell inoculation (day 11), and they

proliferated over the monitoring period in vehicle-treated mice (days 11–25). Whole-body luminescence increased ~300-fold during this time period (Figure 16b). T-3775440 significantly delayed tumor outgrowth in a dose-dependent manner over a dose range of 2.5–10 mg/kg, and even reduced tumor burden at 20 mg/kg (Figures 16a–c). Although pevonedistat itself showed little effect on tumor burden in this model, coadministration of T-3775440/pevonedistat led to a reduction in tumor burden, even when T-3775440 was combined at a low dose of 2.5 mg/kg (Figures 16b–d and Figures 17a and b). In parallel with the tumor burden changes, T-3775440 treatment significantly prolonged mouse survival compared with vehicle treatment (Figure 16e and Table 6). The combination of T-3775440/pevonedistat exhibited more significant prolongation of life than either agent used alone (Figure 16f and Table 6). Through extended time periods, 2 out of 10 mice that had received 20 mg/kg of T-3775440 and 60 mg/kg of pevonedistat had no detectable signal of tumor burden at day 133, suggesting that these mice achieved complete remission (Figure 17c). The drug treatment was generally tolerated, although one mouse out of nine died during the treatment period in the T-3775440 monotherapy group (20 mg/kg) and the T-3775440/pevonedistat combination groups, possibly due to hemorrhage following multiple injections of luciferin and/or pevonedistat in the context of T-3775440-induced thrombocytopenia. Despite this adverse effect observed in the model, the combination of T-3775440/pevonedistat exerted significant antileukemic effects that led to overall improved mouse survival.

Discussion

In this study, I demonstrated a synergistic interaction between the LSD1 inhibitor T-3775440 and the NAE inhibitor pevonedistat in various AML models. Cotreatment with these agents significantly suppressed AML cell growth *in vitro* and *in vivo*. Notably, intensive but short-term treatment with T-3775440/pevonedistat resulted in tumor eradication in subcutaneous xenograft models and prolonged survival in a cell-disseminated model of TF-1a erythroid leukemia. Some mice achieved long-term remission and a potential cure following the treatment. The combination of T-3775440 with pevonedistat showed superior activity to combinations with conventional chemotherapeutics such as cytarabine and daunorubicine. These data suggest that a T-3775440/pevonedistat combination regimen represents a novel strategy to treat resistant/refractory AML, beyond conventional cytarabine/anthracyclines '7+3' induction chemotherapy. However, the clinical relevance of the anti-AML effects of the combination needs to be further validated in studies that, for instance, use patient-derived primary AML cells.

The synergistic interaction between T-3775440 and pevonedistat appeared to be most promising in AML cells, despite the fact that the target molecules, LSD1 and NAE, are widely expressed in a range of cancer types. This may reflect the selective activity of the LSD1 inhibitor against AML. In particular, the acute erythroid leukemia cell line TF-1a was highly sensitive to the combination treatment both *in vitro* and *in vivo*. Erythroid leukemia cells express high levels of GFI1B protein, a SNAG domain-containing protein, which is involved in the lineage-specific transcription program through interactions with LSD1. I have shown previously that T-3775440 produces antileukemia effects by targeting a critical interaction between LSD1 and GFI1B transcription repressor in erythroid and megakaryoblastic leukemia cells [22]. In the present study, GFI1B knockdown potentiated the antileukemia effects of pevonedistat, mimicking the synergistic interaction between T-3775440 and pevonedistat. The lack of a synergistic interaction in the combination in non-AML cells can be explained by the low GFI1B expression in these cell types, which suggests few overlapping nonhematologic toxicities, such as hepatotoxicity [48], and a wide therapeutic window for

the combination. Thrombocytopenia appeared to be a dose-limiting toxicity of the combination in our preclinical models, although we believe that platelet transfusion would be a feasible approach to manage this adverse effect in clinical settings.

Cotreatment with T-3775440/pevonedistat significantly promoted the transdifferentiation of erythroid leukemia cells. This effect is most likely dependent on the ability of each agent to induce transdifferentiation in the same direction as the megakaryocytic–erythroid to granulocytic–monocytic lineage [22, 34]. Of note, the T-3775440/pevonedistat combination cooperatively decreased the expression of GATA1, a lineage-restricted transcription factor of erythroid and megakaryocytic cells [49]. GATA1 physically interacts with and inhibits the activity of the PU.1 transcription factor, a central regulator of myeloid differentiation, in a dose-dependent manner [50, 51, 52]. In contrast to a previous report wherein pevonedistat significantly increased PU.1 protein levels in MV-4–11 cells [34], each agent alone and the combination of T-3775440/pevonedistat only modestly affected PU.1 levels in TF-1a cells. Instead, pevonedistat treatment increased protein expression of c-JUN, a well-known substrate of SCF (SKP1, Cullin and F-box protein) E3 ubiquitin ligase [46, 53]. c-JUN cooperates with PU.1 and relieves GATA1-mediated repression of a myeloid transcription program [54, 55]. Indeed, cotreatment with T-3775440/pevonedistat led to significant expression of PU.1-dependent CEBPA and CD86 in TF-1a cells. These data suggest that these key transcription factors, which function in early myeloid linage selection, execute AML cell transdifferentiation induced by the T-3775440/pevonedistat combination.

Consistent with previous studies [33, 44], pevonedistat elicited DNA rereplication by stabilizing CDT1 in the S phase, leading to cell apoptosis. I demonstrated that this DNA rereplication-induced cell death was significantly augmented by T-3775440, not only in pevonedistat-treated cells but also in DTL-depleted cells, suggesting that AML cells under rereplication stress are highly susceptible to T-3775440 treatment. Mosammaparast et al. [56] reported that LSD1 was recruited to sites of DNA damage, preferentially in late S/G2 phase, and promoted ubiquitylation of H2A/H2AX, thus enabling a full DNA damage response [56]. Cotreatment with T-3775440/pevonedistat increased DNA double-strand breakage, as evidenced by γH2AX expression. These results suggest that LSD1

inhibition sensitizes cells to pevonedistat treatment by disabling the DNA damage response, although the exact mechanism has yet to be clarified. Recently, Zhou et al. [57] reported that the HDAC inhibitor belinostat showed synergistic anti-AML efficacy with pevonedistat by disrupting the DNA damage response. Since LSD1 and HDAC interact with each other through complex formation with CoREST in hematopoietic cells [16], it would be of interest to investigate whether similar modes of action operate with LSD1 and HDAC inhibitors in combination with pevonedistat.

In this article, I report that a synergistic interaction between the LSD1 inhibitor T-3775440 and the NAE inhibitor pevonedistat yielded significant anti-AML effects including complete remission in preclinical erythroid leukemia models. Erythroid leukemia is rare (2–4% of AML) but highly refractory to conventional chemotherapy; there is therefore a considerable unmet medical need for effective treatments. This data, including the antileukemic effects on erythroid leukemia containing cytarabine-resistant TF-1a cells, may be considered promising. Mechanistically, cotreatment with these two agents induced cell transdifferentiation cooperatively, thereby inhibiting cell proliferation. Moreover, pevonedistat-mediated rereplication contributed functionally to the combination with T-3775440 to promote cell death. Two other LSD1 inhibitors, ORY-1001 and GSK2879552, have undergone clinical trials for the treatment of patients with AML (EudraCT number: 2013-002447-29; ClinicalTrials.gov identifier: NCT02177812). Since pevonedistat has been reported to show modest clinical activity in a subset of AML patients [30], these findings indicate that the LSD1/NAE inhibitor combination strategy is worth consideration for the treatment of AML.

Figures and Tables

Figure 1

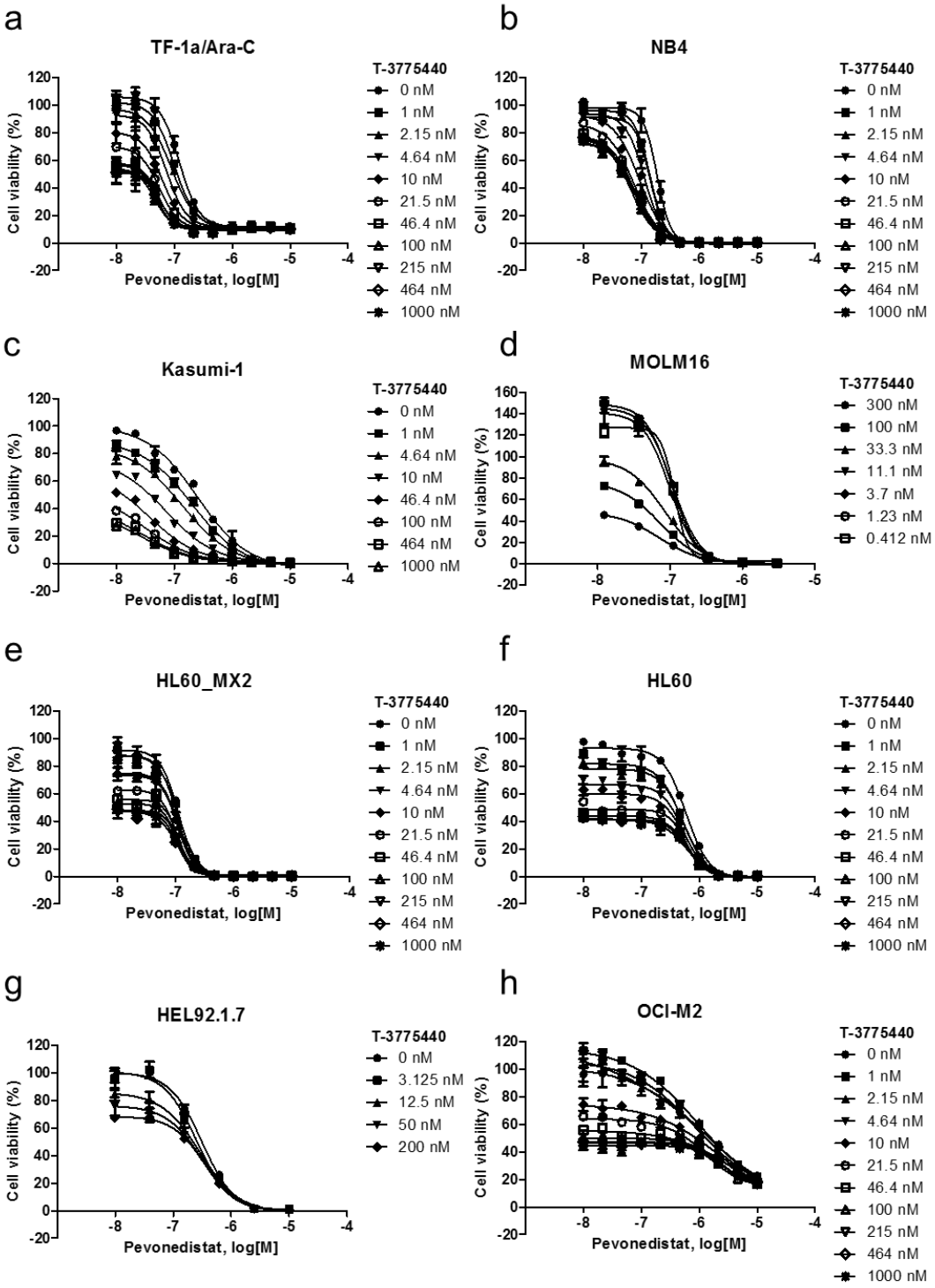

Figure 1, continued

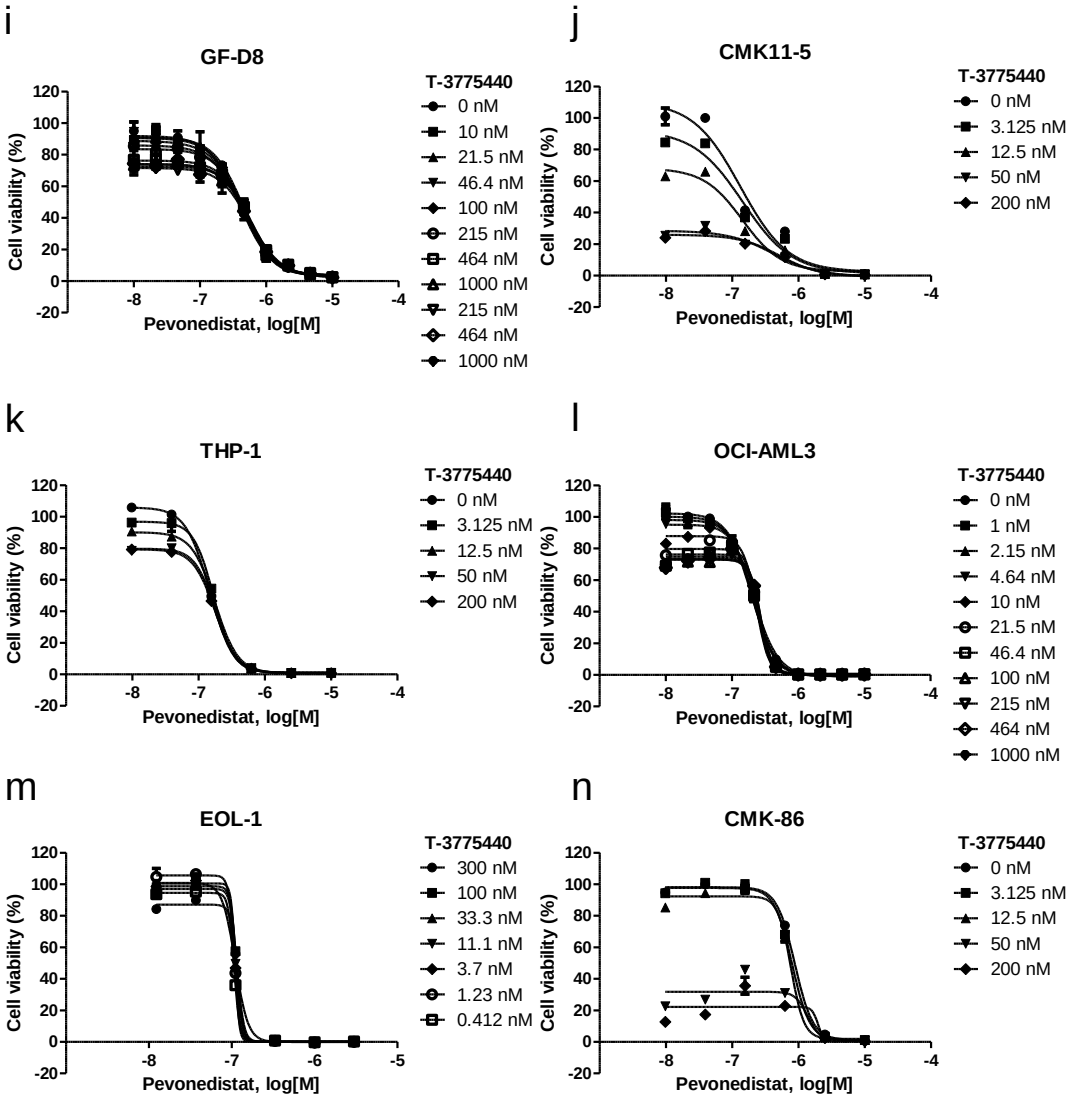

Figure 1. The combination effects of T-3775440 and pevonedistat in an AML cell panel.

(a–n) Cells were treated with pevonedistat in the presence or absence of T-3775440. Viability was measured using CellTiter Glo assay at the time points indicated in Supplementary Table 1. The experiments were performed in duplicate (a-c, e, f, h, i, l) or triplicate (d, g, j, k, m, n). *Values*, means; *bars*, SD.

Figure 2

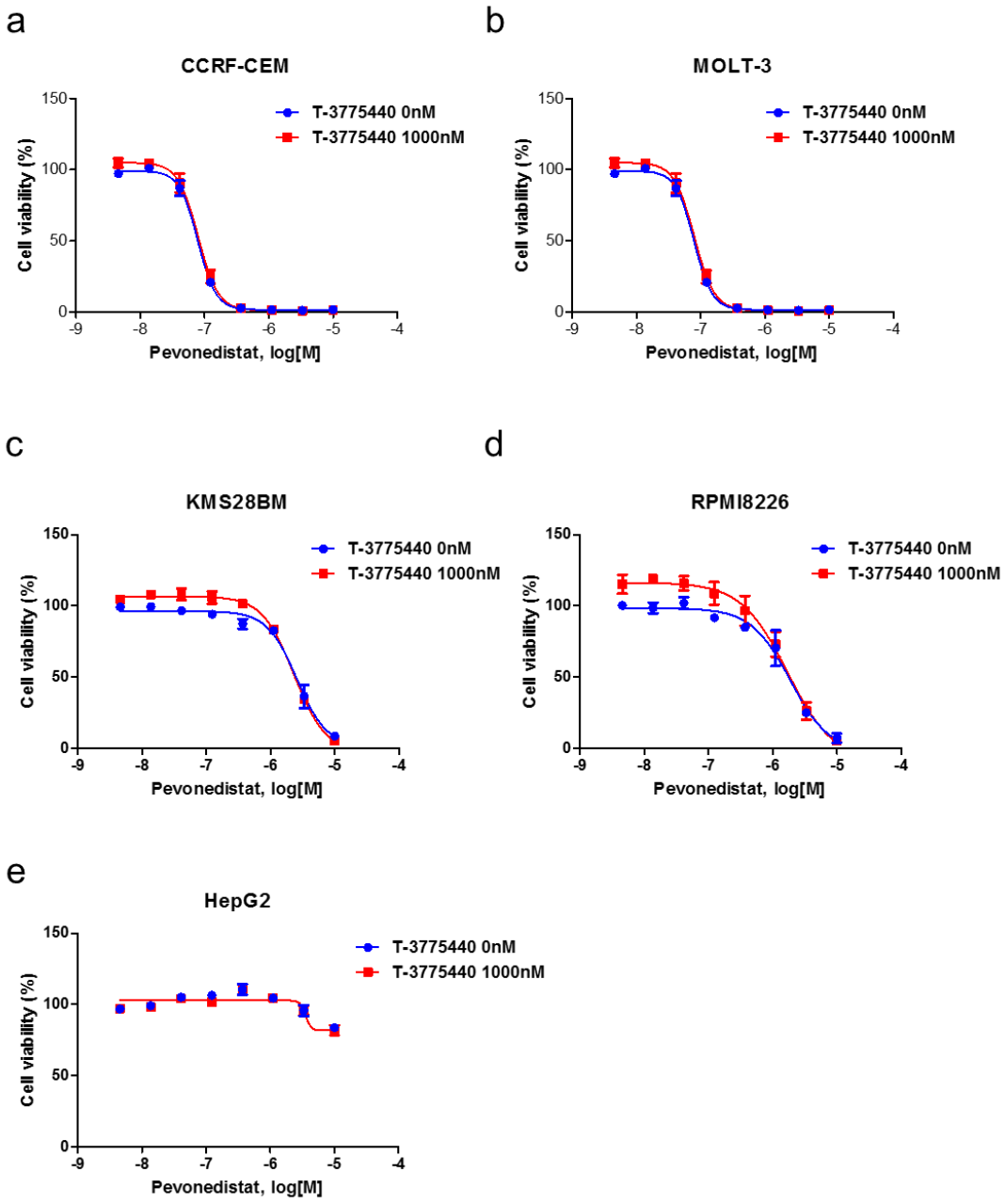

Figure 2. Effects of the T-3775440/pevonedistat combination in non-AML cell lines.

(a–e) Cells were treated with pevonedistat in the presence or absence of T-3775440. Viability was measured after 120 h of treatment in CCRF-CEM (a), MOLT-3 (b), KMS28BM (c), and RPMI8226 (d) cell lines. (e) For HepG2, viability was determined after 72 h of treatment. Experiments were performed in triplicate. *Values*, means; *bars*, SD.

Figure 3

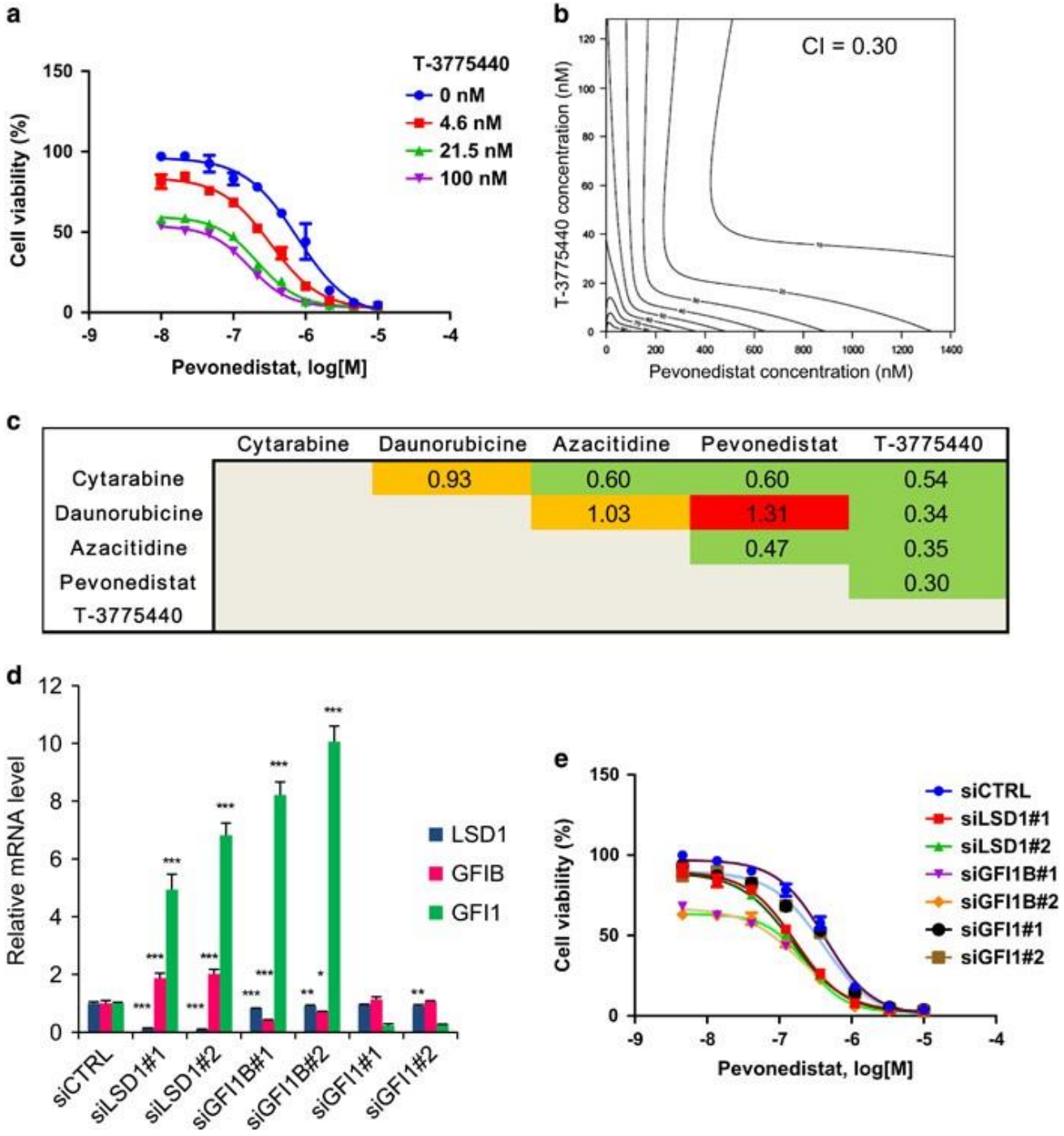

Figure 3. The combination of T-3775440 and pevonedistat shows synergistic growth inhibition of AML cell lines.

(a–c) TF-1a cells were cotreated with T-3775440 and pevonedistat or other anti-AML agents and the effects on cell viability were measured 72 h post treatment using the CellTiter Glo assay. The experiments were conducted in duplicate. (a) Representative growth curve of TF-1a cells. (b)

Isobologram of the cotreatment of TF-1a cells with T-3775440/pevonedistat. (c) Values represent the CI for each combination in TF-1a cells. Heat maps are color-coded based on the combination effects: green, synergy (CI values, <0.7); orange, additive (0.7–1.3); red, subadditive (>1.3). (d) TF-1a cells were treated with siRNA for 6 h and then replated. At 48 h after the initial treatment, total RNA was purified from the cells and used in quantitative reverse transcription–polymerase chain reaction (qRT–PCR) analyses. The values represent the means of triplicate samples ± SD. Statistical significance was determined using Dunnett's multiple comparison test (*P<0.05, **P<0.01, ***P<0.001). (e) TF-1a cells were treated with the indicated siRNA for 6 h and replated as in (d). After overnight incubation, cells were treated with pevonedistat for 72 h. Dose–response curve of cells treated with pevonedistat and siRNA is shown (n=3).

Figure 4

a

	Cytotoxicity [IC_{50} (nM)]	
Drugs	TF-1a	TF-1a/AraC
Cytarabine	53	>10,000
Decitabine	252	>10,000
Daunorubicin	86	58
Azacitidine	4370	5010

b

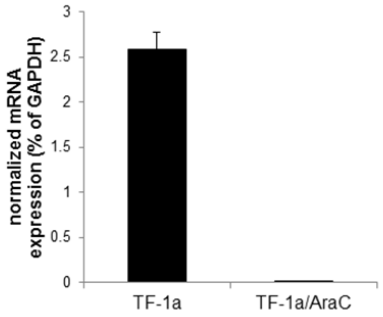

c

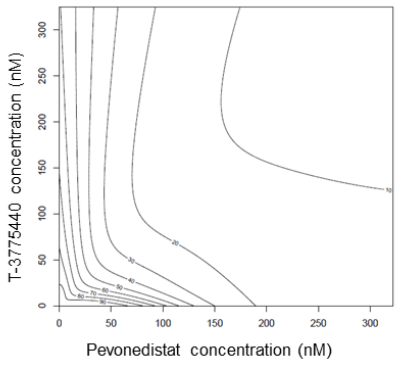

Figure 4. The combination effect of T-3775440 and pevonedistat in cytarabine-resistant TF-1a (TF-1a/AraC) cells.

The cytarabine-resistant TF-1a (TF-1a/Ara-C) cell line was developed from parental TF-1a cells by "stepwise" exposure to increasing concentrations of cytarabine. (a) TF-1a and TF-1a/AraC cells were treated with each compound and cell viability was measured 72 h later using a CellTiter Glo assay. The IC_{50} values shown (n = 4) were calculated using nonlinear regression analysis. The resultant TF-1a/Ara-C cells were highly resistant to cytarabine (IC_{50} > 10 μM) compared to the parental TF-1a cells (IC_{50} = 0.053 μM). The cross-resistance study revealed that TF-1a/Ara-C cells were as sensitive to

daunorubicin and azacitidine as the parental TF-1a cells were. Daunorubicin is a substrate of P-glycoprotein (P-gp), while azacitidine is a substrate of equilibrative nucleoside transporter 1 (hENT1). Therefore, the cytarabine resistance of TF-1a/AraC cells was thought to be independent of either overexpression of P-gP or loss of hENT1 function, which often confers drug resistance by decreasing the drug concentration in AML cells. In contrast, TF-1a/Ara-C cells showed cross-resistance to decitabine. (b) Since both decitabine and cytarabine require deoxycytidine kinase (DCK), a rate-limiting activating enzyme, to exert their anti-leukemic activities, we determined the expression level of DCK. The results revealed that DCK mRNA expression was undetectable in TF-1a/AraC cells. These data suggest that resistance to cytarabine and decitabine is conferred by a deficiency in the activation processes due to DCK downregulation. (c) Isobologram of the T-3775440/pevonedistat combination in TF-1a/AraC cells

Figure 5

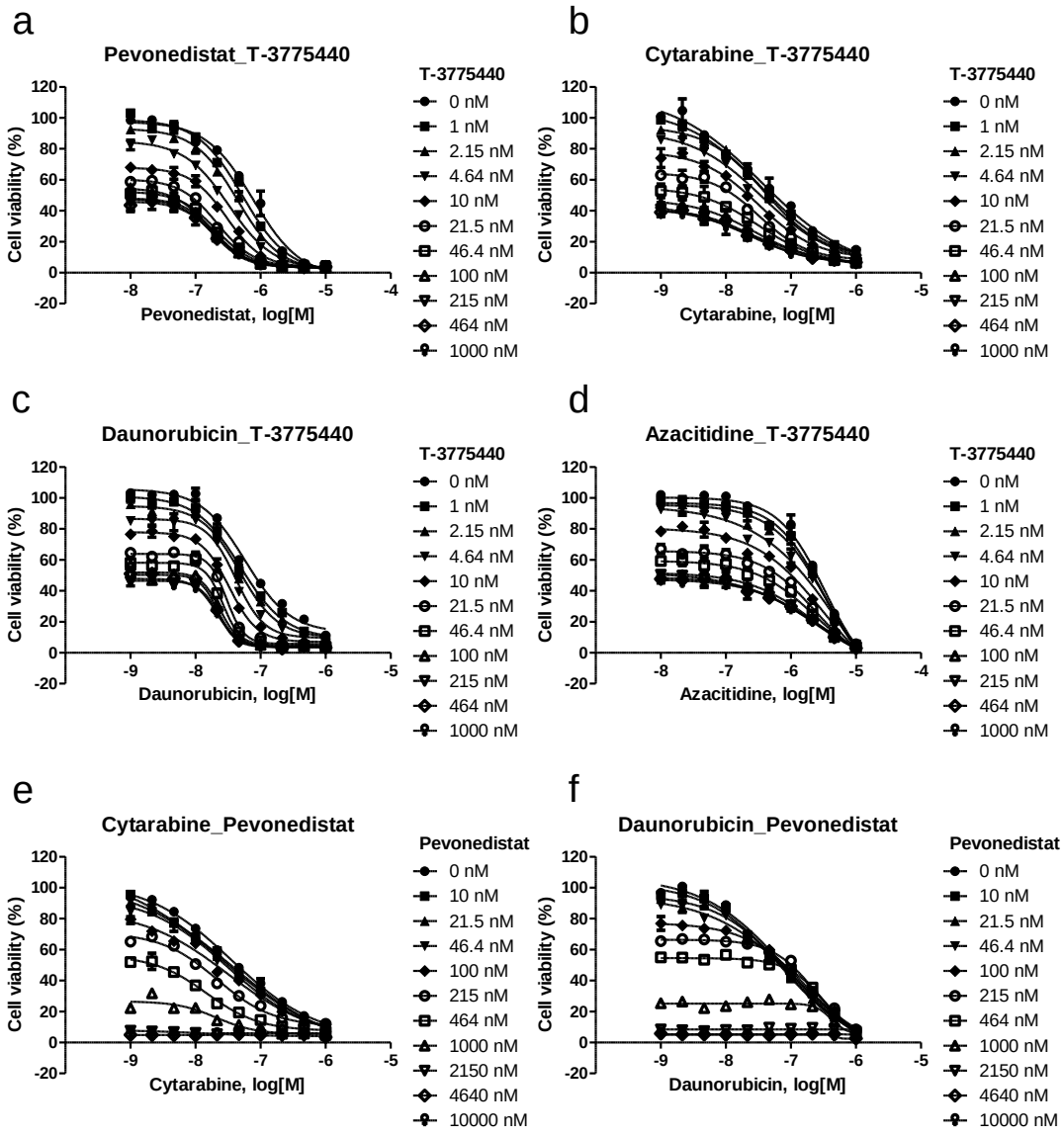
a
Pevonedistat_T-3775440
Cell viability (%)
Pevonedistat, log[M]
T-3775440
0 nM
1 nM
2.15 nM
4.64 nM
10 nM
21.5 nM
46.4 nM
100 nM
215 nM
464 nM
1000 nM
b
Cytarabine_T-3775440
Cell viability (%)
Cytarabine, log[M]
T-3775440
0 nM
1 nM
2.15 nM
4.64 nM
10 nM
21.5 nM
46.4 nM
100 nM
215 nM
464 nM
1000 nM
c
Daunorubicin_T-3775440
Cell viability (%)
Daunorubicin, log[M]
T-3775440
0 nM
1 nM
2.15 nM
4.64 nM
10 nM
21.5 nM
46.4 nM
100 nM
215 nM
464 nM
1000 nM
d
Azacitidine_T-3775440
Cell viability (%)
Azacitidine, log[M]
T-3775440
0 nM
1 nM
2.15 nM
4.64 nM
10 nM
21.5 nM
46.4 nM
100 nM
215 nM
464 nM
1000 nM
e
Cytarabine_Pevonedistat
Cell viability (%)
Cytarabine, log[M]
Pevonedistat
0 nM
10 nM
21.5 nM
46.4 nM
100 nM
215 nM
464 nM
1000 nM
2150 nM
4640 nM
10000 nM
f
Daunorubicin_Pevonedistat
Cell viability (%)
Daunorubicin, log[M]
Pevonedistat
0 nM
10 nM
21.5 nM
46.4 nM
100 nM
215 nM
464 nM
1000 nM
2150 nM
4640 nM
10000 nM

Figure 5, continued

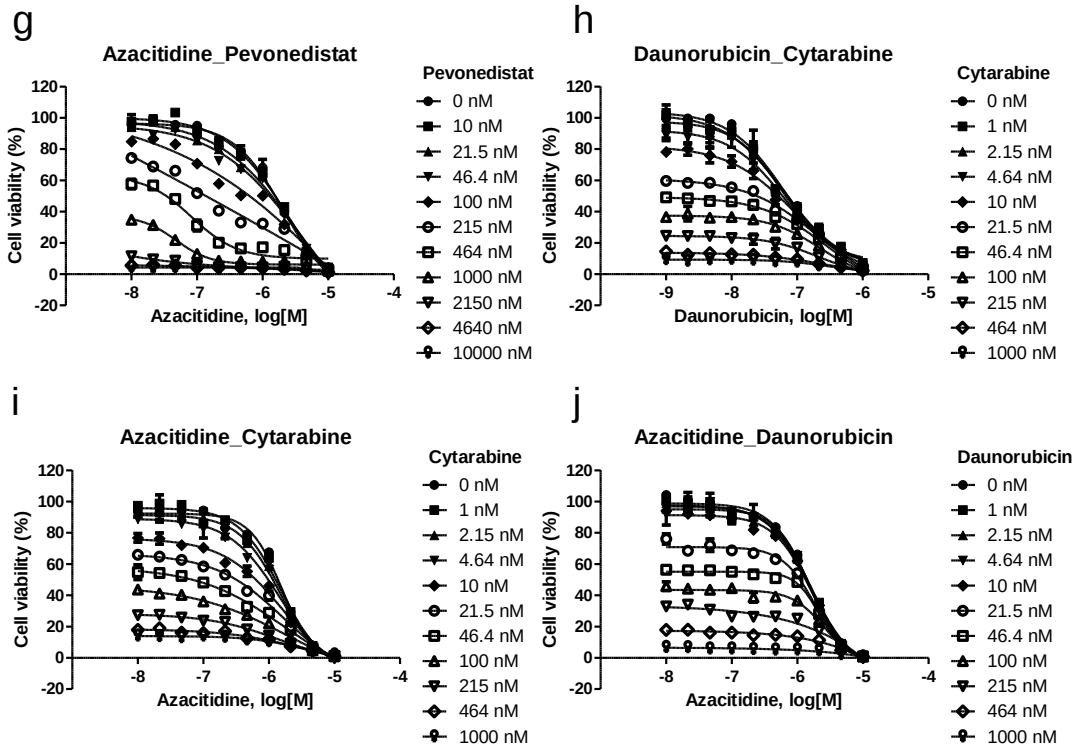

Figure 5. The combination effects of a panel of anti-leukemic agents in TF-1a cells.

(a–j) TF-1a cells were treated with the indicated combination of small molecule inhibitors. Viability was measured after 72 h of treatment using Cell Titer Glo. Experiments were performed in duplicate. *Values*, means; *bars*, SD.

Figure 6

a

	Cytarabine	Daunorubicine	Azacitidine	Pevonedistat	T-3775440
Cytarabine		1.18	0.81	0.73	0.58
Daunorubicine			1.13	1.02	0.66
Azacitidine				0.55	0.58
Pevonedistat					0.45
T-3775440					

b

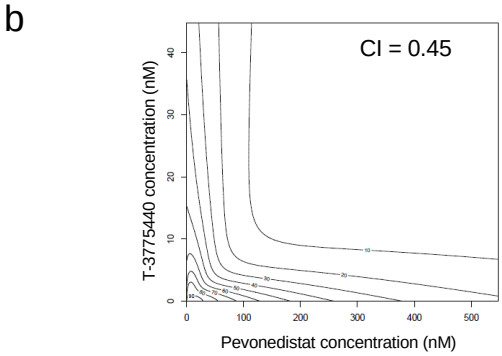

Figure 6. The combination of T-3775440 and pevonedistat shows synergistic growth inhibition of Kasumi-1 cells.

(a) Kasumi-1 cells were treated with each combination of agents and cell viability was measured after 120 h of treatment. Values represent the combination index (CI) for each combination. Experiments were performed in duplicate. (b) The isobologram of the cotreatment of T-3775440/pevonedistat in Kasumi-1 cells is shown.

Figure 7

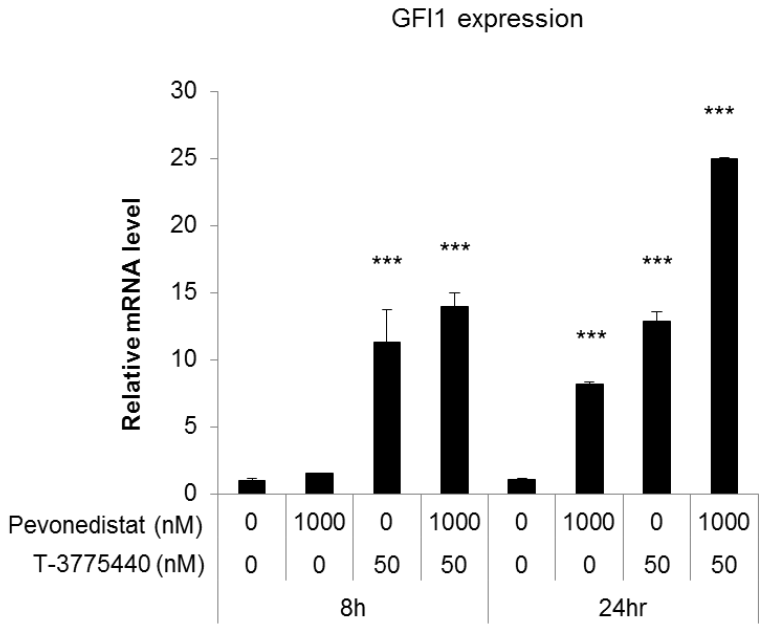

Figure 7. Cotreatment with T-3775440/pevonedistat augments GFI1 expression.

TF-1a cells were treated with dimethyl sulfoxide (DMSO), 1000 nM pevonedistat, 50 nM T-3775440, or pevonedistat and T-3775440 in combination for 8 or 24 h. Total RNA was purified from the cells and subjected to quantitative reverse transcription – polymerase chain reaction (qRT-PCR) analysis (n=2). Statistical significance was determined using Dunnett's multiple comparison test ($^{***}P < 0.001$). *Columns*, means; *bars*, SD.

Figure 8

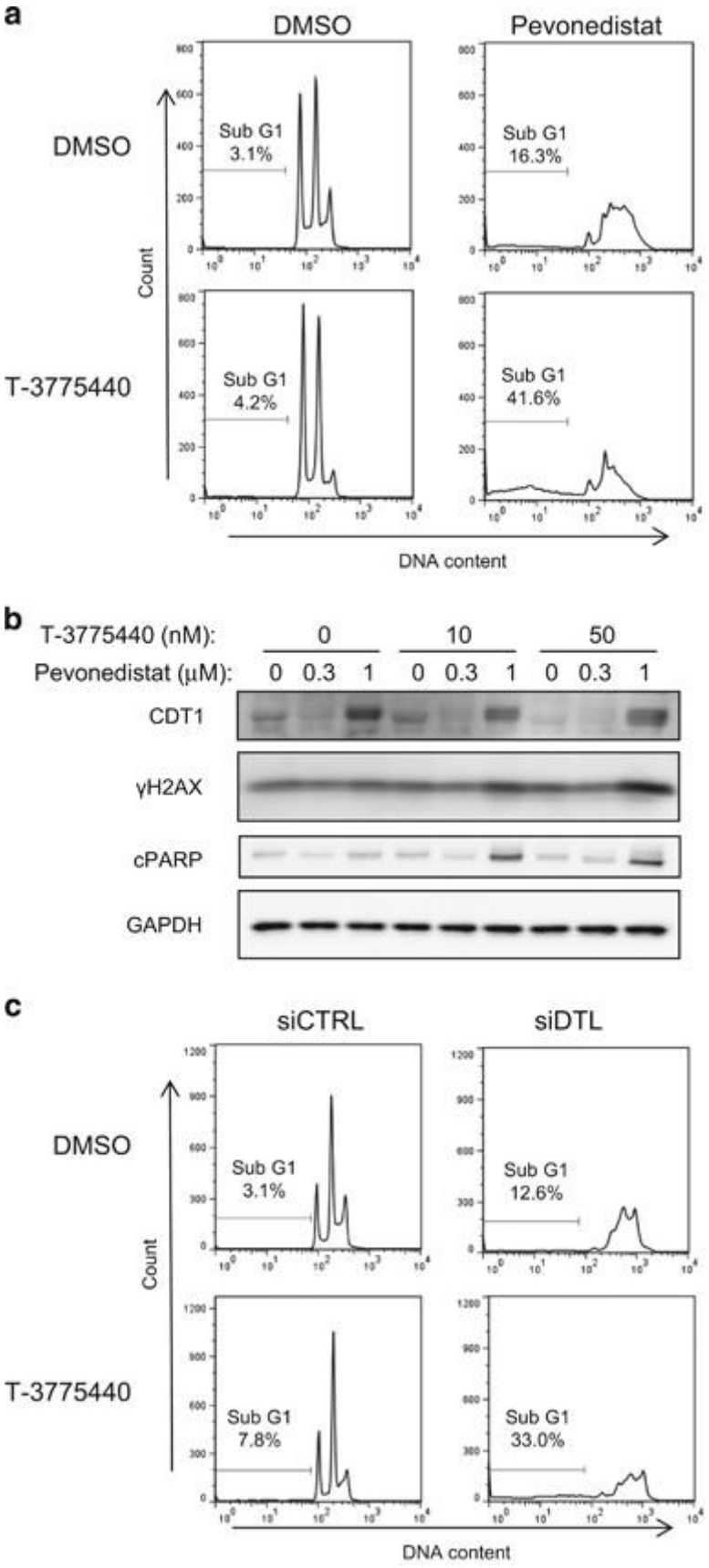
a
DMSO
Pevonedistat
DMSO
T-3775440
Sub G1
3.1%
Sub G1
16.3%
Sub G1
4.2%
Sub G1
41.6%
Count
DNA content
b
T-3775440 (nM):
0
10
50
Pevonedistat (μM):
0 0.3 1 0 0.3 1 0 0.3 1
CDT1
γH2AX
cPARP
GAPDH
c
siCTRL
siDTL
DMSO
T-3775440
Sub G1
3.1%
Sub G1
12.6%
Sub G1
7.8%
Sub G1
33.0%
Count
DNA content

Figure 8. T-3775440 enhances apoptotic cell death under pevonedistat- or DTL depletion-induced replication stress.

(a) TF-1a cells were treated with vehicle, 50 nM T-3775440, 1 μM pevonedistat, or T-3775440 and pevonedistat for 48 h. DNA content was determined by flow cytometry. Note that this cell line grows as a stable population of cells with N, 2N and 4N nuclear complements. Percentages of cells in the sub-G1 population are indicated. (b) Increased DNA damage and apoptosis after T-3775440 and pevonedistat treatment. TF-1a cells were treated with drugs or dimethyl sulfoxide (DMSO) control (as indicated) for 48 h. Immunoblotting analysis was performed to determine the expression levels of γH2AX and cleaved PARP. Glyceraldehyde 3-phosphate dehydrogenase (GAPDH) was used as a protein-loading control. (c) TF-1a cells were transfected with siRNA targeting DTL or control siRNA and incubated for 4 h. Next, cells were replated in the presence or absence of 50 nM T-3775440 for 48 h. Cell cycle analysis was performed using flow cytometry.

Figure 9

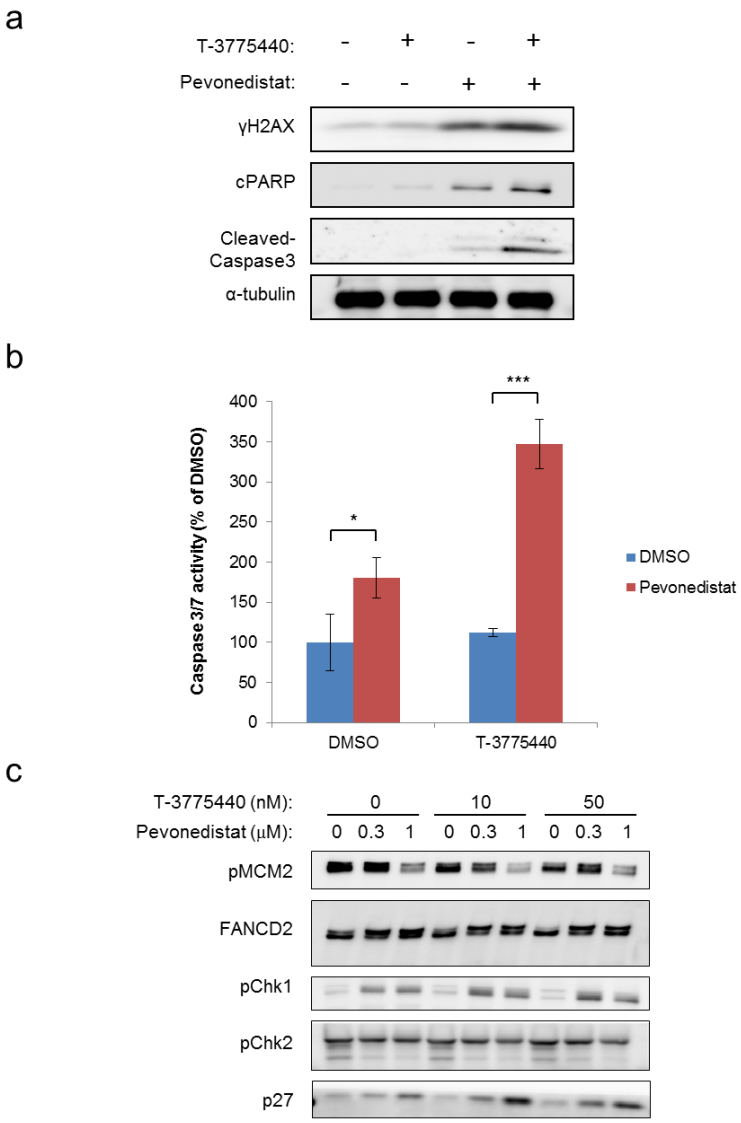

Figure 9. Apoptosis induction by co-treatment with T-3775440 and pevonedistat.

(a) TF-1a cells were treated with T-3775440 and pevonedistat as indicated for 48 h (T-3775440, 50 nM; Pevonedistat, 1 μM). Whole cell lysates were prepared and subjected to immunoblotting analysis. Alpha-Tubulin was used as a loading control. (b) TF-1a cells were treated as indicated (T-3775440, 50 nM; Pevonedistat, 100 nM). After 24 h treatment, caspase 3/7 activities were determined using a Caspase-Glo kit (Promega). *Columns*, means; *bars*, SD. n = 3. Bonferroni post hoc test following analysis of variance (ANOVA) was used for the statistical analyses ($^{*}P < 0.05$, $^{***}P < 0.001$). (c) TF-1a cells were treated with drugs or dimethyl sulfoxide (DMSO) control for 48 h. Immunoblotting analysis was performed to determine the expression levels of indicated proteins.

Figure 10

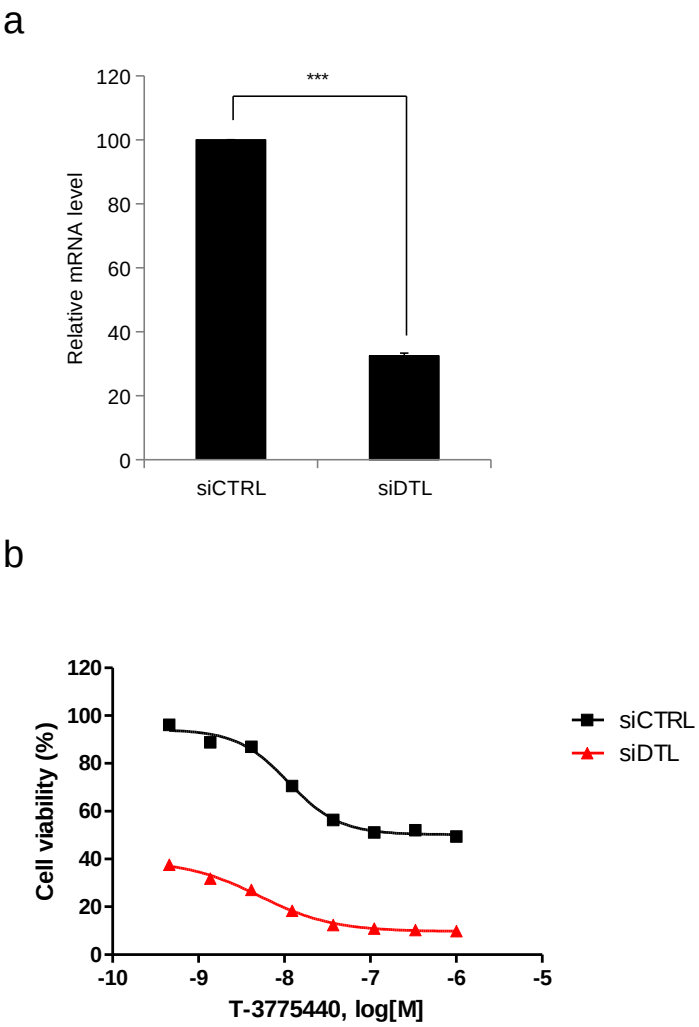

Figure 10. Knockdown of DTL sensitizes TF-1a cells to T-3775440-induced cell growth inhibition. (a) TF-1a cells were treated with siRNA against DTL or control for 4 h. Forty-eight hours after the initial siRNA treatment, cells were harvested for RNA purification. Changes in *DTL* expression were measured by quantitative reverse transcription-polymerase chain reaction (qRT-PCR). The values represent the means of duplicate samples ± SD. Unpaired t test was employed for statistical analysis ($^{***}P < 0.001$). (b) The effects of siRNA targeting DTL on T-3775440-induced growth inhibition in TF-1a cells. Cells were treated with siRNA against DTL or control for 4 h, and after overnight incubation, cells were treated with T-3775440 or dimethyl sulfoxide (DMSO) control for 72 h. Viability was expressed as cell proliferation relative to the siCTRL/DMSO cotreatment control.

Figure 11

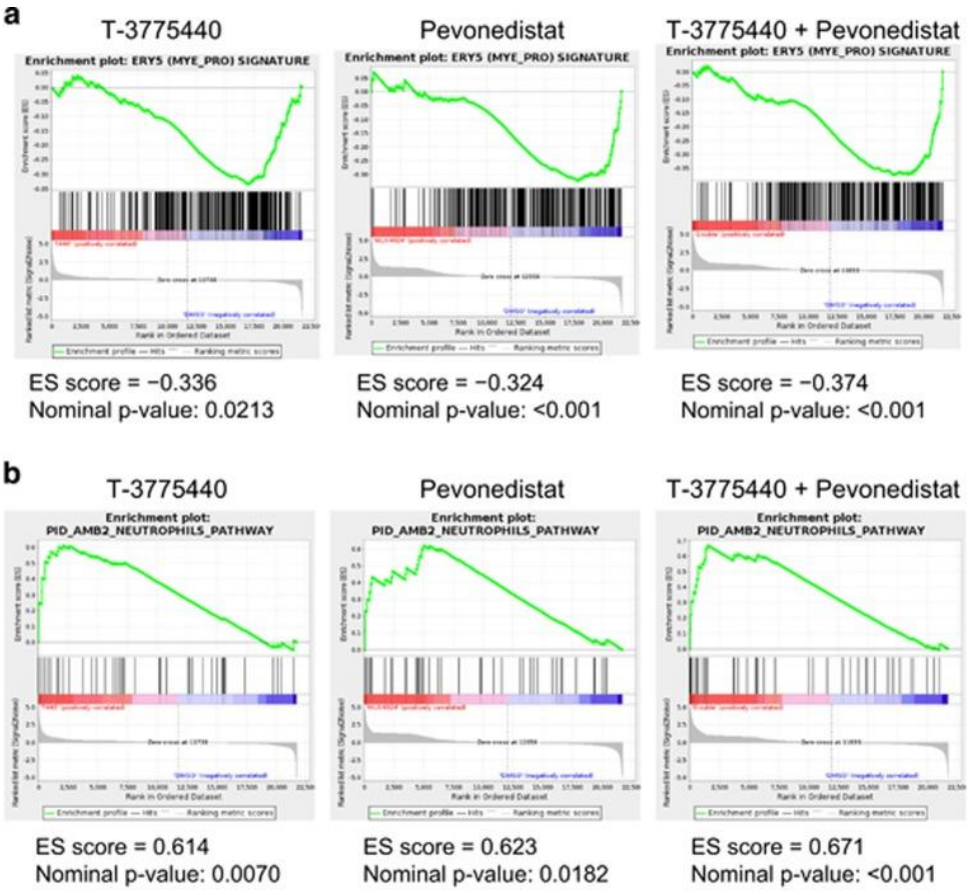
a
T-3775440
Pevonedistat
T-3775440 + Pevonedistat
Enrichment plot: ERY5 (MYE_PRO) SIGNATURE
ES score = −0.336
Nominal p-value: 0.0213
ES score = −0.324
Nominal p-value: <0.001
ES score = −0.374
Nominal p-value: <0.001
b
T-3775440
Pevonedistat
T-3775440 + Pevonedistat
Enrichment plot:
PID_AMB2_NEUTROPHILS_PATHWAY
ES score = 0.614
Nominal p-value: 0.0070
ES score = 0.623
Nominal p-value: 0.0182
ES score = 0.671
Nominal p-value: <0.001
c
T-3775440: - + - +
Pevonedistat: - - + +
GATA1
c-Jun
PU.1
GAPDH
d
T-3775440 (nM)
0
50
Pevonedistat (nM)
0
300
1000
Ratio to Day 0
Days after treatment
0
5
10
15
20
25

Figure 11. Cotreatment with T-3775440/pevonedistat results in AML cell transdifferentiation and durable growth suppression.

(a, b) TF-1a cells were treated with vehicle, 50 nM T-3775440, 1 μM pevonedistat or T-3775440 and pevonedistat in combination for 24 h. Total RNA was used for microarray analysis. Gene set enrichment plots demonstrate the downregulation of erythroid signature genes (a) and upregulation of neutrophil signature genes (b). (c) TF-1a cells were treated with T-3775440 and pevonedistat as indicated. Whole-cell lysates were prepared and subjected to immunoblotting analysis. Glyceraldehyde 3-phosphate dehydrogenase (GAPDH) was used as a loading control. (d) Cell proliferation assay after washout of compounds. TF-1a cells were treated with the indicated drugs alone or in combination for 72 h. Cells were then replated in the absence of the compounds and proliferation rates were determined using CellTiter Glo assay (n=3).

Figure 12

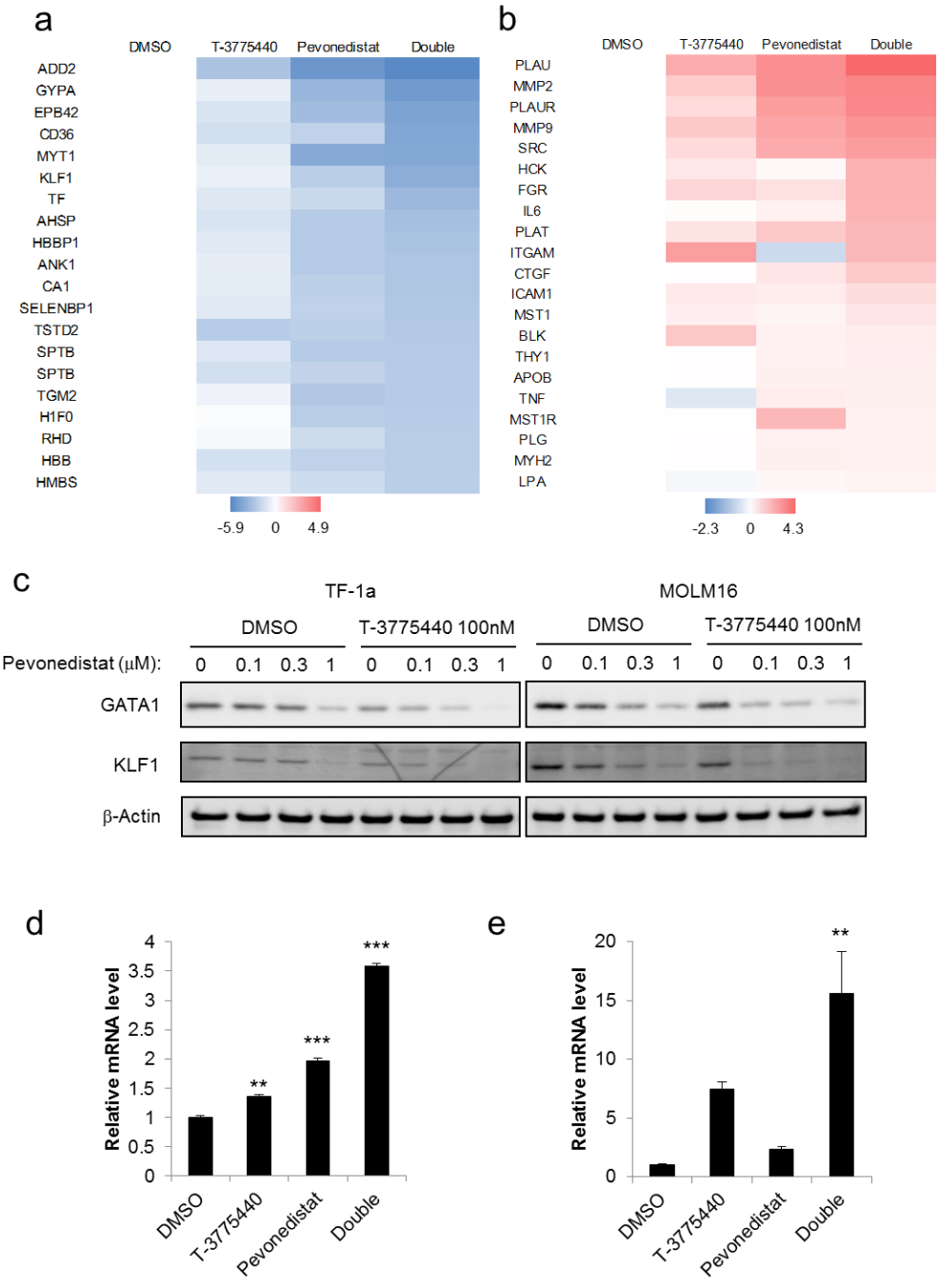

Figure 12. Cotreatment with T-3775440 and pevonedistat modulates the expression of differentiation-associated genes.

(a, b, d, e) TF-1a cells were treated with vehicle, 50 nM T-3775440, 1 μM pevonedistat, or T-3775440 and pevonedistat in combination for 24 h. Total RNA was subjected to microarray analysis. A heat map shows fold changes in gene expression of erythroid signature genes (a) and neutrophil signature genes

(b). Upregulated and downregulated genes relative to dimethyl sulfoxide (DMSO) control are represented as red and blue, respectively. (c) TF-1a or MOLM16 cells were treated with T-3775440 and pevonedistat as indicated for 24 h. Whole cell lysates were prepared and subjected to immunoblotting analysis. b-Actin was used as a loading control. (d) The mRNA expression level of CEBPA was obtained from the microarray analysis as in (a). (e) Cotreatment with T-3775440/pevonedistat augments each drug-induced CD86 expression. TF-1a cells were treated with DMSO, 300 nM pevonedistat, 10 nM T-3775440, or pevonedistat and T-3775440 in combination for 24 h. Total RNA was purified from the cells and subjected to quantitative reverse transcription – polymerase chain reaction (qRT-PCR) analysis. Bonferroni's multiple comparison test was employed ($^{**}P < 0.01$, $^{***}P < 0.001$).

Figure 13

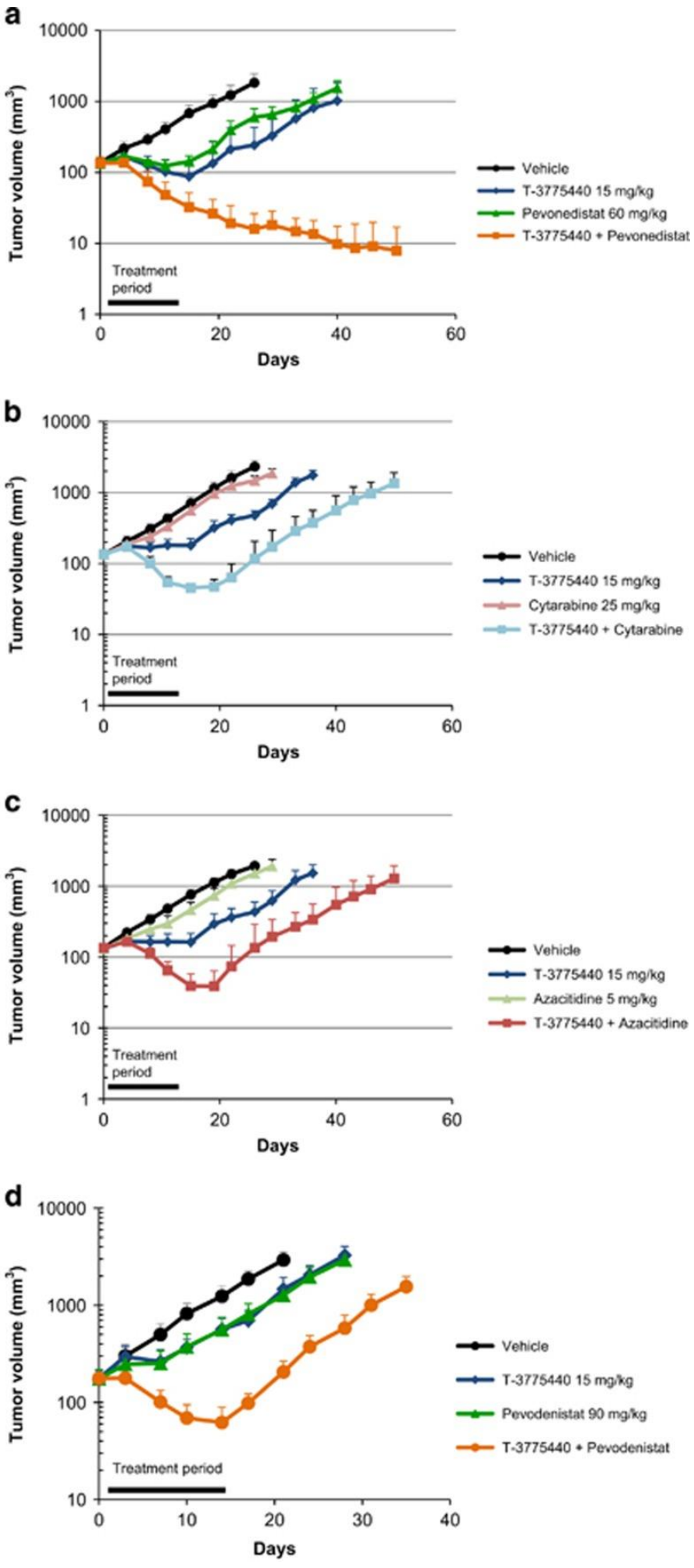
a
Tumor volume (mm³)
10000
1000
100
10
1
Treatment period
0
20
40
60
Days
Vehicle
T-3775440 15 mg/kg
Pevonedistat 60 mg/kg
T-3775440 + Pevonedistat
b
Tumor volume (mm³)
Treatment period
Days
Vehicle
T-3775440 15 mg/kg
Cytarabine 25 mg/kg
T-3775440 + Cytarabine
c
Tumor volume (mm³)
Treatment period
Days
Vehicle
T-3775440 15 mg/kg
Azacitidine 5 mg/kg
T-3775440 + Azacitidine
d
Tumor volume (mm³)
Treatment period
0
10
20
30
40
Days
Vehicle
T-3775440 15 mg/kg
Pevodenistat 90 mg/kg
T-3775440 + Pevodenistat

Figure 13. The T-3775440/pevonedistat combination exhibits significant anti-AML effects in subcutaneous xenograft models.

(a–c) Antitumor effects of T-3775440 in combination with pevonedistat (a), cytarabine (b) or azacitidine (c) were examined in TF-1a tumor subcutaneous models. Mice were subcutaneously (s.c.) inoculated in the flank with AML cells. Animals received T-3775440 once daily orally (p.o.) on a 5 days on/2 days off schedule, pevonedistat three times weekly (on days 1, 3 and 5, s.c.), cytarabine three times weekly (on days 1, 3 and 5, intraperitoneally (i.p.)), or azacitidine two times weekly (on days 1 and 4, s.c.). The values represent mean tumor volumes ± SEM (n=5). (d) Antitumor effects of the T-3775440/pevonedistat combination were examined in a MOLM-16 model with the same dosing schedule as in (a).

Figure 14

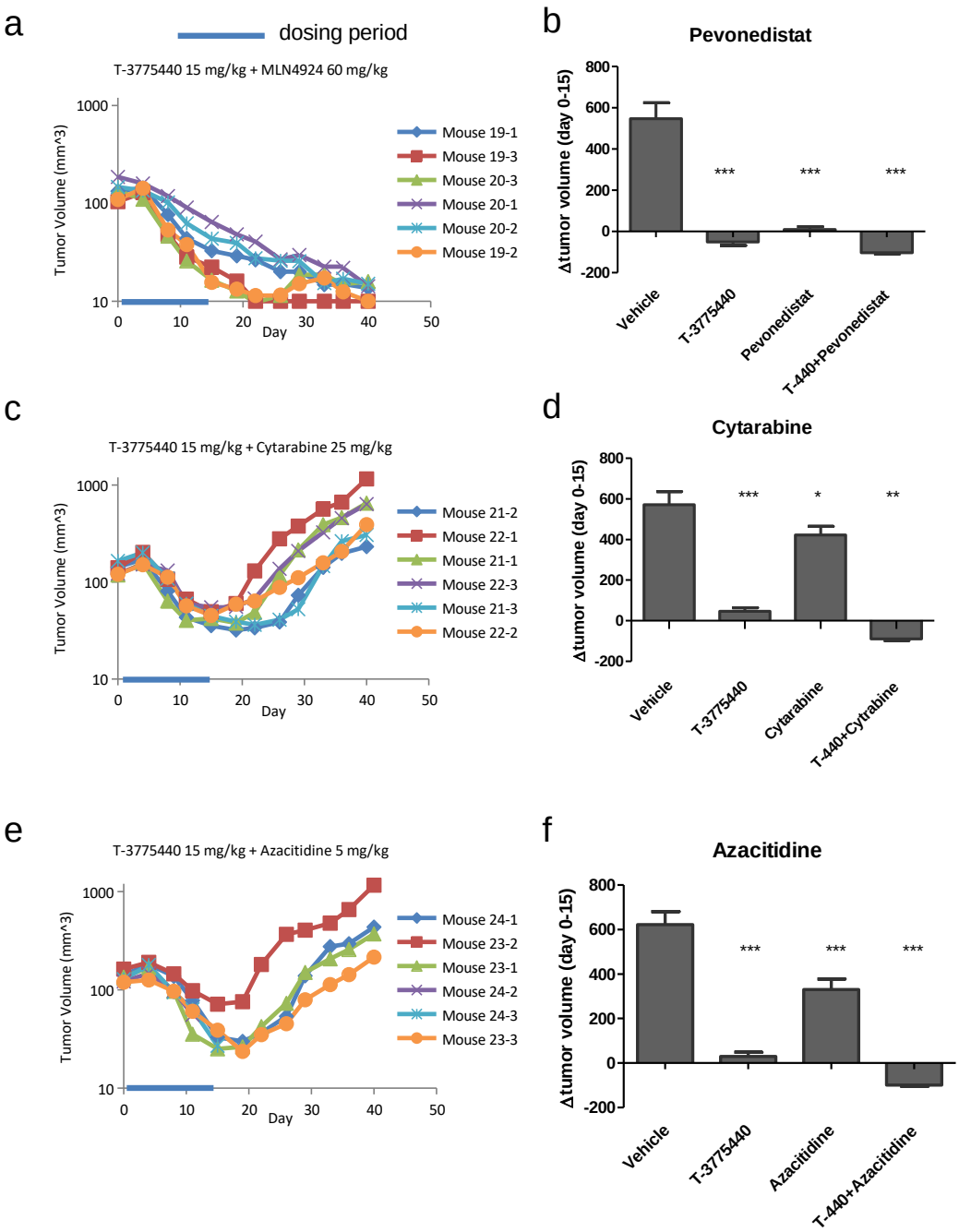
a
dosing period
T-3775440 15 mg/kg + MLN4924 60 mg/kg
Tumor Volume (mm^3)
Day
Mouse 19-1
Mouse 19-3
Mouse 20-3
Mouse 20-1
Mouse 20-2
Mouse 19-2
b
Pevonedistat
Δtumor volume (day 0-15)
Vehicle
T-3775440
Pevonedistat
T-440+Pevonedistat
c
T-3775440 15 mg/kg + Cytarabine 25 mg/kg
Mouse 21-2
Mouse 22-1
Mouse 21-1
Mouse 22-3
Mouse 21-3
Mouse 22-2
d
Cytarabine
Cytarabine
T-440+Cytrabine
e
T-3775440 15 mg/kg + Azacitidine 5 mg/kg
Mouse 24-1
Mouse 23-2
Mouse 23-1
Mouse 24-2
Mouse 24-3
Mouse 23-3
f
Azacitidine
Azacitidine
T-440+Azacitidine

Figure 14, continued

g

Treatment	Maximum BWC (day)	Mortality (day)
T-440/MLN4924	-14.9% (day 9)	0/6
T-440/Cytarabine	-6.5% (Day 14)	0/6
T-440/Azacitidine	-20.7% (Day 15)	2*/6 (Day 15)

*humanely euthanized mice (due to severe weight loss)

h

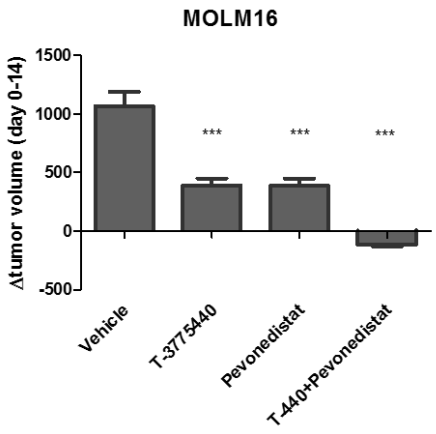

Figure 14. The T-3775440/pevonedistat combination exhibits significant anti-AML effects in subcutaneous xenograft models.

(a–g) Antitumor effects of T-3775440 in combination with pevonedistat (a, b), cytarabine (c, d), or azacitidine (e, f) were examined in TF-1a tumor subcutaneous models. Tumor growth curves for each individual mouse (a, c, e) and the changes in tumor volumes (b, d, f) from day 0 to day 15 are represented. The values represent mean tumor volume changes ± SEM (n = 5). Statistical significance was determined using Dunnett's multiple comparison test ($^{*}P < 0.05$, $^{***}P < 0.001$). Animals received T-3775440 (once daily, on a 5 days on/2 days off schedule, *p.o.*), pevonedistat (three times weekly, on days 1, 3, and 5, *s.c.*), cytarabine (three times weekly, on days 1, 3, and 5, *i.p.*), or azacitidine (twice weekly, on days 1 and 4, *s.c.*). (g) Maximum body weight change (BWC) and mortality rate were represented for each combination. (h) Antitumor effects of T-3775440 in combination with pevonedistat in a MOLM16 tumor subcutaneous model. The changes in tumor volumes from day 0 to day 14 are represented.

Figure 15

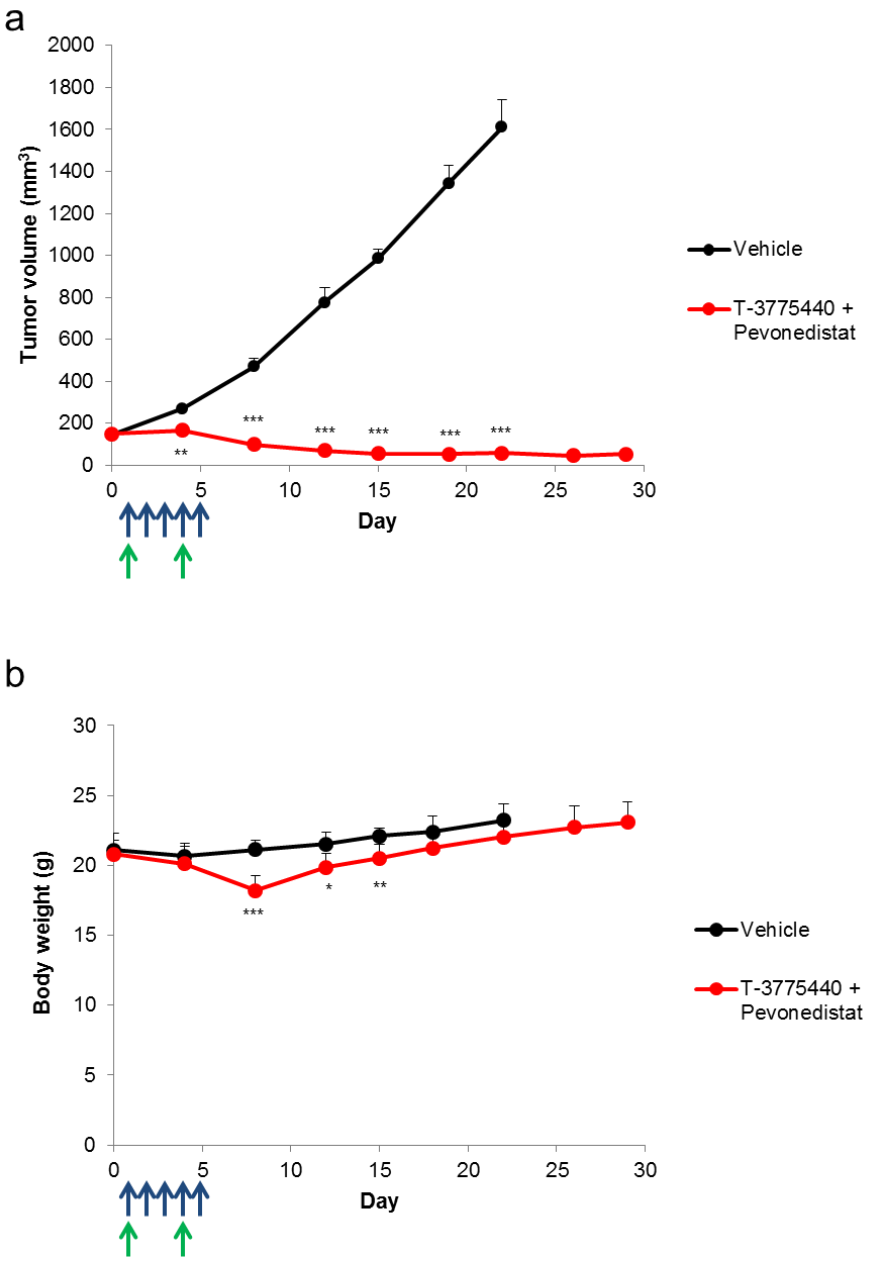

Figure 15. One cycle treatment of the T-3775440/pevonedistat combination induced sustained tumor regression.

Mice bearing TF-1a tumors were treated with T-3775440 (*p.o.*) once daily for 5 consecutive days and pevonedistat (*s.c.*) on days 1 and 4 (n = 6). (a) *Values*, mean tumor volume; *bars*, SEM. (b) *Values*, mean body weight; *bars*, SD. $^{*}P < 0.05$, $^{***}P < 0.001$. Aspin-Welch t test was used for the statistical analyses.

Figure 16

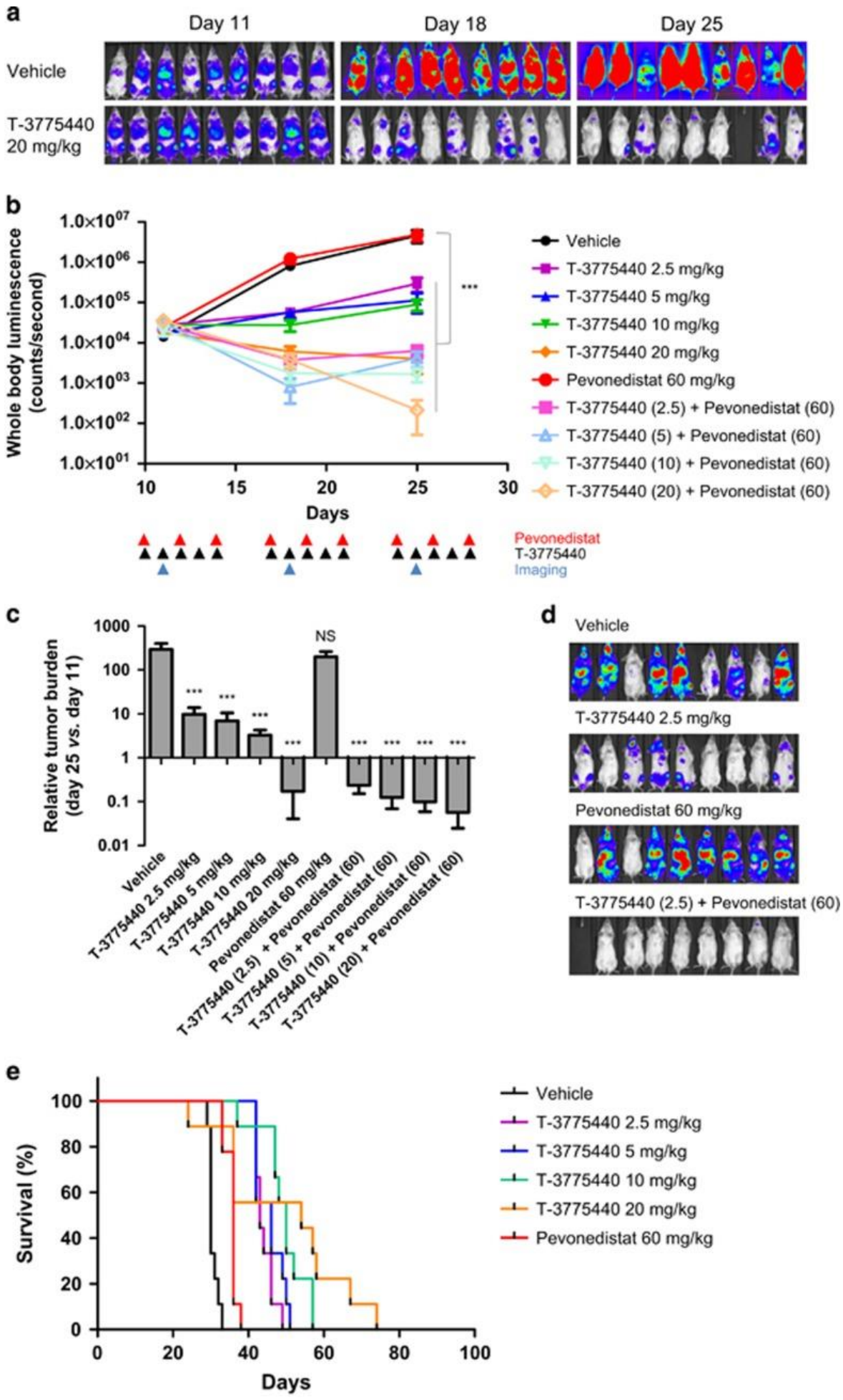
a
Day 11
Day 18
Day 25
Vehicle
T-3775440
20 mg/kg
b
Whole body luminescence
(counts/second)
1.0×10^07
1.0×10^06
1.0×10^05
1.0×10^04
1.0×10^03
1.0×10^02
1.0×10^01
10
15
20
25
30
Days
***
Vehicle
T-3775440 2.5 mg/kg
T-3775440 5 mg/kg
T-3775440 10 mg/kg
T-3775440 20 mg/kg
Pevonedistat 60 mg/kg
T-3775440 (2.5) + Pevonedistat (60)
T-3775440 (5) + Pevonedistat (60)
T-3775440 (10) + Pevonedistat (60)
T-3775440 (20) + Pevonedistat (60)
Pevonedistat
T-3775440
Imaging
c
Relative tumor burden
(day 25 vs. day 11)
1000
100
10
1
0.1
0.01
NS
***
Vehicle
T-3775440 2.5 mg/kg
T-3775440 5 mg/kg
T-3775440 10 mg/kg
T-3775440 20 mg/kg
Pevonedistat 60 mg/kg
T-3775440 (2.5) + Pevonedistat (60)
T-3775440 (5) + Pevonedistat (60)
T-3775440 (10) + Pevonedistat (60)
T-3775440 (20) + Pevonedistat (60)
d
Vehicle
T-3775440 2.5 mg/kg
Pevonedistat 60 mg/kg
T-3775440 (2.5) + Pevonedistat (60)
e
Survival (%)
100
80
60
40
20
0
0
20
40
60
80
100
Days
Vehicle
T-3775440 2.5 mg/kg
T-3775440 5 mg/kg
T-3775440 10 mg/kg
T-3775440 20 mg/kg
Pevonedistat 60 mg/kg

Figure 16, continued

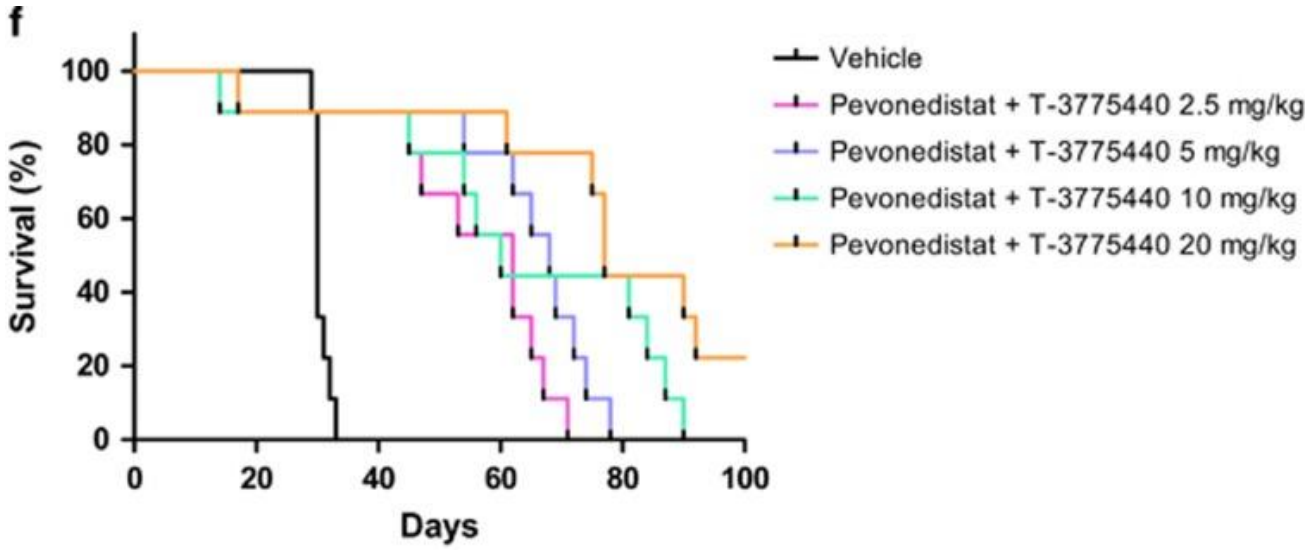

Figure 16. Coadministration of T-3775440/pevonedistat reduced leukemic burden and prolonged animal survival in an AML disseminated model.

(a–f) Mice were inoculated via the tail vein with luciferase-labeled TF-1a cells (day 0). Mice were randomized into groups (n=9 per group) and treatment was initiated 10 days after cell injection (day 10). T-3775440 was administrated once daily (*p.o.*), and pevonedistat three times per week (days 1, 3 and 5, *s.c.*) according to the indicated dose and schedule. Tumor growth was monitored using an *in vivo* imaging system at days 11, 18, and 25. (a) Luminescence images of TF-1a-luc cell-bearing mice that received 20 mg/kg T-3775440 or vehicle are shown. (b) Whole-body luminescence of each treatment group is shown at the indicated time points. All values are means, and bars represent the s.e.m. (c) Bar charts showing relative tumor burden of each treatment group compared with that at days 11 and day 25. Means and SEM are shown. Statistical significance was determined using Dunnett's multiple comparison test (***P<0.001). (d) Representative luminescence images (day 25). (e, f) Kaplan–Meier analysis was conducted to compare survival curves between vehicle-treated mice and T-3775440, MLN4924 or combination-treated mice. Single agent groups (e) and combination groups (f) are shown separately with the control group.

Figure 17

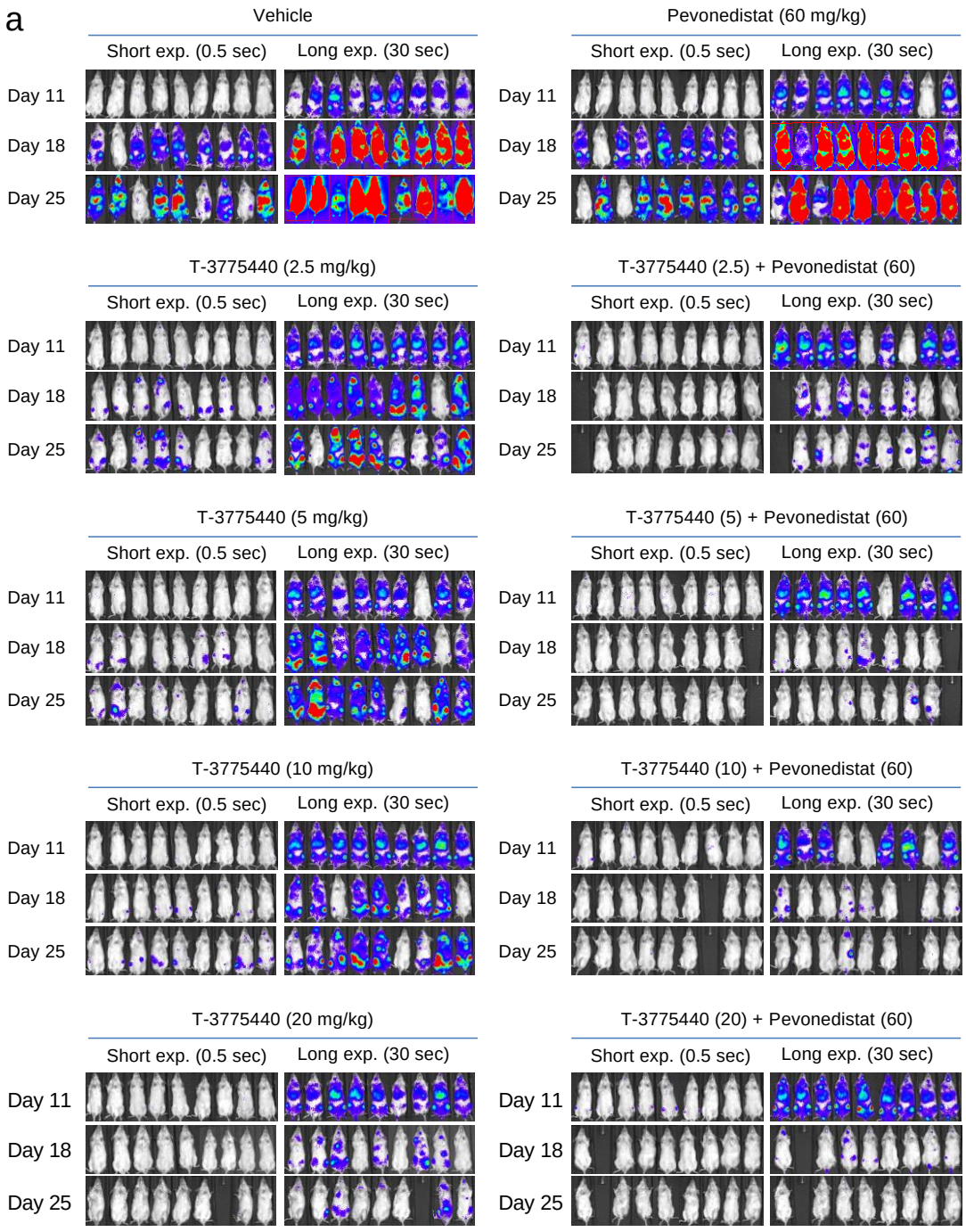
a
Vehicle
Short exp. (0.5 sec)
Long exp. (30 sec)
Day 11
Day 18
Day 25
Pevonedistat (60 mg/kg)
T-3775440 (2.5 mg/kg)
T-3775440 (2.5) + Pevonedistat (60)
T-3775440 (5 mg/kg)
T-3775440 (5) + Pevonedistat (60)
T-3775440 (10 mg/kg)
T-3775440 (10) + Pevonedistat (60)
T-3775440 (20 mg/kg)
T-3775440 (20) + Pevonedistat (60)

Figure 17, continued

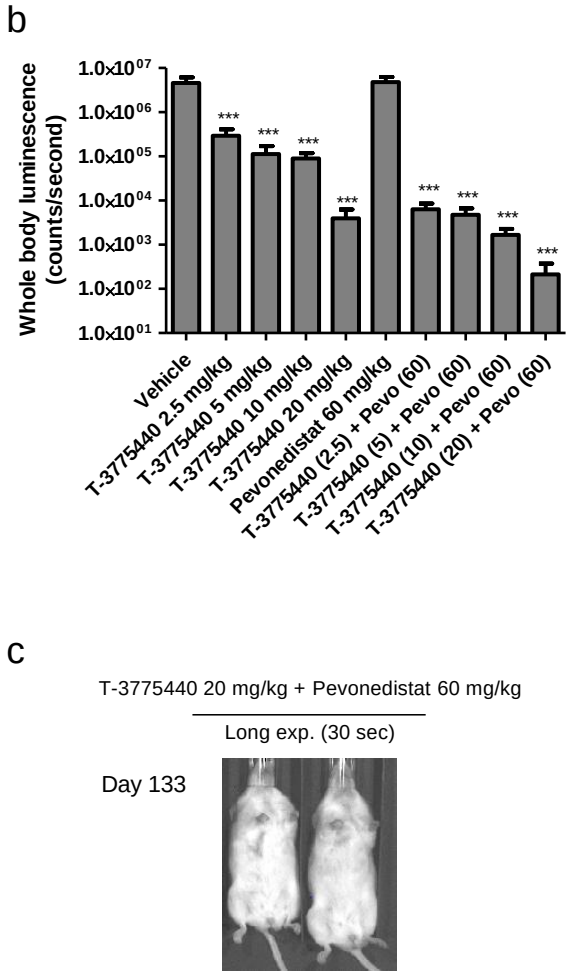

Figure 17. Coadministration of T-3775440/pevonedistat shows anti-leukemic effects in an AML disseminated model.

(a) Tumor growth was monitored on days 11, 18, and 25 after *i.p.* injection with luciferin, using an *in vitro* imaging system. Representative images of mice are shown. (b) Whole body luminescence was measured after the indicated treatment on day 25. Statistical significance was determined using Dunnett's multiple comparison test ($^{***}P < 0.001$). *Values*, mean body weight; *bars*, SD. (c) Two mice treated with T-3775440/pevonedistat combination did not show any sign of tumor regrowth (day 133).

Table 1. Culture medium information for cell lines used in cell proliferation assays.

Cell line	Medium	FBS	Supplement
CMK-11-5 (JCRB)	RPMI 1640 (Wako, 189-02145)	10%	no
CMK-86 (JCRB)	RPMI 1640 (Wako, 189-02145)	10%	no
EOL-1 (DSMZ)	RPMI 1640 (Wako, 189-02145)	10%	no
GF-D8 (DSMZ)	RPMI 1640 (Wako, 189-02145)	20%	50 ng/ml rhGM-CSF (Wako, 075-04114)
HEL92.1.7(ATCC)	RPMI 1640 (Wako, 189-02145)	10%	no
HL-60 (ATCC)	RPMI 1640 (Wako, 189-02145)	10%	no
HL-60/MX2 (ATCC)	RPMI 1640 (Wako, 189-02145)	10%	no
Kasumi-1 (JCRB)	RPMI 1640 (Wako, 189-02145)	10%	no
MOLM-16 (DSMZ)	RPMI 1640 (Wako, 189-02145)	20%	no
NB4 (DSMZ)	RPMI 1640 (Wako, 189-02145)	10%	no
OCI-AML3 (DSMZ)	MEM α (Wako, 135-15175)	20%	no
OCI-M2 (DSMZ)	IMDM (Gibco, 12440-053)	20%	no
TF-1a (ATCC)	RPMI 1640 (Wako, 189-02145)	10%	no
TF-1a/Ara-C	RPMI 1640 (Wako, 189-02145)	10%	no
THP-1 (ATCC)	RPMI 1640 (Wako, 189-02145)	10%	no
CCRF-CEM (ATCC)	RPMI 1640 (Wako, 189-02145)	10%	Sodium Pyruvate (Gibco, 11360)
MOLT-3 (ATCC)	RPMI 1640 (Wako, 189-02145)	10%	no
RPMI8226 (JCRB)	RPMI 1640 (Wako, 189-02145)	10%	no
KMS28BM (JCRB)	RPMI 1640 (Wako, 189-02145)	10%	no
HepG2	EMEM (Wako, 051-07615)	10%	Sodium Pyruvate (Gibco, 11360) NEAA (Gibco, 11140)

Table 2. Synergy score of T-3775440/pevonedistat combination in an AML cell panel.

Cell line	*Meaning*	*Blending synergy*	*Combination index*	*Incubation (h)*	*FAB*
TF-1a	Synergy	36.5	0.3	72	M6
TF-1a/Ara-C	Synergy	34.9	NA	72	M6
NB4	Synergy	33.5	NA	120	M3
Kasumi-1	Synergy	31.8	0.45	120	M2
MOLM-16	Synergy	28.4	NA	120	M7
HL-60/MX2	Synergy	23.3	0.42	120	M2
HL-60	Synergy	19.6	0.41	120	M2
HEL92.1.7	Additivity	14.6	NA	72	M6
OCI-M2	Additivity	10.9	0.81	72	M1
GF-D8	Additivity	8.6	NA	168	M7
CMK-11-5	Additivity	4.3	0.96	72	M5
THP-1	Additivity	-5.5	NA	144	M4
OCI-AML3	Additivity	-7.9	NA	168	M4
EOL-1	Additivity	-17.3	NA	120	Eosinophilic
CMK-86	Subadditivity	-27.6	1.73	72	M7

Abbreviations: AML, acute myeloid leukemia; CI, combination index; FAB, French–American–British Classification; NA, not applicable. CI values in the range 0–0.7 and 0.7–1.3 are classified as synergy and additivity, respectively. When CI values were not associated, nonlinear blending values >20 and between −20 and +20 were classified as synergy and additivity, respectively. The experiments were conducted in duplicate for TF-1a, TF-1a/Ara-C, NB4, Kasumi-1, HL-60/MX2, HL-60, OCI-M2, GF-D8, OCI-AML3 and in triplicate for MOLM-16, HEL92.1.7, CMK-11–5, THP-1, EOL-1, CMK-86.

Table 3. Effect of T-3775440 on the sensitivity of TF-1a cells to pevonedistat (related to Fig. 3a).

T-3775440	Relative cell proliferation (%)		EC_{50} of pevonedistat (nmol/L)	95% Confidence intervals (nmol/L)
	Bottom	Top		
0 nM	-3.0	96.2	770	583–1015
4.6 nM	1.9	83.9	326***	283–375
21.5 nM	3.4	59.5	215***	191–241
100 nM	3.1	53.9	167***	152–185

NOTE: TF-1a cells were co-treated with pevonedistat and T-3775440 at the indicated concentrations for 72 h. EC_{50} values and their 95% confidence intervals were calculated using nonlinear regression analysis of the percentage inhibition. One-way ANOVA along with post-Dunnett's multiple comparison test were performed to compare the EC_{50} values obtained from the nonlinear regression analysis [$^{***}P < 0.001$, versus control (0 nM)].

Table 4. Effect of GFI1 family protein knockdown on the sensitivity of TF-1a cells to pevonedistat (related to Fig. 3e).

siRNA	Relative cell proliferation (%)		EC_{50} of pevonedistat (nmol/L)	95% Confidence intervals (nmol/L)
	Bottom	Top		
siControl	0.3	97.1	427	365–499
siLSD1#1	2.2	89.7	168*	150–187
siLSD1#2	2.4	89.1	153*	140–166
siGFI1B#1	2.2	67.2	196*	170–227
siGFI1B#2	2.1	63.4	232*	208–259
siGFI1#1	-0.3	90.2	395	317–492
siGFI1#2	-0.4	88.7	402	336–480

NOTE: TF-1a cells were treated with the indicated siRNAs for 6 h and re-plated. After overnight incubation, cells were treated with pevonedistat for 72 h. For each siRNA treatment, the EC_{50} values of pevonedistat were calculated. All assays were done in triplicate (n = 3). EC_{50} values and their 95% confidence intervals were calculated using nonlinear regression analysis of the percentage inhibition. siLSD1 and siGFI1B, but not siGFI1, augmented the anti-proliferative activity of pevonedistat in TF-1a cells. One-way ANOVA and post-Dunnett's multiple comparison test were performed to compare the EC_{50} values obtained from the nonlinear regression analysis ($^{*}P < 0.05$, versus siControl).

Table 5. Effects of DTL knockdown on the sensitivity of TF-1a cells to T-3775440 (related to Fig. 10b).

siRNA	Relative cell proliferation (%)		EC_{50} of pevonedistat (nM)	95% Confidence intervals (nM)
	Bottom	Top		
siCTRL	50.21	94.21	11.1	9.0–13.7
siDTL	9.653	39.34	5.1^{***}	4.1–6.5

NOTE: TF-1a cells were treated with the indicated siRNAs for 6 h and re-plated. After incubation overnight, cells were treated with pevonedistat for 72 h. For each siRNA treatment, the EC_{50} values of T-3775440 were calculated. All assays were done in quadruplicate. EC_{50} values and their 95% confidence intervals were calculated using nonlinear regression analysis of the percentage inhibition. Unpaired t test was performed to compare the EC_{50} values obtained from the nonlinear regression analysis ($^{***}P < 0.001$, versus siControl).

Table 6. Median survival time after administration of T-3775440, pevonedistat, or the indicated combination in the TF-1a-luc disseminated model (related to Fig. 16).

Group	Median survival (days)	*p* value
Control	30	NA
2.5 mg/kg T-3775440	43	< 0.0001
5 mg/kg T-3775440	46	< 0.0001
10 mg/kg T-3775440	50	< 0.0001
20 mg/kg T-3775440	54	0.0004
60 mg/kg pevonedistat	36	< 0.0001
T-3775440 (2.5) + pevonedistat (60)	62	0.0004
T-3775440 (5) + pevonedistat (60)	68	0.0004
T-3775440 (10) + pevonedistat (60)	60	0.0004
T-3775440 (20) + pevonedistat (60)	77	0.0004

NOTE: Statistical analysis was performed with a Log-rank test (p <0.00555 after the Bonferroni correction was considered statistically significant).

Part 2

TP-064, a potent and selective small molecule inhibitor of PRMT4 for multiple myeloma

Abstract

Protein arginine methyltransferase (PRMT) 4 (also known as coactivator-associated arginine methyltransferase 1; CARM1) is involved in a variety of biological processes and is considered as a candidate oncogene owing to its overexpression in several types of cancer. Selective PRMT4 inhibitors are useful tools for clarifying the molecular events regulated by PRMT4 and for validating PRMT4 as a therapeutic target. In this study, I identified TP-064, a potent, selective, and cell-active chemical probe of human PRMT4 and revealed its co-crystal structure with PRMT4. TP-064 inhibited the methyltransferase activity of PRMT4 with high potency (half-maximal inhibitory concentration, IC_{50} < 10 nM) and selectivity over other PRMT family proteins, and reduced arginine dimethylation of the PRMT4 substrates BRG1-associated factor 155 (BAF155; IC_{50} = 340 ± 30 nM) and Mediator complex subunit 12 (MED12; IC_{50} = 43 ± 10 nM). TP-064 treatment inhibited the proliferation of a subset of multiple myeloma cell lines, with affected cells arrested in G1 phase of the cell cycle. TP-064 and its negative control (TP-064N) will be valuable tools to further investigate the biology of PRMT4 and the therapeutic potential of PRMT4 inhibition.

Introduction

Protein arginine methyltransferases (PRMTs) catalyze arginine methylation of proteins, which involves the transfer of the methyl group of S-adenosyl-L-methionine (SAM) to the terminal guanidino nitrogens of arginine. This reaction can give rise to three types of methylarginine species including monomethylarginine (MMA), symmetric dimethylarginine (SDMA), and asymmetric dimethylarginine (ADMA). PRMTs are classified according to their methylation products as Type I (PRMT1, 2, 3, 4, 6, and 8, which can convert arginine to MMA and ADMA), Type II (PRMT5 and 9, which produce MMA and SDMA), and Type III (PRMT7, which generates MMA only) [58]. Arginine methylation influences target interactions with other proteins and modulates their physiological functions [59].

PRMT4, also known as coactivator-associated arginine methyltransferase 1, is a Type I PRMT that methylates arginines 17 and 26 of histone H3 [60] as well as non-histone proteins involved in a variety of biological processes including transcriptional activation [61], RNA splicing [62], cell cycle regulation [63], DNA damage response [64], and cell differentiation [65]. PRMT4 is dysregulated in several diseases and has been linked to breast [63], prostate [66], and colorectal cancer [67] and positively regulates transcriptional activators including Wnt/β-catenin in colorectal cancer [68], estrogen receptor-α in breast cancer [69], Runt-related transcription factor 1 in myeloid leukemia [70], and the Switch/sucrose non-fermentable chromatin remodeling complex in breast cancer [71]. These reports suggest that PRMT4 is a potential therapeutic target in certain types of cancer.

Potent, selective, and cell-active small molecule PRMT4 inhibitors can be useful tools for clarifying the molecular events regulated by protein arginine methylation and for validating PRMT4 as a therapeutic target. A number of PRMT4 inhibitors have recently been reported [72]. For example, potent and selective PRMT4 inhibitors were developed that did not exhibit cellular activity [73, 74], while a cell-active inhibitor of Type I PRMTs that is not selective for PRMT4 was also reported [75]. Since Type I PRMTs (except for PRMT8) are ubiquitously expressed [76], improving the selectivity

for PRMT4 can avoid adverse events caused by other Type I PRMT inhibitors. Recently, a potent, selective, and cell-active inhibitor has been reported, EZM2302, which shows activity in preclinical models of multiple myeloma [77].

Here I described the development of a potent and selective PRMT4 inhibitor with high cellular activity. The co-crystal structure of PRMT4 in complex with N-methyl-N-((2-(1-(2-(methylamino)ethyl)piperidin-4-yl)pyridin-4-yl)methyl)-3-phenoxybenzamide (TP-064) provided structural evidence for the specificity of inhibition. I also showed that TP-064 inhibited the growth of a subset of multiple myeloma (MM) cell lines. These results indicate that TP-064 may be an effective drug for the treatment of MM that acts by targeting PRMT4.

Materials and Methods

Synthesis of TP-064 and TP-064N

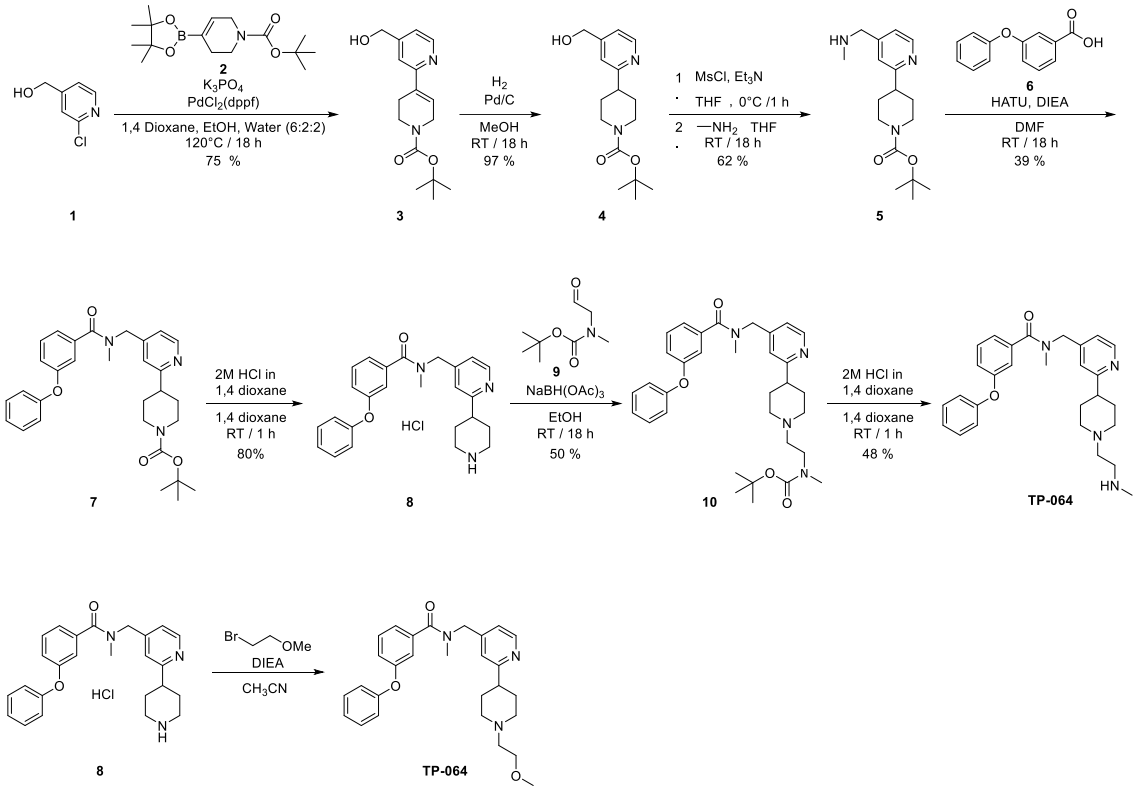

Experimental procedure for 3

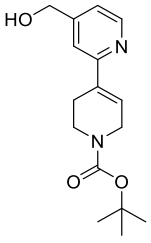

3

Tert-butyl 4-(4-(hydroxymethyl)pyridin-2-yl)-5,6-dihydropyridine-1(2H)-carboxylate

Potassium phosphate (22.2 g, 104.89 mmol, 3 eq.) was added to a solution of (2-chloropyridin-4-yl)methanol (5 g, 34.965 mmol, 1 eq.) and tert-butyl 4-(4,4,5,5-tetramethyl-1,3,2-dioxaborolan-2-yl)-5,6-dihydropyridine-1(2H)-carboxylate (12.97 g, 41.958 mmol, 1.2 eq.) in 1,4 dioxane:ethanol:water (70 ml, 6:2:2) with stirring and argon bubbling for 10 min. This was followed by addition of

[1,1bis(diphenylphosphino)ferrocene]-palladium(II) dichloride (1.42 g, 1.748 mmol, 0.05 eq.) in sealed tube under dry atmosphere. The resultant reaction mixture was heated at 120°C for 18 h. The progress of the reaction was monitored by thin-layer chromatography (TLC). After completion of the reaction, the solution was filtered through a celite bed and washed with ethyl acetate; the filtrate was concentrated under reduced vacuum pressure to obtain the crude compound, which was purified by silica gel (60–120 mesh) column chromatography, eluted with 60% ethyl acetate/pet ether to obtain **3** (7.5 g, yield: 75%) as a yellow solid. The proton nuclear magnetic resonance (**^{1}H NMR**) (**400 MHz, $CDCl_3$**) values were as follows: δ 1.48 (9H, s), 2.62-2.64 (2H, m), 3.63 (2H, t, *J* = 5.38 Hz), 4.09–4.14 (2H, m), 4.74 (2H, s), 6.60 (1H, s), 7.14 (1H, d, *J* = 4.89 Hz), 7.37 (1H, s), 8.50 (1H, d, *J* = 4.89 Hz). Liquid chromatography–mass spectrometry (LC–MS) (M+H): 291.17.

Experimental procedure for 4

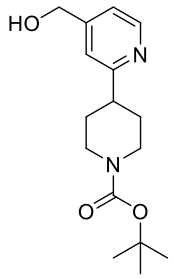

4

Tert-butyl 4-(4-(hydroxymethyl)pyridin-2-yl)piperidine-1-carboxylate

The stirred and degassed solution of **3** (8.5 g, 29.274 mmol, 1 eq.) in methanol (200 ml) was combined with 10% Pd/C (0.311 g, 2.927 mmol, 0.1 eq.) and subjected to hydrogenation under balloon pressure

for 18 h. The progress of the reaction was monitored by TLC. After completion of the reaction, the solution was filtered through a celite bed and washed with methanol, and the filtrate was concentrated under reduced vacuum pressure to obtain **4** (7.1 g, yield: 97%) as an off-white gummy liquid. The **^{1}H NMR** (**400 MHz, $CDCl_3$**) values were as follows δ 1.47 (9H, m), 1.66–1.76 (3H, m), 1.89–1.92 (3H, m), 2.80–2.89 (3H, m), 4.25 (1H, brs), 4.73 (2H, s), 7.12 (1H, d, *J* = 5.38 Hz), 7.16 (1H, s), 8.50 (1H, d, *J* = 4.89 Hz). LC–MS (M+H): 293.21.

Experimental procedure for 5

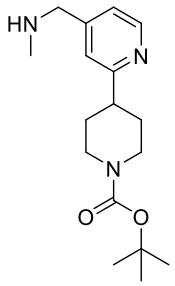

5

Tert-butyl 4-(4-((methylamino)methyl)pyridin-2-yl)piperidine-1-carboxylate

The stirred solution of **4** (5 g, 17.1 mmol, 1 eq.) in t*etrahydrofuran* (40 ml) was combined with triethylamine (5.18 g, 51.304 mmol, 3 eq.) and thionyl chloride (2.35 g, 20.52 mmol, 1.2 eq.) at 0°C. The resultant reaction mixture was allowed to stir at room temperature for 1 h before adding 40 ml methylamine (2 M in tetra-n-butylammonium fluoride) at room temperature . The mixture was stirred at room temperature for 18 h, with the progress of the reaction monitored by TLC. After completion of the reaction, the mixture was concentrated under reduced vacuum pressure to obtain the crude

compound, which was purified by silica gel (60–120 mesh) column chromatography, eluted with 5% methanol/dichloromethane to obtain **5** (5.09 g, yield: 62%) as a pale yellow gummy liquid. The **^{1}H NMR** (**400 MHz, DMSO-d$_6$**) values were as follows: δ 1.41 (9H, s), 1.54–1.58 (2H, m), 1.82 (2H, d, *J* = 10.76 Hz), 2.50 (3H, s), 2.82–2.88 (3H, m), 3.01–3.03 (2H, m), 3.97 (2H, s), 4.02–4.09 (1H, s), 7.22–7.37 (2H, m), 8.50 (1H, d, *J* = 5.38 Hz). LC–MS (M+H): 306.21.

Experimental procedure for 7

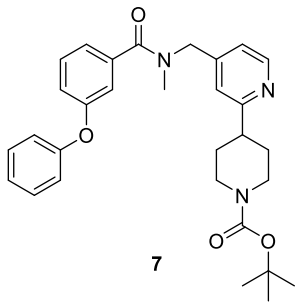

7

Tert-butyl-4-(4-((N-methyl-3-phenoxybenzamido)methyl)pyridin-2-yl)piperidine-1-carboxylate

(1-[Bis(dimethylamino)methylene]-1H-1,2,3-triazolo[4,5-b]pyridinium-3-oxid hexafluorophosphate) (11.4 g, 30.12 mmol, 2 eq.) and N,N-diisopropylethylamine (5.8 g, 45.18 mmol, 3 eq.) were added to the stirred solution of 3-phenoxybenzoic acid (3.87 g, 18.073 mmol, 1.2 eq.) in dimethylformamide (30 ml) at room temperature with stirring for 5 min; **5** (4.6 g, 15.06 mmol, 1 eq.) in dimethylformamide (10 ml) was then added at room temperature with stirring for 18 h. The progress of the reaction was monitored by TLC. After completion of the reaction, the solution was diluted with water and extracted with ethyl acetate. The Ethyl acetate layer was washed with water and brine solution and dried over anhydrous Na_2SO_4, then filtered and evaporated under reduced pressure to obtain the crude compound.

This was purified by silica gel (60–120 mesh) column chromatography, eluted with 60% ethyl acetate/pet ether to obtain compound **7** (2.9 g, Yield: 38.6%) as a pale yellow gummy liquid. The **^{1}H NMR** (**300 MHz, $CDCl_3$**) values were as follows: δ 1.47 (9H, s), 1.68-1.72 (2H, m), 1.83–1.90 (2H, m), 2.80–3.02 (6H, m), 4.23–4.26 (2H, m), 4.48–4.70 (2H, m), 6.91–7.19 (8H, m), 7.33–7.35 (3H, m), 8.48–8.50 (1H, m). LC–MS (M+H): 502.34.

Experimental procedure for 8

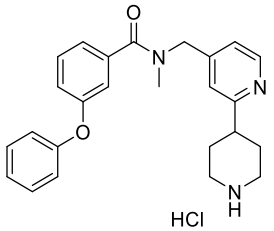

8

N-methyl-3-phenoxy-N-((2-(piperidin-4-yl)pyridin-4-yl)methyl)benzamide hydrochloride

1,4-Dioxane in HCl (2M) (10 ml) was added to the stirred solution of **7** (2.5 g, 5.186 mmol, 1 eq.) in 1,4 dioxane (10 ml) at 0°C and the resultant mixture was stirred at room temperature for 1 h. The progress of the reaction was monitored by TLC. After completion of the reaction, the solution was concentrated under reduced pressure to obtain the crude compound, which was co-distilled with dichloromethane and washed with *n*- pentane to obtain **8** (1.91 g, yield: 79.5%) as a pale yellow solid. The **^{1}H NMR** (**300 MHz, DMSO-d_6**) values were as follows: δ 1.97–2.06 (4H, m), 2.93–3.02 (5H, m), 3.11–3.18 (1H, m), 3.34–3.38 (2H, m), 4.66 (2H, brs), 6.98–7.01(2H, m), 7.06–7.21 (3H, m), 7.29 (2H, s), 7.35–7.47 (3H, m), 8.51-8.53 (1H, m), 8.82 (1H, brs), 9.38 (1H, brs). LC–MS [(M-2HCl)+H]:

402.25.

Experimental procedure for 10

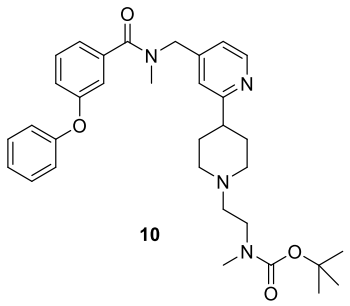

10

Tert-butyl methyl(2-(4-(4-((N-methyl-3-phenoxybenzamido)methyl)pyridin-2-yl)piperidin-1-yl)ethyl)carbamate

Sodium triacetoxyborohydride (0.527 g, 2.490 mmol, 5 eq.) was added to the stirred solution of **8** (0.2 g, 0.498 mmol, 1 eq.) and **9** (0.172 g, 0.996 mmol, 2 eq.) in ethanol (20 ml) at 0°C; the resultant reaction mixture was allowed to stir at room temperature for 18 h. The progress of the reaction was monitored by TLC. After completion of the reaction, the solution was basified with saturated sodium bicarbonate solution and extracted with ethyl acetate. The ethyl acetate layer was washed with water and brine solution, dried over anhydrous Na_2SO_4, filtered, and evaporated under reduced pressure to obtain the crude compound, which was purified by silica gel (60–120 mesh) column chromatography and eluted with 3% methanol/ dichloromethane to obtain **10** (0.14 g, yield: 50.3%) as a brown gummy liquid, which was confirmed by LC–MS. LC–MS (M+H): 559.38.

Experimental procedure for TP-064

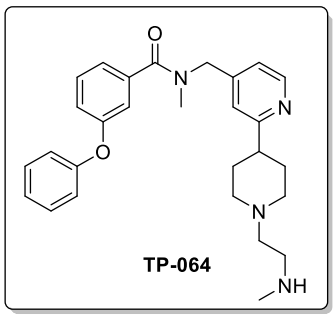

N-methyl-N-((2-(1-(2-(methylamino)ethyl)piperidin-4-yl)pyridin-4-yl)methyl)-3-phenoxybenzamide

1,4-Dioxane in HCl (2M) (2 ml) was added to the stirred solution of **10** (0.14 g, 0.882 mmol, 1 eq.) in 1,4 dioxane (5 ml) was added at 0°C and the resulting reaction mixture was allowed to stir at room temperature for 1 h. The progress of the reaction was monitored by TLC. After completion of the reaction, the reaction mixture was concentrated under reduced pressure to obtain the crude compound, which was co-distilled with dichloromethane and diethyl ether, basified with triethylamine, and concentrated. The free acid was purified by preparative high-performance LC to obtain **TP-064** (55.5 mg, yield: 48.6%) as a brown semi-solid. The **^{1}H NMR (400 MHz, DMSO-d$_6$)** values were as follows: δ 1.73–1.76 (4H, m), 1.95–2.05 (2H, m), 2.31 (3H, s), 2.40 (2H, t, *J* = 6.26 Hz), 2.60 (3H, t, *J* = 6.26 Hz), 2.88–2.94 (5H, m), 4.46–4.63 (2H, m), 6.94–7.48 (12H, m), 8.43 (1H, brs). LC–MS (M+H): 459.1.

Experimental procedure for TP-064N

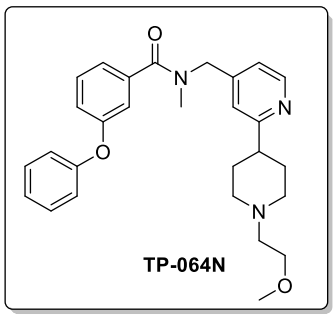

N-((2-(1-(2-methoxyethyl)piperidin-4-yl)pyridin-4-yl)methyl)-N-methyl-3-phenoxybenzamide

A mixture of N-methyl-3-phenoxy-N-((2-(piperidin-4-yl)pyridin-4-yl)methyl)benzamide hydrochloride (2000 mg, 4.57 mmol), 1-bromo-2-methoxyethane (698 mg, 5.02 mmol), and N, N-diisopropylethylamine (3.99 ml, 22.83 mmol) in CH_3CN (15 ml) was stirred at 50°C for 5 h. The mixture was neutralized with saturated $NaHCO_3$ aq. at 0°C and extracted with ethyl acetate. The organic layer was separated, washed with water and brine, dried over $MgSO_4$, and concentrated under vacuum. The residue was purified by column chromatography (NH silica gel, eluted with 50%–100% ethyl acetate in hexane) to obtain N-((2-(1-(2-methoxyethyl)piperidin-4-yl)pyridin-4-yl)methyl)-N-methyl-3-phenoxybenzamide **TP-064N** (740 mg, 1.610 mmol, 35.3%) as a white solid. The **^{1}H NMR (300 MHz, DMSO-d_6)** values were as follows: δ ppm 1.59–1.84 (m, 4 H) 2.05 (t, *J* = 10.27 Hz, 2 H) 2.43–2.49 (m, 2 H) 2.60 (br. s., 1 H) 2.84–3.03 (m, 5 H) 3.24 (s, 3 H) 3.44 (t, *J* = 5.93 Hz, 2 H) 4.34–4.76 (m, 2 H) 6.82–7.29 (m, 8 H) 7.29–7.61 (m, 3 H) 8.43 (br. s., 1 H). LC–MS (M+H): 460.2.

Reagents

[3H]SAM was purchased from PerkinElmer Life Sciences (Waltham, MA, USA; cat. no. NET155V001MC; specific activity range: 12–18 Ci/mmol). SAM was obtained from AK Scientific (Union City, CA, USA). Biotinylated peptide substrates were purchased from Tufts University Peptide Synthesis Core Facility (Boston, MA, USA).

Enzymatic assays for PRMTs

The assay conditions and protein constructs used in this study are presented in Tables 7 and 8, respectively. The protein purification procedures have been previously described [74, 78, 79, 80]. In the scintillation proximity assay (SPA), specific amounts of enzyme and biotinylated peptide substrate were mixed with the compound and the reaction was initiated by adding SAM. IC_{50} values were measured at the apparent K_m concentrations of the substrate and SAM. The reaction was quenched by adding an equal volume of 7.5 M guanidine hydrochloride, and the reaction product was measured by SPA using FlashPlate Plus and TopCount NXT HTS plate reader (both from Perkin Elmer Life Sciences).

Selectivity assay

The selectivity assay was performed as previously described [81]. The effect of test compounds on the methyltransferase activities of Euchromatic histone-lysine N-methyltransferase 2 (G9a), G9a-like protein (GLP), Suppressor of variegation 3-9 homolog (SUV39H)1, SUV39H2, SUV420H1, SUV420H2, SET domain (SETD)2, SETD8, SETD bifurcated 1 (SETDB1), SETD7, Mixed-lineage leukemia (MLL)1 trimeric complex, MLL3 pentameric complex, Enhancer of zeste homolog (EZH)2 trimeric complex, PRMT1, PRMT3, PRMT4, PRMT5/Methylosome protein (MEP)50 complex, PRMT6, PRMT7, PRMT8, PRMT9, PR domain zinc finger protein (PRDM)9, SET and MYND domain-containing (SMYD)2, SMYD3, and DNA methyltransferase (DNMT)1 was assessed by monitoring the incorporation of a tritium-labeled methyl group into substrates with the

scintillation proximity assay [82]. Briefly, a 10-µl reaction containing 3H-SAM and substrate at concentrations close to the apparent Km values for each enzyme was prepared. Two concentrations (1 and 10 µM) of compound were tested. The reactions were quenched with 10 µl of 7.5 M guanidine hydrochloride; 180 µl of 20 mM Tris buffer (pH 8.0) were added, and the mixture was transferred to a 96-well FlashPlate followed by incubation for 1 h. The counts per minute (CPM) was measured on a TopCount plate reader; the CPM in the absence of compound or enzyme was defined as 100% activity and background (0%), respectively, for each dataset.

For DNMT1, the double-stranded DNA substrate was prepared by annealing two complementary strands (biotinylated forward strand: B-GAGCCCGTAAGCCCGTTCAGGTCG and reverse strand: CGACCTGAACGGGCTTACGGGCTC) that were synthesized by Eurofins MWG Operon (Louisville, KY, USA). A filter-based assay was used for DOT1L, Nuclear receptor binding SET domain protein (NSD)1, NSD2, NSD3, ASH1-like histone lysine methyltransferase (ASH1L), DNMT3A/3L, and DNMT3B/3L in which 10 µl of reaction mixture were incubated at 23°C for 1 h, followed by addition of 50 µl of 10% trichloroacetic acid (TCA). The mixture was transferred to filter plates (Millipore, Billerica, MA, USA) that were centrifuged at 2,000 rpm (Allegra X-15R; Beckman Coulter, Brea, CA, USA) for 2 min, washed twice with 10% TCA and once with ethanol (180 µl), and centrifuged. After drying, 100 µl MicroScint-O (Perkin Elmer) was added to each well and the plates were centrifuged to remove the liquid. A 70-µl volume of MicroScint-O was added and the CPM was measured with a TopCount plate reader.

Substrate competition assays

The substrate competition assays were performed by measuring IC_{50} values at various concentrations of one substrate (e.g., peptide) and at saturating concentrations of the other (e.g., SAM) and vice versa, as previously described [83].

Orthogonal binding confirmation

SPR experiments were performed using a Biacore T200 system (GE Healthcare, Little Chalfont, UK). Approximately 6,500 response units of PRMT4 were amino-coupled onto one flow cell of a CM5 chip according to manufacturer's protocol, while another flow cell was left empty for reference subtraction. SPR analysis was performed in HBS-EP buffer composed of 20 mM HEPES (pH 7.4), 150 mM NaCl, 3 mM EDTA, and 0.05% Tween-20 with 5% dimethylsulfoxide (DMSO), and 50 µM SAH. TP-064 was prepared at concentrations of 500, 125, 31.3, and 7.8 nM by serial dilution. Kinetic determination experiments were performed at 20°C using single cycle kinetics with an on time of 180 s, off time of 300 s, and a flow rate of 100 µl min^{-1}. To favor complete dissociation of the compound for the subsequent cycle, HBS-EP with 5% DMSO and no SAH was run for 300 s at 50 µl min^{-1}, and two blank cycles were run between each cycle. Kinetic curve fitting and KD calculations were performed with a 1:1 binding model using Biacore T200 Evaluation software. DSLS was performed as previously described [84] using 100 mM HEPES (pH 7.5), 150 mM NaCl, 3% DMSO, and 0.4 mg ml^{-1} (6 µM) protein in a 10-µl reaction volume.

Crystallization, data collection, and structure determination

A DNA fragment encoding the methyltransferase domain of human PRMT4 (residues 140–480) was cloned into a baculovirus expression vector pFBOH-MHL (http://www.thesgc.org/sites/default/files/toronto_vectors/pFBOH-MHL.pdf). The protein was expressed in Sf9 cells as an N-terminal hexa-His tag fusion protein and purified by metal chelating affinity chromatography (TALON resin; Clontech, Mountain View, CA, USA) followed by size-exclusion chromatography (Superdex 200; GE Healthcare). Pooled fractions containing PRMT4 were subjected to tobacco etch virus treatment to remove the His-tag. The protein was purified to homogeneity by ion-exchange chromatography.

Purified PRMT4 (6.1 mg ml^{-1}) was mixed with TP-064 at a 1:5 molar ratio of protein:inhibitor and crystallized with the sitting drop vapor diffusion method at 20°C by mixing 2 µl of protein solution

with 1 µl of the reservoir solution containing 20% PEG3350, 0.2 M ammonium sulfate, and 0.1 M Tris-HCl (pH 8.5).

X-ray diffraction data for PRMT4 + TP-064 were collected at 100 K on a Rigaku FR-E superbright X-ray generator. Data were processed using the HKL-3000 suite [85]. The structure of PRMT4 + TP-064 was isomorphous to PDB entry 4IKP, which was used as a starting model. REFMAC [86] was used for structure refinement. Geometric restraints for compound refinement were prepared with GRADE v.1.102 developed at Global Phasing Ltd. (Cambridge, UK). The COOT graphics program [87] was used for model building and visualization, and MOLPROBITY [88] was used for structure validation.

Docking

The X-ray crystal structure of rPRMT3 (PDB 1F3L) [89] and human PRMT6 (PDB 5E8R) [75] were used according to a previously described docking protocol [74]. Docking calculations were performed using Glide SP (Schrodinger, NY, USA) with default settings. Hydrogen bonding constraints were imposed with Glu326 and His476 of PRMT3 and Glu155 and His317 of PRMT6.

Cell culture

786-O, A498, A549, A704, AML-193, C2BBe1, Caki-1, Caki-2, CAMA-1, Caov-3, Caov-4, COLO-205, DMS114, DMS53, G-401, HCT116, HCT15, HCT-8, HPAC, HPAF-II, Hs 746T, HT1080, HT-29, JEG-3, KATOIII, LS174T, MDA-MB-231, MDA-MB-361, MDA-MB-468, MG-63, MIA-PaCa-2, MM.1R, MM.1S, MSTO-211H, NCI-H1755, NCI-H2228, NCI-H226, NCI-H23, NCI-H2452, NCI-H28, NCI-H460, NCI-H520, NCI-H522, NCI-H661, NCI-H69, NCI-H810, NCI-H929, RKO, SK-MEL-2, SK-MEL-24, SK-MEL-28, SK-MEL-5, SKOV-3, SW1271, SW1417, SW620, SW780, SW948, T-24, T47D, T84, TF-1a, THP-1, U266B1, and U2OS cell lines were purchased from American Type Culture Collection (Manassas, VA, USA). CMK-11-5, COLO201, COLO320 DM, Daudi, Kasumi-1, KMM-1, KMS-11, KMS-12-BM, KMS-12-PE, KMS-20, KMS-26, KMS-27, KMS-

28BM, KYSE70, MCF-7, MOLM-16, PL-21, RPMI8226, and SKNO-1 cell lines were from the Japanese Collection of Research Bioresources Cell Bank (Osaka, Japan). The A2780 cell line was from DS Pharma Biomedical (Osaka, Japan). The CACO-2 cell line was from RIKEN BioResource Center (Tsukuba, Japan). OVCAR-4 and SF268 cell lines were from National Cancer Institute (Bethesda, MD, USA). The PA-TU-8902 cell line was from Creative Bioarray (Shirley, NY, USA). SW48 cell line was from Horizon Discovery (Cambridge, UK). The OCI-Ly19 cell line was a gift from Dr. Louis Staudt (National Cancer Institute). The HEK293T cell line was a gift from Sam Benchimol, York University. Table 9 summarizes the source and culture conditions of each cell line.

Western blotting

HEK293 cells were lysed in lysis buffer composed of 20 mM Tris-HCl (pH 8.0), 150 mM NaCl, 1 mM EDTA, 10 mM $MgCl_2$, 0.5% TritonX-100, and 12.5 U ml^{-1} benzonase (Sigma-Aldrich, St. Louis, MO, USA) and containing complete EDTA-free protease inhibitor cocktail (Roche Diagnostics, Indianapolis, IN, USA). After incubation for 3 min at room temperature, sodium dodecyl sulfate (SDS) was added to a final concentration of 1%. Cell lysates were resolved on 4–12% Bis-Tris protein gels (Invitrogen, Carlsbad, CA, USA) with MOPS buffer (Invitrogen) and transferred for 1.5 h (80 V) onto a polyvinylidene difluoride membrane (Millipore) in Tris-glycine transfer buffer containing 20% MeOH and 0.05% SDS. Blots were blocked for 1 h in blocking buffer composed of 5% milk and 0.1% Tween 20 in phosphate-buffered saline (PBS) and then incubated overnight at 4°C in blocking buffer containing primary antibodies against MED12 (1:1000) (Abnova, Taipei, Taiwan; H00009968-A01), MED12 with asymmetrically dimethylated arginine (1:1000; gift from Dr. Mark Bedford and Cell Signaling Technology, Danvers, MA, USA), BAF155 (1:500) (Santa Cruz Biotechnology, Santa Cruz, CA, USA; sc32763), or R1064-dimethylated BAF155 (1:2000) (Millipore; ABE1339). After five washes with 0.1% Tween 20 in PBS, the blots were incubated with goat-anti rabbit (IR800-conjugated; 926-32211) and donkey anti-mouse (IR 680; 926-68072) antibodies (both 1:5000 and from LI-COR Biosciences, Lincoln, NE, USA) in Odyssey blocking buffer (LI-COR

Biosciences) for 1 h at room temperature, and washed five times with 0.1% Tween 20 in PBS. The signal was detected on an Odyssey scanner (LI-COR Biosciences) at 800 and 700 nm.

Cultured MM cells were harvested and lysed in ice-cold SDS lysis buffer composed of 62.5 mM Tris-HCl (pH 7.5), 1% SDS, and 10% glycerin. The lysates were separated by SDS-polyacrylamide gel electrophoresis and transferred to a nitrocellulose membrane using an iBlot Transfer Stack and iBlot Gel Transfer Device (Thermo Fisher Scientific, Waltham, MA, USA). After incubation with StartingBlock T20 PBS blocking buffer (Pierce, Rockford, IL, USA), the membrane was incubated overnight at 4°C with primary antibodies against BAF155 (1:1000) (Cell Signaling Technology; 11956) and dimethyl-BAF155 (1:1000) (Millipore; ABE1339) in Can Get Signal solution 1 (Toyobo Life Science, Osaka, Japan). After five washes with 0.1% Tween 20 in PBS, the blots were incubated with horseradish peroxidase-conjugated anti-rabbit IgG (1:5000) (Cell Signaling Technology; 7074) in Can Get Signal solution 2 (Toyobo Life Science) for 30 min at room temperature and washed five times with 0.1% Tween 20 in PBS. The membrane was incubated with ImmunoStar LD (Wako Pure Chemical Industries, Osaka, Japan), and signals were detected with an ImageQuant LAS-3000 imaging system (Fujifilm, Tokyo, Japan).

Cell proliferation assay

Cells were seeded in tissue culture plates and TP-064 was added immediately or after 24 h (described in Table 9). After 72 or 144 h, cell viability was evaluated based on intracellular ATP concentrations using the CellTiter-Glo luminescent cell viability kit (Promega, Madison, WI, USA). Chemiluminescence was measured with a microplate reader. IC_{50} values were calculated by 4-parameter logistic regression using GraphPad Prism software. K562 cells were cultured in RPMI 10% FBS. Cell viability was determined on MACSquant (Miltenyi) flow cytometer by SytoxBlue (Invitrogen) dye exclusion. The drug response effects were calculated by using GraphPad Prism software fractional response calculations.

siRNA transfection

The following siRNAs were obtained from Thermo Fisher Scientific: non-silencing (Silencer negative control siRNA#2, AM4637), siPRMT4#1 (Silencer select CARM1, s20579), siPRMT4#2 (Silencer select CARM1, s20577). siRNAs were transfected into cells using GenomeONE-Si (Ishihara Sangyo) following the manufacturer's protocol. Statistical comparisons were carried out using the Aspin–Welch's t-test.

Quantitative reverse transcription–polymerase chain reaction (RT-PCR) analysis

Following the designated treatment, total RNA was isolated from cells and purified using an RNeasy Mini Kit (Qiagen). Reverse transcription reactions were performed using a Verso cDNA synthesis kit (ThermoFisher Scientific). Quantitative real-time PCR analysis was performed with a ViiA7 system (Applied Biosystems, Foster City, CA) and TaqMan Fast Advanced Master Mix with TaqMan probes against indicated genes (Applied Biosystems). The 2–ΔΔCt method was applied to analyze the data, using GAPDH mRNA expression as an internal control. The normalized abundance of target mRNAs was expressed relative to the corresponding value for cells treated with non-silencing siRNAs. The following TaqMan probes were used for quantitative RT-PCR analysis: PRMT4 (Hs1092577_m1, Thermo Fisher Scientific), GAPDH (4333764T, Thermo Fisher Scientific).

Ion ampliseq transcriptome analysis

Total RNA was isolated and purified from KMS-11, KMS-20, KMS-26, KMS-27, KMS-28BM, MM.1R, MM.1S, NCI-H929, RPMI8226, and U266B1 cells using an RNeasy Mini kit (Qiagen, Valencia, CA, USA). A total of 10 ng RNA was reverse transcribed using the Ion AmpliSeq Transcriptome Human Gene Expression kit (Thermo Fisher Scientific) following the manufacturer's protocol. cDNA libraries were amplified and barcoded using Ion AmpliSeq Transcriptome Human Gene Expression core panel and Ion Xpress Barcode Adapter (Thermo Fisher Scientific). The prepared libraries were purified using Agencourt AMPure XP (Beckman Coulter), quantified with the Ion

Library TaqMan Quantitation kit (Thermo Fisher Scientific), diluted to 75 pM, and pooled equally. Emulsion PCR, enrichment, and loading were performed on an Ion Chef Instrument. Templated libraries were sequenced on an Ion Proton system using the Ion P1 Hi-Q Chef kit and the Ion P1 Chip kit v.3 (Thermo Fisher Scientific). Ion Proton reads were analyzed using the AmpliSeqRNA analysis plugin (v.5.2.1.2) in Torrent Suite software (Thermo Fisher Scientific). The data are publically available via the NCBI GEO database (GSE110180).

Cell cycle analysis

To measure DNA content for cell cycle distribution analysis, cells were incubated with 70% ethanol/PBS (v/v) overnight. Fixed cells were stained with propidium iodide and analyzed on a FACS LSRFortessa system (BD Biosciences, Franklin Lakes, NJ, USA).

Results and Discussion

Identification and characterization of the selective PRMT4 inhibitor TP-064

TP-064 was developed as a small-molecule inhibitor of PRMT4 (Figure 18A) by chemically optimizing seed compounds identified by high-throughput chemical library screening with a methyltransferase. I found that TP-064 inhibited the methyltransferase activity of PRMT4, with an IC_{50} value of < 10 nM (Figure 18B). The binding of TP-064 to PRMT4 was confirmed by differential static light scattering (DSLS), with aggregation temperature (Tagg) increasing by about 6°C at 80 μM (Figure 18C). Surface plasmon resonance (SPR) analysis revealed that binding only occurred in the presence of S-adenosyl methionine (SAM), yielding a Kd value of 7.1 ± 1.8 nM, with k_{on} = 1.1 ± 0.1 × 10^5 $M^{-1}s^{-1}$ and k_{off} = 0.7 ± 0.1 × 10^{-3} s^{-1} from kinetic fitting (Figure 18D). The steady state response and 1:1 binding model fitting is also presented in Figure 18E. A similar binding profile was also obtained in the presence of S-adenosyl-L-homocysteine (SAH) (Figure 19). The observation that the presence of SAM is required for TP-064 binding suggests that SAM binds first, and PRMT4 may follow a similar ordered kinetic mechanism as reported by Brown et. al. for PRMT1 [90]. I found that switching the terminal aminomethyl (TP-064) to a methoxy moiety to obtain N-((2-(1-(2-methoxyethyl)piperidin-4-yl)pyridin-4-yl)methyl)-N-methyl-3-phenoxybenzamide (TP-064N) clearly reduced the inhibitory activity against PRMT4 (IC_{50} 2.5 ± 0.6 μM; Figure 18B). TP-064N binding to PRMT4 was not observed by DSLS (Figure 18C). The high structural similarity and marked difference in potency indicated that TP-064N could serve as a negative control compound for TP-064.

Selectivity of TP-064 against all known human PRMTs except for PRMT2, which was not active in my experiment, was evaluated. As summarized in Figure 20A, TP-064 showed high selectivity for PRMT4 over other PRMTs (> 100 fold) (Figure 20A). It was inactive against the other family members (IC_{50} > 10 μM) except for PRMT6 (IC_{50} of 1.3 ± 0.4 μM), which is the most structurally related to PRMT4 among PRMT family [91] and PRMT8 (IC_{50} of 8.1 ± 0.6 μM). To further assess the selectivity of TP-064, I tested it against 24 protein lysine methyltransferases and DNA

methyltransferases. TP-064 did not inhibit any of these methyltransferases up to 10 μM (Figure 20A). Negative control compound TP-064N was completely inactive against other methyltransferases (Figure 20A).

To determine the mode of inhibition of TP-064, we investigated the effects of the cofactor SAM and substrate peptide concentration on the IC_{50} values of TP-064 against PRMT4. Increasing SAM or peptide concentration did not significantly affect the IC_{50} values of TP-064 against PRMT4 (Figure 20B), suggesting a non-competitive mode of inhibition, which was previously reported for other inhibitors of methyltransferases including PRMT4 [74] that target the substrate-binding pocket [78, 92].

Next I evaluated the effect of TP-064-mediated inhibition of endogenous PRMT4 in cell-based assays. BRG1-associated factor (BAF)155 and Mediator complex subunit (MED)12 are direct substrates of PRMT4; arginine dimethylation of these proteins is drastically reduced in PRMT4-deficient cells [71, 93]. It was found that TP-064 treatment reduced dimethylation of BAF155 (IC_{50} = 340 ± 30 nM) and MED12 (IC_{50} = 43 ± 10 nM) in a dose-dependent manner (Figure 21), whereas TP-064N up to concentrations of 10 μM did not inhibit BAF155 and MED12 dimethylation (Figure 22). Differences in cellular IC_{50} values for various PRMT4 substrates are not unexpected, as the binding affinities of different substrates could be significantly different as well as the slow substrate turnover rates such as they have been reported for BAF155 complex components [94] could result in higher IC_{50} values. These results indicate that TP-064 is a potent, highly selective, and cell-active PRMT4 inhibitor that can serve as a useful tool for studying the physiological and pathological functions of PRMT4.

Co-crystal structure of PRMT4 in complex with TP-064

To clarify the molecular mechanism of TP-064 inhibition, a co-crystal structure of the catalytic domain of human (h)PRMT4 with TP-064 and the cofactor product SAH was obtained, and a structure was determined at 1.88 Å resolution (PDB code 5U4X) (Figure 23A); the crystal diffraction

data and refinement statistics are shown in Table 10. The structure showed that TP-064 was bound to the substrate-binding site adjacent to SAH. The methylaminoethyl tail of TP-064 occupied the arginine-binding pocket and formed three hydrogen bonds with PRMT4: two were between the side chain of Glu258 and backbone carbonyl group of Met260, and one was between N1 and the side chain of His415, suggesting the importance of this moiety for strong PRMT4 inhibition. The other moieties of TP-064 engaged in hydrogen bonding with the side chain of Asn266 and hydrophobic interactions (Figure 23A).

To determine the structural basis for the observed selectivity of TP-064 for PRMT4 over other PRMTs, a docking model of this compound in complex with PRMT3 and PRMT6 with Glide [95] was generated using the crystal structure of rat (r) PRMT3 (PDB code 1F3L) and hPRMT6 (PDB code 5E8R). In the PRMT4 complex, TP-064 engaged in a π-stacking interaction with Phe153 and formed a hydrogen bond with Asn266 (Figure 23B). The π-stacking was lost with PRMT6 (Figure 23C), and both interactions were lost with PRMT3 (Figure 23D). Hydrophobic interactions with Pro473, Phe475, and water-mediated hydrogen bonding with Lys471 and Ser146 were also observed only with PRMT4. These results were supported by molecular dynamics and molecular mechanics/generalized Born surface area calculations, which showed that the binding energy of TP-064 was stronger with PRMT4 than with PRMT3 and 6 (Table 11). These observations suggest that structural features determine the specific inhibition by TP-064 of PRMT4 over other Type I PRMTs.

Although a clear pattern of competitive inhibition for TP-064 was not observed (Figure 20B), the crystal structure showed that TP-064 occupied the substrate-binding site of PRMT4. This was not unexpected, since a similar pattern was previously reported for inhibitors of PRMT4 [74] and other methyltransferases [78, 92]. It was suggested that in such cases the binding affinity of the peptide substrate is derived from regions outside the arginine-binding pocket. Thus, TP-064 can occupy this pocket without interfering with substrate-PRMT4 binding to form the substrate-TP-064-PRMT4 complex.

TP-064 inhibits MM cell proliferation

To evaluate the effects of TP-064 on cancer cell proliferation, I tested a panel of 89 (69 solid and 20 hematologic) cancer cell lines (Table 9). The cells were treated with 3 μM TP-064 for 3 days and viability was evaluated based on intracellular ATP concentration. TP-064 inhibited the growth of a subset of MM cell lines (red dots in Figure 24A). To confirm this result, I carried out a dose titration experiment for a longer treatment period—*i.e.*, 12 MM cell lines were cultured with TP-064 for 6 days. TP-064 treatment inhibited the growth of NCI-H929, RPMI8226, and MM.1R cells in a dose-dependent manner (Figure 24B), but had no effect on acute myeloid leukemia, colon cancer, or lung cancer cell lines (Figure 25), suggesting that the efficacy of TP-064 was dependent on the context. As expected, TP-064N did not affect cell growth of MM cells (Figure 26). In addition, to further validate the role of PRMT4 in MM cell growth, we performed PRMT4 knockdown in NCI-H929 cells and observed PRMT4 knockdown-induced growth inhibition (Figure 27). Thus, pharmacological inhibition of PRMT4 by small molecules may be a therapeutic option for some MM treatment.

To identify a biomarker for predicting the sensitivity of MM cells to TP-064 treatment, I obtained the steady-state transcriptome data of the MM cells used in the growth inhibition assay (GSE110180). At first, the correlation between sensitivity to TP-064 and PRMT4 mRNA expression was investigated. However, the anti-proliferative effect of TP-064 was not associated with PRMT4 mRNA levels in the tested cancer cell lines ($R_2 = 0.15$; Figure 24C). This indicates that the sensitivity of cancer cells to TP-064 cannot be predicted solely by their expression of PRMT4, and involves other proteins or pathways. Further analysis of the gene expression data in the TP-064 sensitive cells and insensitive cells may shed light on sensitivity markers for the TP-064 treatment in MM cells.

Pharmacodynamic biomarker inhibition by TP-064 in MM cells

To confirm the inhibition of PRMT4 activity in TP-064-sensitive and insensitive MM cells, the dimethylation level of BAF155, as a pharmacodynamic biomarker upon TP-064 treatment, was examined. TP-064-sensitive NCI-H929 and TP-064-insensitive KMS-27 and U266B1 cells were

treated with various concentrations of TP-064 or TP-064N for 72 h and cell lysates were evaluated by western blotting to determine the expression and dimethylation levels of BAF155. Dimethyl-BAF155 level was reduced by TP-064 treatment in a dose-dependent manner in both TP-064-sensitive and -insensitive cells (Figure 28A), whereas TP-064N had no effect. The fact that the observed reduction by TP-064 was not correlated with TP-064 sensitivity suggests that the mechanism of action of TP-064 does not involve BAF155 dimethylation. Although dimethyl-BAF155 cannot be used as a biomarker for predicting TP-064 efficacy, it can nonetheless be used to monitor target inhibition in future pre-clinical and clinical studies of PRMT4 inhibitors.

TP-064 induces G1 cell cycle arrest in NCI-H929 cells

To clarify the mechanism of TP-064-induced growth inhibition in MM cells, I analyzed cell cycle by flow cytometry. TP-064 treatment reduced the proportion of NCI-H929 cells in S and G2/M phases while increasing the G1 phase fraction (Figure 28B). TP-064N treatment showed no/little effect on cell cycle of the cells. These results imply that PRMT4 inhibition by TP-064 induced G1 cell cycle arrest, although the underlying mechanism remains to be determined. Given that PRMT4 is known to be involved in multiple biological functions and has a wide range of histone and non-histone substrates, comprehensive analyses of the transcriptome, proteome, and methylome and chromatin immunoprecipitation sequencing in TP-064-treated cells can provide insight into the regulation of PRMT4-mediated growth and survival in MM cells as well as biomarkers for evaluating the efficacy of PRMT4 inhibitors.

Recently, CRISPR-based genetic screening has revealed a synergistic interaction between PRMT4 and the histone lysine methyltransferase Disruptor of telomeric silencing 1-like (DOT1L) in the K562 chronic myelogenous leukemia cell line [96]. Although K562 cells have no response to DOT1L inhibitor SGC0946 and a weak response to TP-064 but not TP-064N, the combination of DOT1L inhibitor SGC0946 and TP-064 but not TP-064N elicited a stronger cytotoxic response (Figure

29), suggesting that PRMT4 can be combined with other agents for cancer treatment. Further study is needed to reveal the mechanism of synergistic interaction between PRMT4 and DOT1L.

Conclusion

In this study, I have identified TP-064, a novel potent, selective, and cell-active PRMT4 inhibitor and its inactive analog TP-064N. TP-064 had anti-proliferative effects in a subset of MM cell lines and potential synergistic activity with another methyltransferase (DOT1L). These results suggest that small molecule inhibitors of PRMT4 can serve as tools for investigating PRMT4 pharmacology in health and disease and may be used to treat MM and other forms of cancer, including in combination with conventional drugs.

Figures and Tables

Figure 18

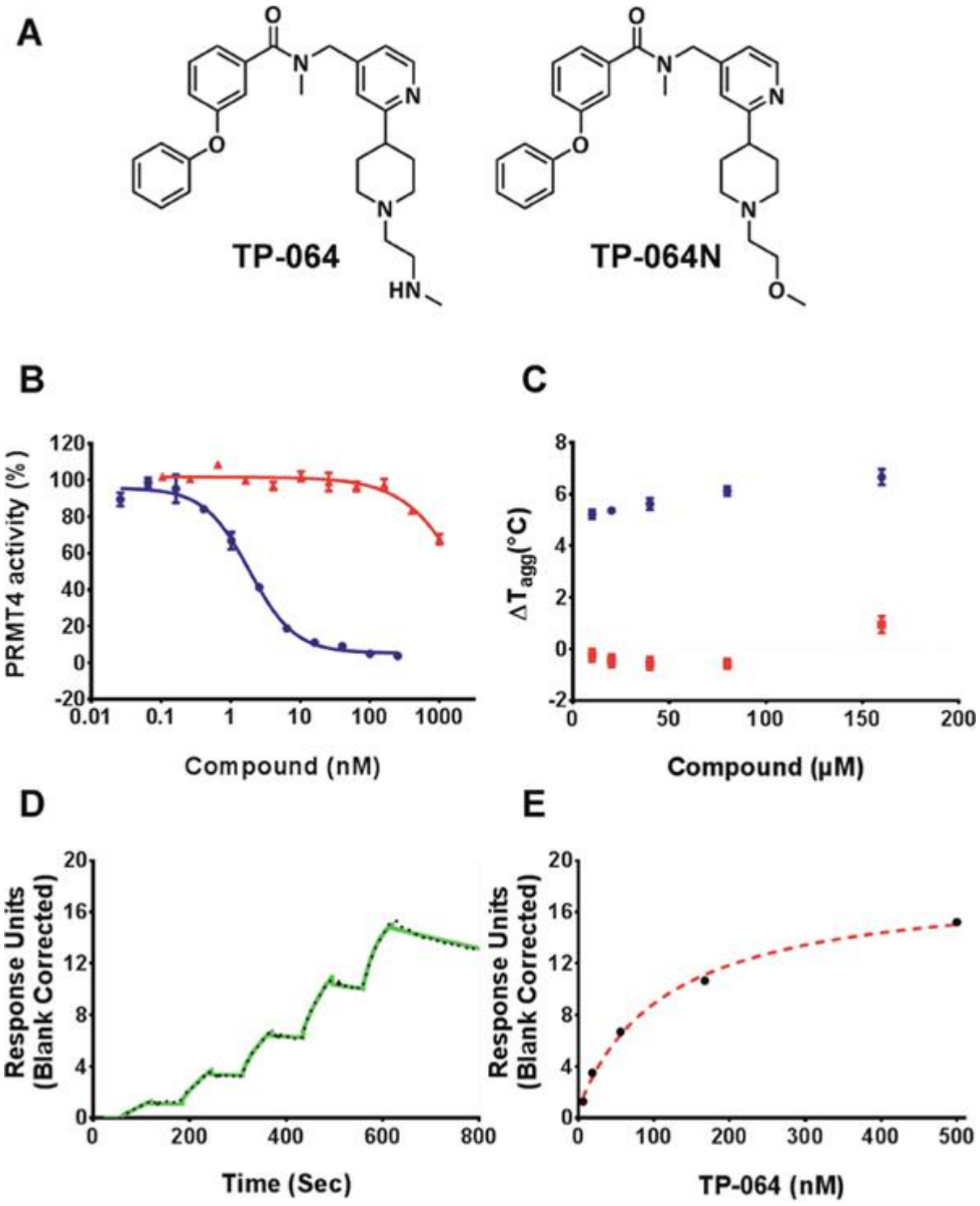

Figure 18. TP-064 is a potent inhibitor of PRMT4.

(A) Chemical structure of TP-064 and its negative control, TP-064N. (B) TP-064 (blue) inhibits PRMT4 activity with an IC_{50} value of < 10 nM under balanced conditions. TP-064N (red) has no effect on PRMT4 activity up to 100 nM. (C) The binding of TP-064 to PRMT4 was confirmed by DSLS with stabilization at about 6°C. No binding was observed with TP-064N. (D, E) SPR analysis of the TP-064 binding to PRMT4 in the presence of 50 μM SAM. (D) A representative sensorgram (black dots) is shown with the kinetic fit (solid green). A Kd value of 7.1 ± 1.8 nM, with k_{on} = 1.1 ± 0.1 × 10^5 M^{-1} s^{-1} and k_{off} = 0.7 ± 0.1 × 10^{-3} s^{-1}, was obtained from triplicate experiments. (E) The steady state response (black circles) and 1:1 binding model fitting (red dashed line) is presented.

Figure 19

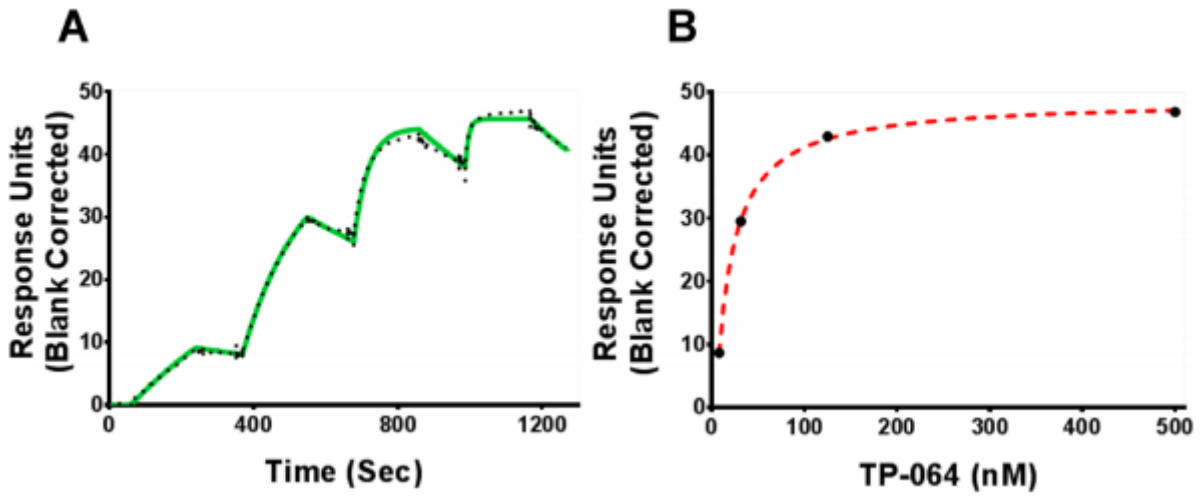

Figure 19. SPR analysis of TP-064 binding to PRMT4 in the presence of 50 µM SAH.

(A) A representative sensorgram (black dots) is shown with the kinetic fit (solid green). A K_d value of 6.9 ± 1.1 nM, with k_{on} = 2.02 ± 0.03 × 10^5 M^{-1} s^{-1} and k_{off} = 1.4 ± 0.2 × 10^{-3} s^{-1}, was obtained from triplicate experiments. (B) The steady state response (black circles) and 1:1 binding model fitting (red dashed line) is presented.

Figure 20

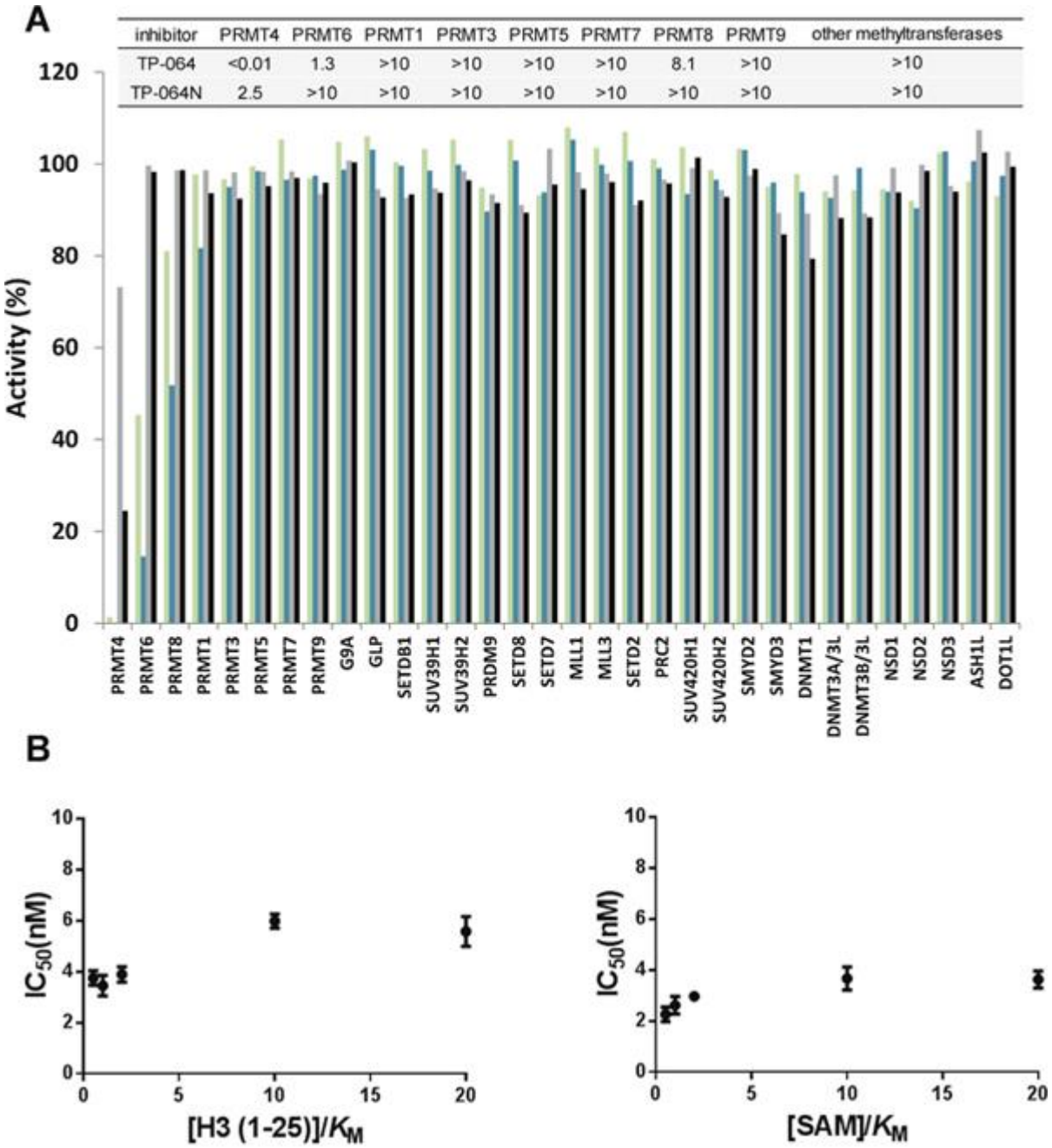

Figure 20. Selectivity and mechanism of action of TP-064.

(A) Selectivity of TP-064N at 10 μM (■) and 1 μM (■) and of TP-064 at 10 μM (■) and 1 μM (■) for PRMT1, 3, 4, 5, 6, 7, 8, and 9 as well as for 24 histone and DNA methyltransferases was assessed. Dose response data are presented in the top panel as IC_{50} (μM). (B) Mechanism of action of TP-064 was assessed by determining IC_{50} of both substrates values at various concentrations.

Figure 21

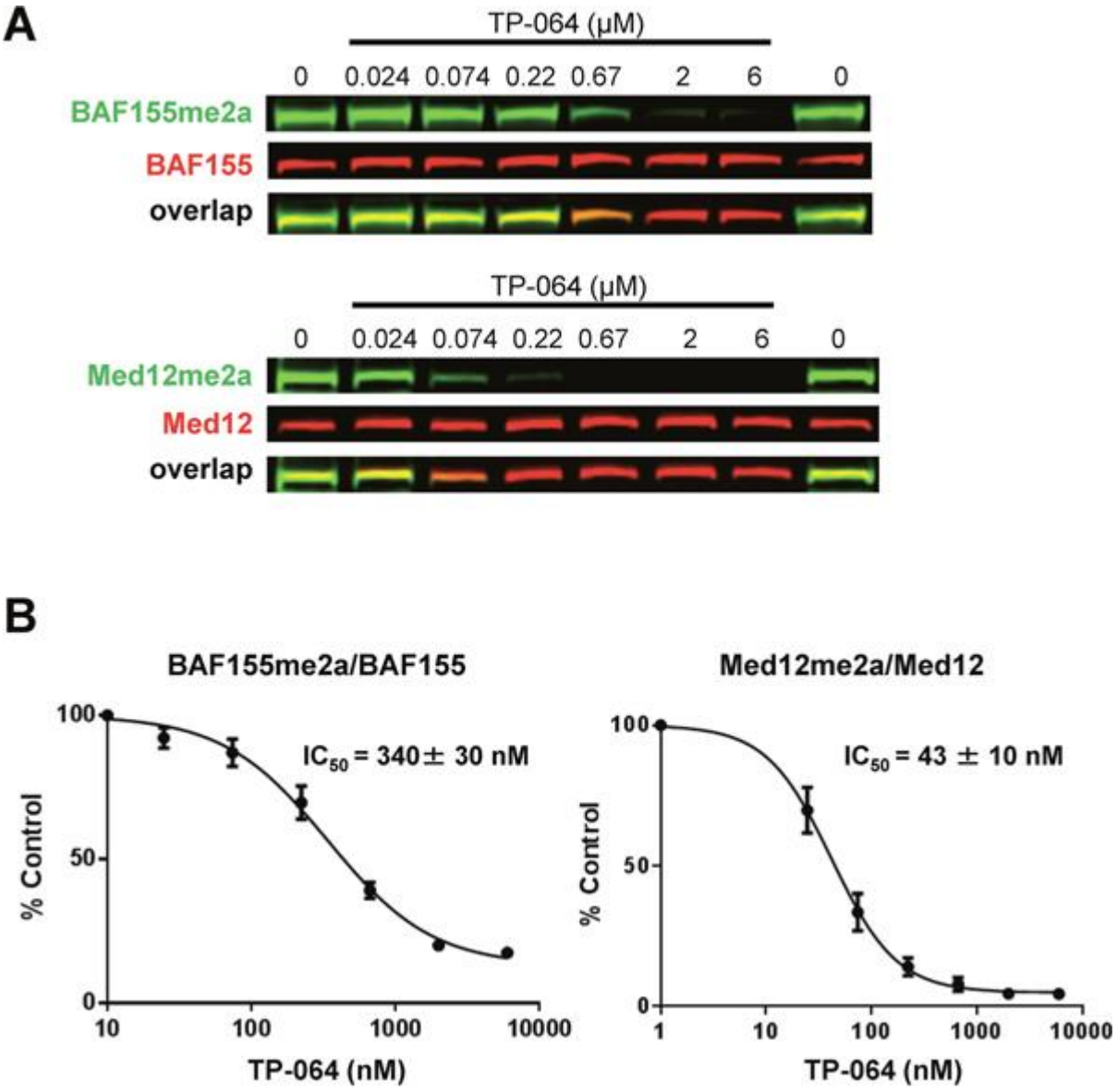

Figure 21. TP-064 inhibits PRMT4 substrate methylation in cells.

(A) TP-064 inhibits the dimethylation of PRMT4 substrates. HEK293 cells were treated with indicated concentrations of TP-064 for 3 days and dimethylation levels of BAF155 and MED12 in whole cell extracts were analyzed by western blotting. (B) Quantitation of data in (A). Graphs represent nonlinear curve fits of dimethyl-BAF155 and dimethyl-MED12 signal intensities normalized to total BAF155 or MED12, respectively. Data represent mean ± SEM of two independent experiments prepared in triplicate.

Figure 22

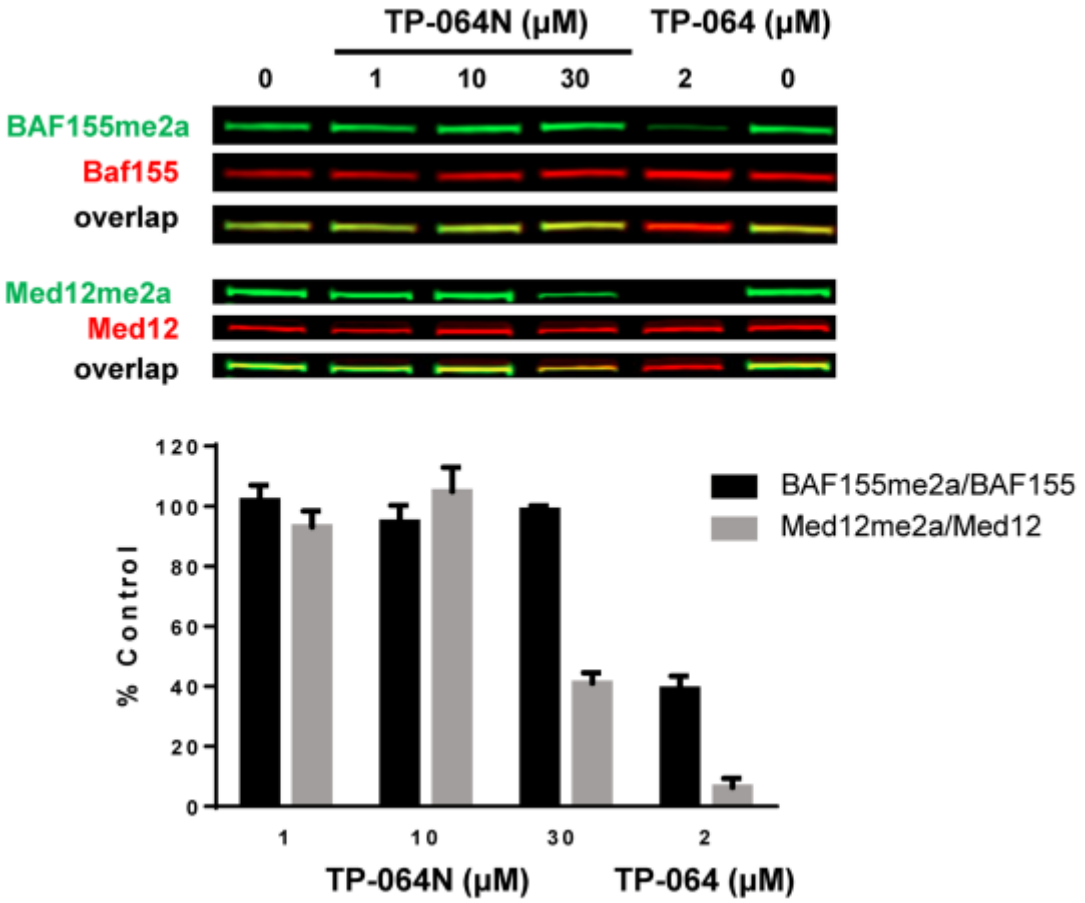

Figure 22. Effect of TP-064N on PRMT4 cellular activity.

TP-064N did not inhibit the methylation of BAF155 or MED12 up to 10 μM. HEK293 cells were treated with indicated concentration of TP-064 and TP-064N for 3 days and whole cell extracts were analyzed by western blotting for dimethylation of BAF155 R1064 and MED12 R1862.

Figure 23

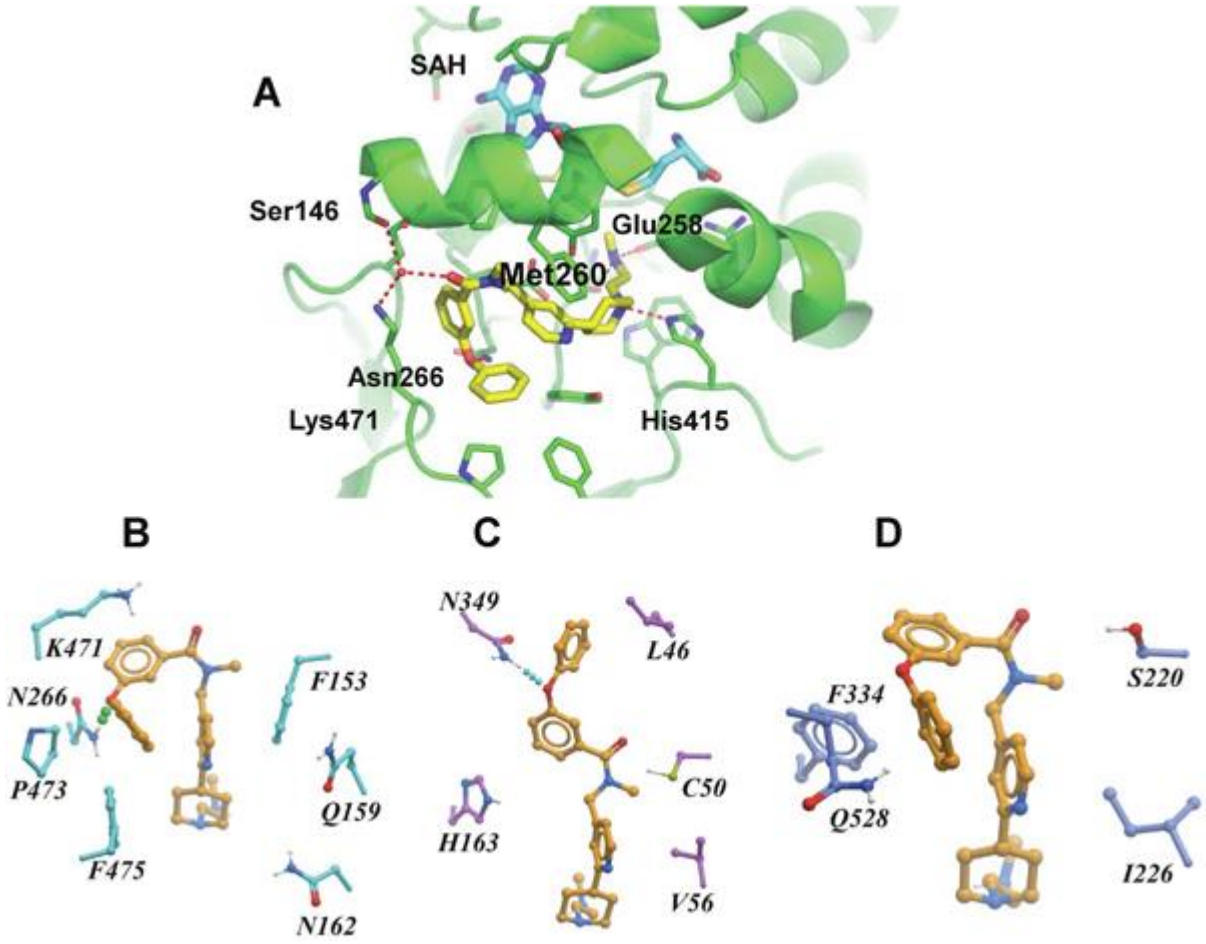

Figure 23. X-ray crystal structure and binding mode of TP-064, SAH, and PRMT4.

(A) Ribbon diagram of X-ray co-crystal structure of PRMT4 in complex with TP-064 and SAH (PDB code: 5U4X). (B–D) Binding mode of TP-064 against PRMT4 (B) and predicted binding mode of TP-064 against PRMT6 (C) and PRMT3 (D) are shown as stick diagrams. Residues in the active site are shown as cyan sticks. Dashed lines represent intermolecular hydrogen bonds.

Figure 24

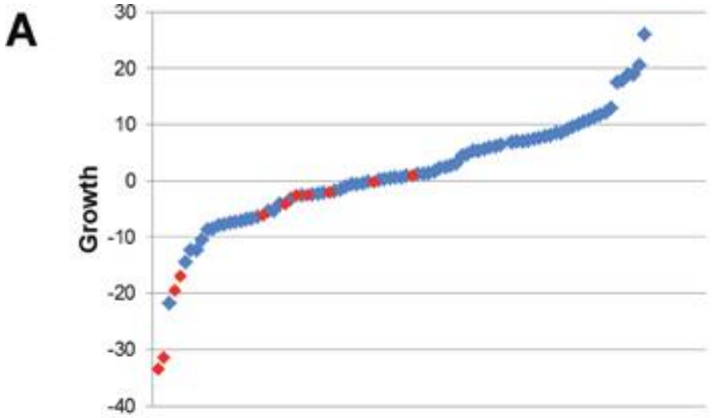

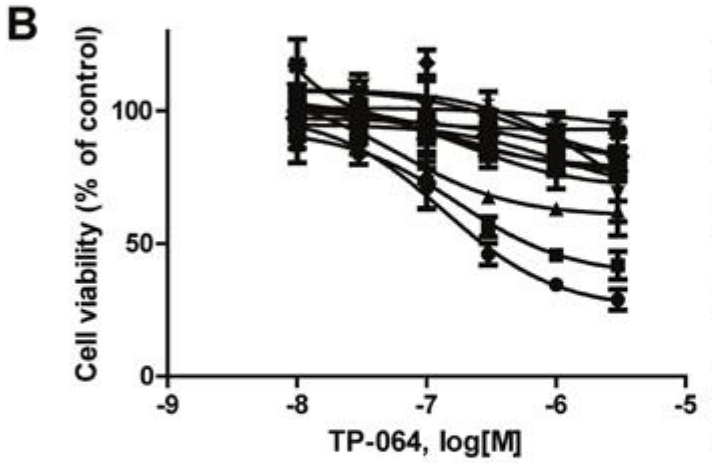

cell line	Growth at 3 μM (%)	IC_{50} (nM)
NCI-H929	-71.2	379
RPMI8226	-58.3	886
MM.1R	-37.8	N.A.
MM.1S	-31.0	N.A.
U266B1	-24.4	N.A.
KMS-28BM	-24.1	N.A.
KMS-20	-22.5	N.A.
KMS-26	-19.5	N.A.
KMS-11	-17.2	N.A.
KMS-27	-17.2	N.A.
KMS-12BM	-8.2	N.A.
KMS-12PE	-4.4	N.A.

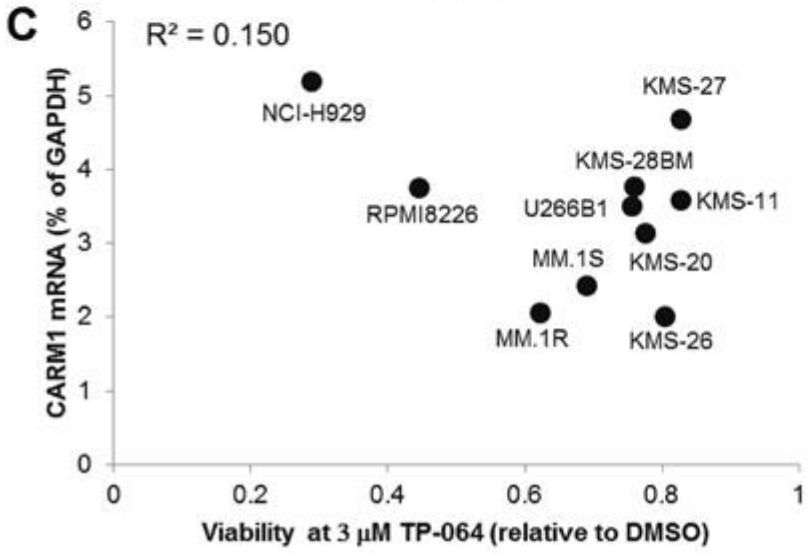

Figure 24. TP-064 inhibits growth in multiple myeloma (MM) cell lines.

(A) A panel of 89 different cancer cell lines was cultured with 3 μM TP-064 for 3 days and cell viability was determined with the CellTiter-Glo assay. Decrease in viability relative to DMSO-treated cells was defined as growth inhibition and is shown as a water-fall plot (n = 3). Red dots indicate MM cell lines. (B) MM cells were treated with TP-064 for 6 days and cell growth was assayed with CellTiter-Glo. Data are presented as mean ± standard deviation (n = 3). IC_{50} values were calculated by nonlinear regression analysis of % inhibition. TP-064 inhibits the growth of NCI-H929, RPMI8226, and MM.1R cells in a dose-dependent manner. (C) Correlation between the antiproliferative activity of TP-064 and *PRMT4* mRNA expression in MM cell lines. X and Y axes indicate the relative ATP level at 3 μM TP-064 and *PRMT4* mRNA levels in the 10 indicated MM cell lines, respectively. ATP concentration was calculated based on chemiluminescence values relative to the 0 nM value (control) in each cell line. *PRMT4* mRNA expression levels in MM cells were determined with the Ion Ampliseq transcriptome assay and were normalized to that of glyceraldehyde 3-phosphate dehydrogenase (GAPDH) in each cell line.

Figure 25

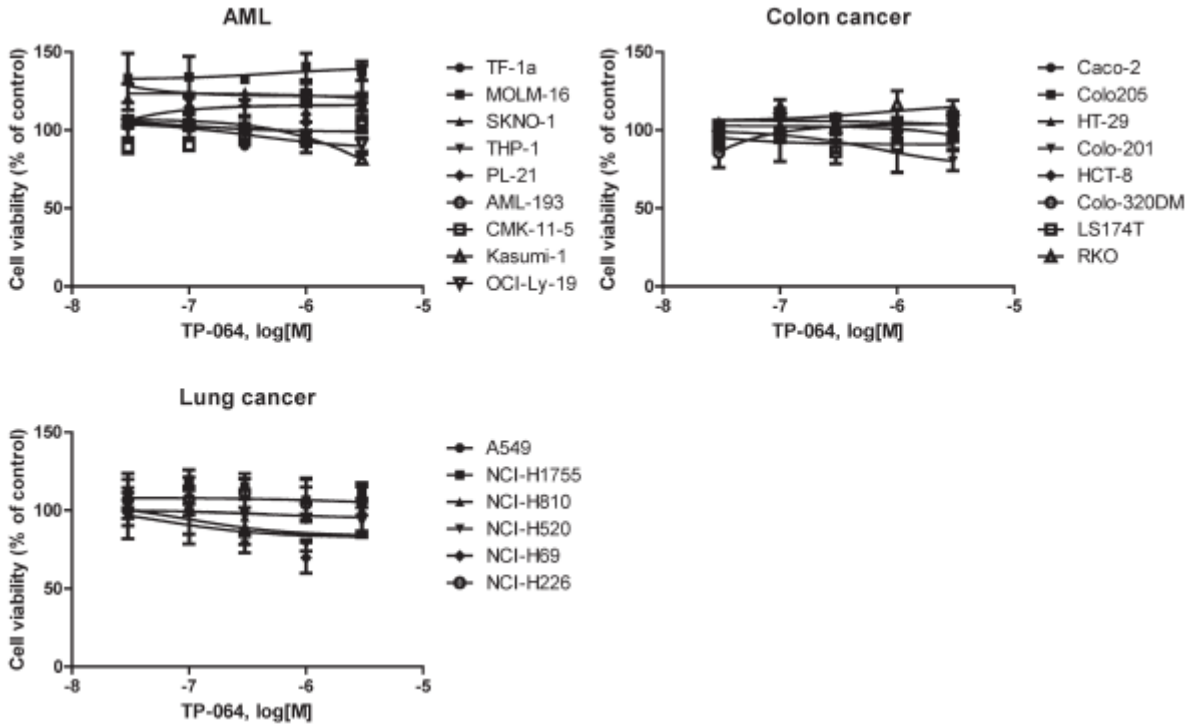

Figure 25. Effect of TP-064 on proliferation of various cancer cell lines.

TP-064 did not exhibit anti-proliferative activity in acute myeloid leukemia, colon cancer, or lung cancer cell lines treated with indicated concentrations of TP-064 for 6 days. Relative ATP concentration was calculated based on chemiluminescence relative to the 0 nM value (control). Data are presented as mean ± standard deviation (n = 3).

Figure 26

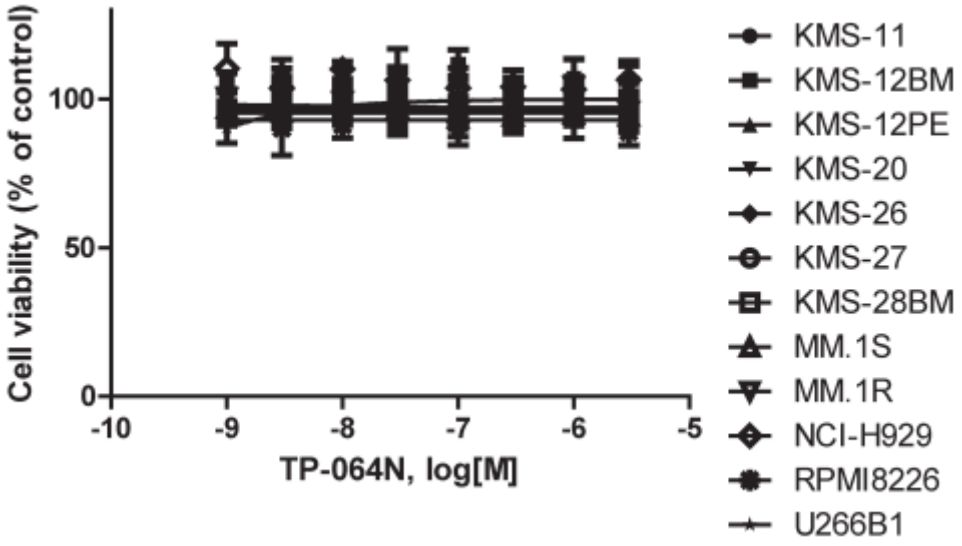

Figure 26. TP-064N does not affect the cell growth of MM cell lines.

MM cells were treated with indicated concentration of TP-064N for 6 days and cell viability was measured by CellTiter-Glo luminescent cell viability kit. Data are presented as mean ± standard deviation (n = 3).

Figure 27

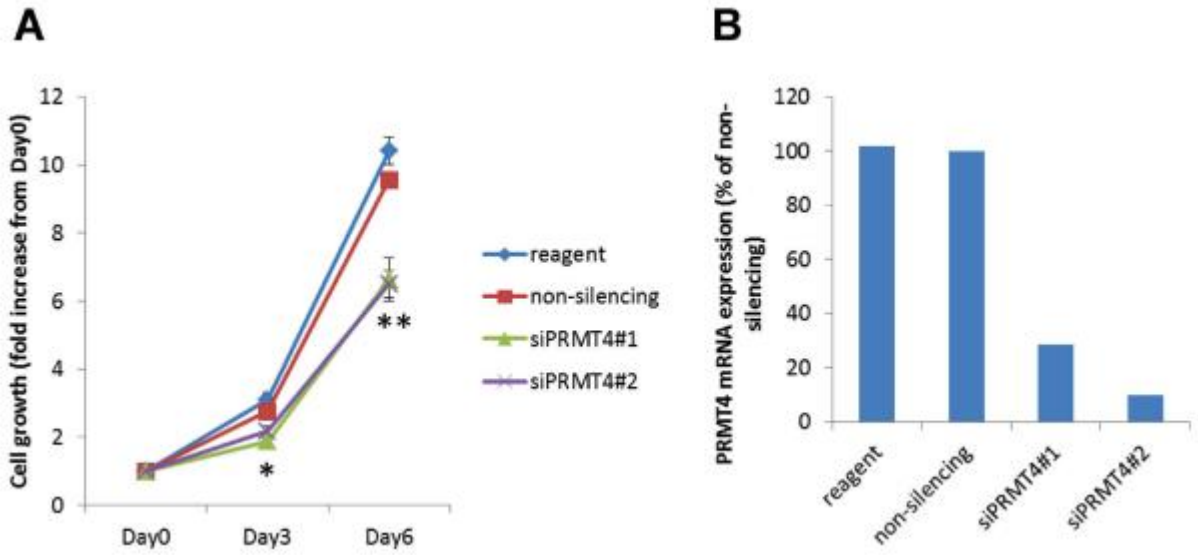

Figure 27. PRMT4 knockdown inhibited NCI-H929 cell growth.

NCI-H929 cells were transfected with siPRMT4 and cultured indicated period. (A) Cell viabilities were evaluated at day 3 and day 6 by CellTiter-Glo luminescent cell viability kit. Data are presented as mean ± SD (n = 4). *P < 0.01, **P < 0.001, significant differences with the Aspin-Welch's t-test when compared with the values of the non-silencing control. (B) Total RNA was isolated from cells at day3 and PRMT4 mRNA expression was evaluated by quantitative RT-PCR.

Figure 28

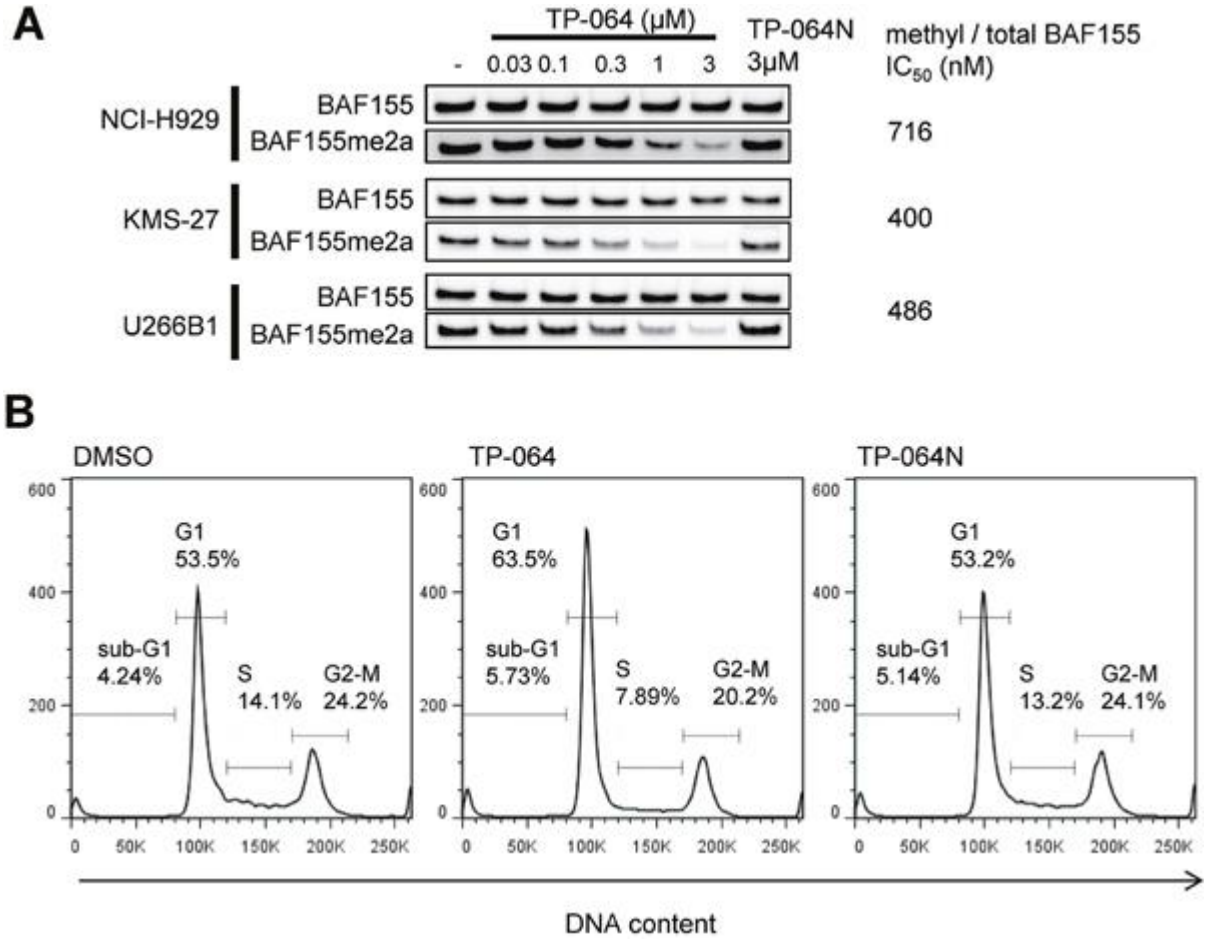

Figure 28. Cellular responses of MM cells treated with TP-064.

(A) Cells were treated with indicated concentration of TP-064 for 3 days and whole cell extracts were analyzed by western blotting for BAF155 dimethylation. IC_{50} values were calculated by nonlinear regression analysis of % inhibition. (B) NCI-H929 cells were treated with DMSO, 1 μM TP-064 or 1 μM TP-064N for 72 h, and DNA content was determined by flow cytometry. Sub-G1, G1, S, and G2-M cell fractions are indicated.

Figure 29

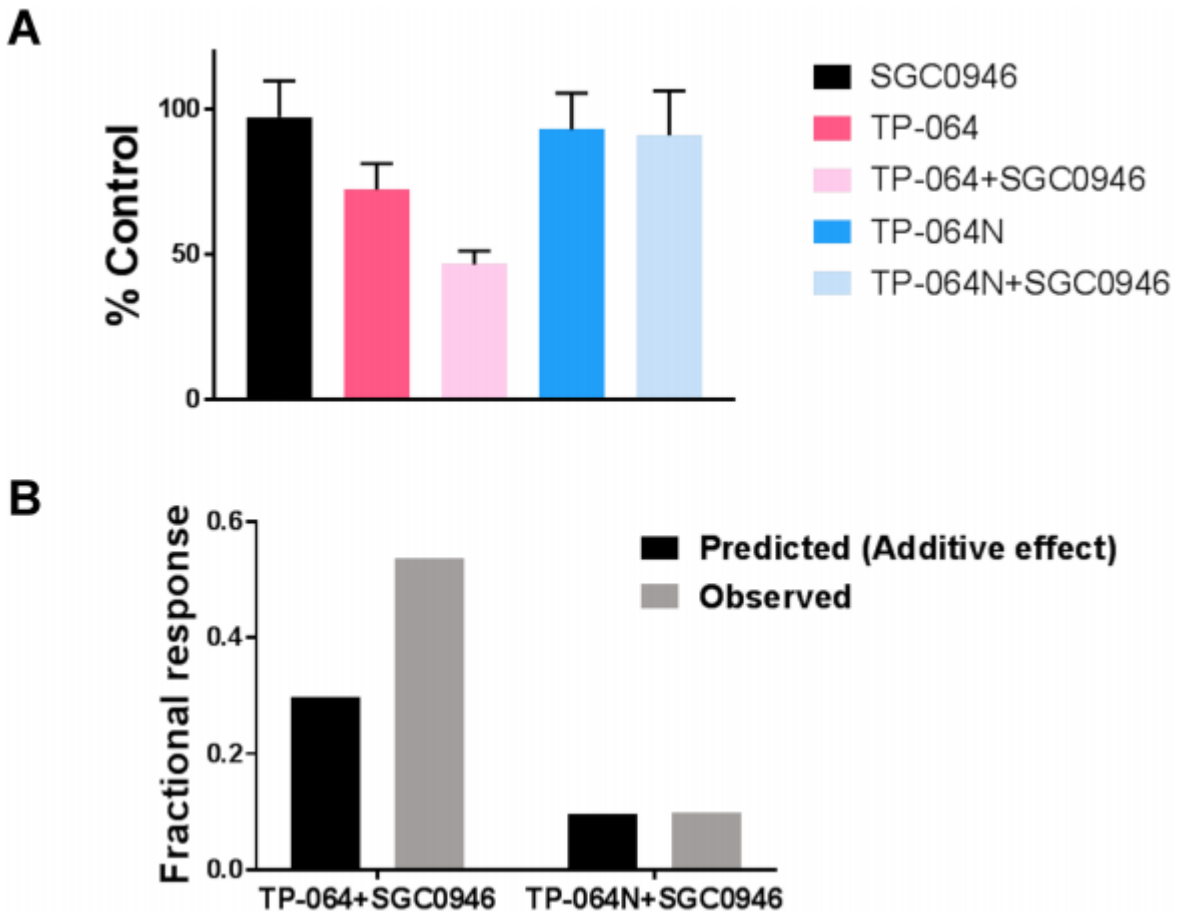

Figure 29. Inhibition of DOT1L (SGC0946) and PRMT4 (TP-064) additively suppresses K562 cell growth.

K562 cells were treated with 3 µM of TP-064 or TP-064N and 5 µM of SGC0946 for 6 days. The inhibitors were topped up after 3 days. After 6 days, cells were stained with SYTOX Blue dead cell stain and the number of viable cells was determined by flow cytometry. Data are presented as mean ± SD (n = 5). The predicted additive effect was calculated as Fa + Fb × (1 − Fa), where Fa and Fb are the fractional responses to TP-064 and SGC0946, respectively.

Table 7. Assay conditions for PRMT enzymatic assays

Enzyme	Protein (nM)	Peptide substrate (μM)	^{3}H-SAM (μM)	SAM (μM)	Buffer	Incubation time at 23°C (min)
PRMT1	15	0.13	2	2.6	20 mM Tris-HCl (pH 8.0), 0.01% Triton X-100, 5 mM DTT	45
PRMT3	20	0.57	4	24.3	20 mM Tris-HCl (pH 7.5), 0.01% Tween-20, 5 mM DTT	45
PRMT4	20	0.74	0.5	1.42	20 mM Bicine (pH 8.5), 0.01% Triton X-100	30
PRMT5-MEP50	15	0.07	0.6	0	20 mM Tris-HCl (pH 8.5), 0.01% Tween-20, 5 mM TCEP	30
PRMT6	50	0.6	1.15	1.15	20 mM BTP (pH 7.5), 0.01% Tween-20, 10 mM DTT	30
PRMT7	25	0.3	1.1	0	20 mM Tris-HCl (pH 8.5), 0.01% Tween-20, 5 mM DTT	45
PRMT8	20	0.7	0.5	1.7	20 mM Tris-HCl (pH 8.0), 0.01% Triton X-100, 5 mM DTT	30
PRMT9	10	0.07	5	32.7	20 mM BTP (pH 7.5), 0.01% Tween-20, 10 mM DTT, 0.5 mM EDTA	20

BTP, Bis-Tris-Propane-HCl; DTT, dithiothreitol; EDTA, ethylenediaminetetraacetic acid; MEP50, methylosome protein 50; PRMT, protein arginine methyltransferase; SAM, S-adenosyl-L-methionine; TCEP, (Tris(2-carboxyethyl)phosphine.

Table 8. Protein constructs used in PRMT enzymatic assays

Protein	GenBank accession number	Number of amino acids in full-length protein	Amino acids covered
PRMT1	NP_001527.3	371	30–371
PRMT3	XP_011518138.1	426	106–426 (within the identical region of the two isoforms)
PRMT4	NP_954592.1	608	1–608
PRMT5-MEP50	NP_006100.2(PRMT5)	637 (PRMT5)	1–637 (PRMT5)
	NP_077007.1 (MEP50)	342 (MEP50)	1–342 (MEP50)
PRMT6	AAH73866.1	375	1–375
PRMT7	NP_061896.1	692	1–692
PRMT8	AAH22458.2	394	1–394
PRMT9	NP_612373.2	845	1–845

MEP50, methylosome protein 50; PRMT, protein arginine methyltransferase

Table 9. Cell lines used in this study

Cell line	Tissue	Tissue Pathology	Source	Catalog Number	Purchased Date	Culture Media	FBS	Supplement	Treatment (time after plating)
786-O	kidney	renal cell adenocarcinoma	ATCC	CRL-1932	2013/9/10	RPMI1640 (Wako, 189-02145)	10%		24 hr
A2780	ovarian	ovarian endometroid adenocarcinoma	DS pharma biomedical	93112519	2008/4/29	RPMI1640 (Wako, 189-02145)	10%	1 mM Sodium Pyruvate (Thermo Fisher, 11360-070)	24 hr
A498	kidney	carcinoma	ATCC	HTB-44	2013/2/19	E-MEM (Wako, 051-07615)	10%	1 mM Sodium Pyruvate (Thermo Fisher, 11360-070) 1x NEAA (Thermo Fisher, 11140-050)	24 hr
A549	lung	carcinoma	ATCC	OCB-33	2013/6/18	F12K (Wako, 080-08565)	10%		24 hr
A704	kidney	adenocarcinoma	ATCC	HTB-45	2014/1/29	E-MEM (Wako, 051-07615)	10%	1 mM Sodium Pyruvate (Thermo Fisher, 11360-070) 1x NEAA (Thermo Fisher, 11140-050)	24 hr
AML-193	peripheral blood	acute monocytic leukemia	ATCC	CRL-9589	2015/1/8	IMDM (Thermo Fisher, 12440-053)	5%	5 ng/mL GM-CSF, 5 µg/mL Insulin, 5 µg/mL Transfelin	24 hr
C2BBe1	colon	colorectal adenocarcinoma	ATCC	CRL-2102	2014/9/25	D-MEM (Wako, 043-30085)	10%	0.01 mg/ml human transferrin	24 hr

CACO-2	colon	colorectal adenocarcinoma	RIKEN	RCB0988	2015/2/25	E-MEM (Wako, 051-07615)	20%	1 mM Sodium Pyruvate (Thermo Fisher, 11360-070) 1x NEAA (Thermo Fisher, 11140-050)	24 hr
Caki-1	kidney:skin	clear cell carcinoma	ATCC	HTB-46	2002/9/10	McCoy's 5A (Wako, 16600-082)	10%		24 hr
Caki-2	kidney	clear cell carcinoma	ATCC	HTB-47	2014/1/21	McCoy's 5A (Wako, 16600-082)	10%		24 hr
CAMA-1	mammary gland/breast	adenocarcinoma	ATCC	HTB-21	2013/5/30	E-MEM (Wako, 051-07615)	10%	1 mM Sodium Pyruvate (Thermo Fisher, 11360-070) 1x NEAA (Thermo Fisher, 11140-050)	24 hr
Caov-3	ovary	adenocarcinoma	ATCC	HTB-75	2013/6/24	D-MEM (Wako, 043-30085)	10%		24 hr
Caov-4	ovary	ovarian carcinoma	ATCC	HTB-76	2015/1/8	L-15 (Thermo Fisher, 11415-064)	20%	7.5 w/v% Sodium Bicarbonate Solution（wako, 195-16411)	24 hr
CMK-11-5	peripheral blood	leukemia,acute megakaryoblastic	JCRB	IFO50430	2014/1/16	RPMI1640 (Wako, 189-02145)	10%		24 hr
COLO201	colon	adenocarcinoma	JCRB	JCRB0226	2015/2/18	RPMI1640 (Wako, 189-02145)	10%		24 hr

COLO-205	colon	Dukes' type D, colorectal adenocarcinoma	ATCC	CCL-222	2008/4/17	RPMI1640 (Wako, 189-02145)	10%	1 mM Sodium Pyruvate (Thermo Fisher, 11360-070)	24 hr
COLO320DM	colon	adenocarcinoma	JCRB	JCRB0225	2015/2/18	D-MEM (Wako, 043-30085)	10%		24 hr
Daudi	blood	lymphoma, Burkitt's	JCRB	JCRB9071	2015/5/13	RPMI1640 (Wako, 189-02145)	10%		24 hr
DMS114	lung	carcinoma; small cell lung cancer	ATCC	CRL-2066	2013/6/5	Waymouth's MB752/1 (Thermo Fisher, 11220-053)	10%		24 hr
DMS53	lung	carcinoma; small cell lung cancer	ATCC	CRL-2062	2013/6/5	Waymouth's MB752/1 (Thermo Fisher, 11220-053)	10%		24 hr
G-401	kidney	rhabdoid tumor (formerly classified as Wilms' tumor)	ATCC	CRL-1441	2014/1/21	McCoy's 5A (Wako, 16600-082)	10%		24 hr
HCT116	colon	colorectal carcinoma	ATCC	CCL-247	2013/2/26	McCoy's 5A (Wako, 16600-082)	10%		24 hr
HCT15	colon	colorectal carcinoma	ATCC	CCL-225	2011/10/25	RPMI1640 (Wako, 189-02145)	10%	1 mM Sodium Pyruvate (Thermo Fisher, 11360-070)	24 hr

HCT-8	colon	ileocecal colorectal adenocarcinoma	ATCC	CCL-244	2015/2/19	RPMI1640 (Wako, 189-02145)	10%		24 hr
HEK293T	kidney	Epithelial from human kidney embryo	Kind gift from Sam Benchimol, York University		2009	DMEM (Thermo Fisher, 11965-092)	10%		immediately
HPAC	pancreas	adenocarcinoma	ATCC	CRL-2119	2014/9/25	F12/DMEM(1:1) (Thermo Fisher, 11330-032)	5%	0.002 mg/ml insulin, 0.005mg/ml transferrin, 40 ng/ml hydrocortisone, 10ng/ml EGF	24 hr
HPAF-Ⅱ	pancreas	adenocarcinoma	ATCC	CRL-1997	2014/3/20	E-MEM (Wako, 051-07615)	10%	1 mM Sodium Pyruvate (Thermo Fisher, 11360-070) 1x NEAA (Thermo Fisher, 11140-050)	24 hr
Hs 746T	stomach	gastric carcinoma	ATCC	HTB-135	2014/9/25	D-MEM (Wako, 043-30085)	10%		24 hr
HT1080	connective tissue	fibrosarcoma	ATCC	CCL-121	2014/6/19	E-MEM (Wako, 051-07615)	10%	1 mM Sodium Pyruvate (Thermo Fisher, 11360-070) 1x NEAA (Thermo Fisher, 11140-050)	24 hr
HT-29	colon	colorectal carcinoma	ATCC	HTB-38	2013/9/25	McCoy's 5A (Wako 16600-082)	10%		24 hr
JEG-3	placenta	choriocarcinoma	ATCC	HTB-36	2014/3/20	E-MEM (Wako, 051-07615)	10%	1 mM Sodium Pyruvate (Thermo Fisher, 11360-070)	24 hr

								1x NEAA (Thermo Fisher, 11140-050)	
K562	bone marrow	chronic myelogenous leukemia	ATCC	CCL-243	2013/11/19	IMDM (Thermo Fisher, 12440-053)	10%		immediately
Kasumi-1	blood	myeloblast	JCRB	JCRB1003	2014/1/16	RPMI1640 (Wako, 189-02145)	10%		24 hr
KATOⅢ	stomach	gastric carcinoma	ATCC	HTB-103	2014/3/20	IMDM (Thermo Fisher, 12440-053)	20%		24 hr
KMM-1	subcutaneous tumor	multiple myeloma	JCRB	JCRB1180	2015/6/10	RPMI1640 (Wako, 189-02145)	10%		immediately
KMS-11	pleural effusion	multiple myeloma	JCRB	JCRB1179	2015/6/24	RPMI1640 (Wako, 189-02145)	10%		immediately
KMS-12-BM	bone marrow	multiple myeloma	JCRB	JCRB0429	2016/2/24	RPMI1640 (Wako, 189-02145)	10%		immediately
KMS-12-PE	pleural effusion	multiple myeloma	JCRB	JCRB0430	2016/2/24	RPMI1640 (Wako, 189-02145)	10%		immediately
KMS-20	blood	multiple myeloma	JCRB	JCRB1196	2015/6/10	RPMI1640 (Wako, 189-02145)	10%		immediately

KMS-26	pleural effusion	multiple myeloma	JCRB	JCRB1187	2015/6/10	RPMI1640 (Wako, 189-02145)	10%		immediately
KMS-27	peripheral blood	multiple myeloma	JCRB	JCRB1188	2015/6/24	RPMI1640 (Wako, 189-02145)	10%		immediately
KMS-28BM	bone marrow	multiple myeloma	JCRB	JCRB1192	2015/6/10	RPMI1640 (Wako, 189-02145)	10%		immediately
KYSE70	esophagus	squamous cell carcinoma	JCRB	JCRB0190	2014/3/19	D-MEM (Wako, 043-30085)	2%		24 hr
LS174T	colon	Dukes' type B,colorectal adenocarcinoma	ATCC	CL-188	2014/7/29	E-MEM (Wako, 051-07615)	10%	1 mM Sodium Pyruvate (Thermo Fisher, 11360-070) 1x NEAA (Thermo Fisher, 11140-050)	24 hr
MCF-7	mammary gland/breast	adenocarcinoma	JCRB	JCRB0134	2015/8/5	RPMI1640 (Wako, 189-02145)	10%	1 mM Sodium Pyruvate (Thermo Fisher, 11360-070)	24 hr
MDA-MB-231	mammary gland/breast	adenocarcinoma	ATCC	HTB-26	2002/11/13	D-MEM (Wako, 043-30085)	10%		24 hr
MDA-MB-361	mammary gland/breast	adenocarcinoma	ATCC	HTB-27	2009/1/14	L-15 (Thermo Fisher, 11415-064)	20%	7.5 w/v% Sodium Bicarbonate Solution（wako, 195-16411)	24 hr
MDA-MB-468	mammary gland/breast	adenocarcinoma	ATCC	HTB-132	2013/11/19	RPMI1640 (Wako, 189-02145)	10%	1 mM Sodium Pyruvate (Thermo Fisher, 11360-070)	24 hr

MG-63	bone	osteosarcoma	ATCC	CRL-1427	2014/3/26	E-MEM (Wako, 051-07615)	10%	1 mM Sodium Pyruvate (Thermo Fisher, 11360-070) 1x NEAA (Thermo Fisher, 11140-050)	24 hr
MIA-PaCa-2	pancreas	carcinoma	ATCC	CRL-1420	2013/11/21	D-MEM (Wako, 043-30085)	10%		24 hr
MM.1R	B lymphocyte	multiple myeloma	ATCC	CRL-2975	2012/7/25	RPMI1640 (Wako, 189-02145)	10%		immediately
MM.1S	B lymphocyte	multiple myeloma	ATCC	CRL-2974	2012/7/18	RPMI1640 (Wako, 189-02145)	10%		immediately
MOLM-16	blood	acute myeloid leukemia	DSMZ	ACC 555	2014/2/13	RPMI1640 (Wako, 189-02145)	20%		24 hr
MSTO-211H	lung	biphasic mesothelioma	ATCC	CRL-2081	2014/4/23	RPMI1640 (Wako, 189-02145)	10%	1 mM Sodium Pyruvate (Thermo Fisher, 11360-070)	24 hr
NCI-H1755	lung	adenocarcinoma	ATCC	CRL-5892	2015/2/19	RPMI1640 (Wako, 189-02145)	10%		24 hr
NCI-H2228	lung	adenocarcinoma	ATCC	CRL-5935	2013/2/13	RPMI1640 (Wako, 189-02145)	10%	1 mM Sodium Pyruvate (Thermo Fisher, 11360-070)	24 hr

NCI-H226	lung	squamous cell carcinoma; mesothelioma	ATCC	CRL-5826	2012/9/25	RPMI1640 (Wako, 189-02145)	10%		24 hr
NCI-H23	lung	adenocarcinoma; non-small cell lung cancer	ATCC	CRL-5800	2012/6/5	RPMI1640 (Wako, 189-02145)	10%	1 mM Sodium Pyruvate (Thermo Fisher, 11360-070)	24 hr
NCI-H2452	lung	mesothelioma	ATCC	CRL-5946	2014/1/7	RPMI1640 (Wako, 189-02145)	10%	1 mM Sodium Pyruvate (Thermo Fisher, 11360-070)	24 hr
NCI-H28	lung	stage4, mesothelioma	ATCC	CRL-5820	2014/1/7	RPMI1640 (Wako, 189-02145)	10%	1 mM Sodium Pyruvate (Thermo Fisher, 11360-070)	24 hr
NCI-H460	lung	carcinoma; large cell lung cancer	ATCC	HTB-177	2003/7/7	RPMI1640 (Wako, 189-02145)	10%	1 mM Sodium Pyruvate (Thermo Fisher, 11360-070)	24 hr
NCI-H520	lung	squamous cell carcinoma	ATCC	HTB-182	2015/2/19	RPMI1640 (Wako, 189-02145)	10%		24 hr
NCI-H522	lung	adenocarcinoma; non-small cell lung cancer	ATCC	CRL-5810	2012/6/5	RPMI1640 (Wako, 189-02145)	10%	1 mM Sodium Pyruvate (Thermo Fisher, 11360-070)	24 hr
NCI-H661	lung	carcinoma; large cell lung cancer	ATCC	HTB-183	2014/2/13	RPMI1640 (Wako, 189-02145)	10%	1 mM Sodium Pyruvate (Thermo Fisher, 11360-070)	24 hr

NCI-H69	lung	carcinoma; small cell lung cancer	ATCC	HTB-119	2012/11/8	RPMI1640 (Wako, 189-02145)	10%		24 hr
NCI-H810	lung	large lung carcinoma	ATCC	CRL-5816	2015/2/19	DMEM/F12 (Thermo Fisher, 10565-018)	5%	0.005 mg/mL Insulin, 0.01 mg/mL Transferrin, 30 nM Sodium selenite, 10 nM Hydrocortisone, 10 nM beta-estradiol	24 hr
NCI-H929	B lymphocytes	multiple myeloma	ATCC	CRL-9068	2012/7/18	RPMI1640 (Wako, 189-02145)	10%	0.05 mM 3-mercapto-1,2-propanediol (Wako, 139-16452)	immediately
OCI-Ly19	blood	GCB-DLBC lymphoma	NCI, Louis Staudt Lab	-	2013/6/18	IMDM (Thermo Fisher, 12440-053)	20%		24 hr
OVCAR-4	ovary	adenocarcinoma	NCI	NA	2010/3/1	RPMI1640 (Wako, 189-02145)	10%	1 mM Sodium Pyruvate (Thermo Fisher, 11360-070)	24 hr
PA-TU-8902	pancreas	adenocarcinoma	Creative bioarray	CRD-CSC-C0312	2013/11/28	D-MEM (Wako, 043-30085)	10%		24 hr
PL-21	white blood	Immature cells with azuophilic granule	JCRB	JCRB1319	2014/1/16	RPMI1640 (Wako, 189-02145)	20%		24 hr
RKO	colon	carcinoma	ATCC	CRL-2577	2014/10/2	E-MEM (Wako, 051-07615)	10%	1 mM Sodium Pyruvate (Thermo Fisher, 11360-070) 1x NEAA (Thermo Fisher, 11140-050)	24 hr

RPMI8226	blood	multiple myeloma	JCRB	JCRB0034	2014/11/27	RPMI1640 (Wako, 189-02145)	10%		immediately
SF268	central nervous system	highly anaplastic astrocytoma	NCI	0507456	2010/3/1	RPMI1640 (Wako, 189-02145)	10%	1 mM Sodium Pyruvate (Thermo Fisher, 11360-070)	24 hr
SK-MEL-2	skin	malignant melanoma	ATCC	HTB-68	2014/9/12	E-MEM (Wako, 051-07615)	10%	1 mM Sodium Pyruvate (Thermo Fisher, 11360-070) 1x NEAA (Thermo Fisher, 11140-050)	24 hr
SK-MEL-24	skin	malignant melanoma	ATCC	HTB-71	2013/7/25	E-MEM (Wako, 051-07615)	15%	1 mM Sodium Pyruvate (Thermo Fisher, 11360-070) 1x NEAA (Thermo Fisher, 11140-050)	24 hr
SK-MEL-28	skin	malignant melanoma	ATCC	HTB-72	2014/3/12	E-MEM (Wako, 051-07615)	10%	1 mM Sodium Pyruvate (Thermo Fisher, 11360-070) 1x NEAA (Thermo Fisher, 11140-050)	24 hr
SK-MEL-5	skin	malignant melanoma	ATCC	HTB-70	2002/7/?	F12/DMEM(1:1) (Thermo Fisher, 11330-032)	10%		24 hr
SKNO-1	bone marrow	myeloblastic leukemia	JCRB	JCRB1170	2014/12/25	RPMI1640 (Wako, 189-02145)	20%	10 ng/mL GM-CSF	24 hr

SKOV-3	ovary	adenocarcinoma, derived from metastatic site: ascites	ATCC	HTB-77	2009/1/14	McCoy's 5A (Wako, 16600-082)	10%		24 hr
SW1271	lung	carcinoma; small cell lung cancer	ATCC	CRL-2177	2014/9/25	L-15 (Thermo Fisher, 11415-064)	10%	7.5 w/v% Sodium Bicarbonate Solution（wako, 195-16411)	24 hr
SW1417	colon	Dukes' type C, grade III, colorectal adenocarcinoma	ATCC	CCL-238	2014/3/20	L-15 (Thermo Fisher, 11415-064)	10%	7.5 w/v% Sodium Bicarbonate Solution（wako, 195-16411)	24 hr
SW48	colon	adenocarcinoma	Horizon Discovery	HD PAR-006	2011/3/2	L-15 (Thermo Fisher, 11415-064)	10%	7.5 w/v% Sodium Bicarbonate Solution（wako, 195-16411)	24 hr
SW620	colon	Dukes' type C, colorectal adenocarcinoma	ATCC	CCL-227	2002/10/13	L-15 (Thermo Fisher, 11415-064)	10%	7.5 w/v% Sodium Bicarbonate Solution（wako, 195-16411)	24 hr
SW780	urinary bladder	transitional cell carcinoma	ATCC	CRL-2169	2013/4/2	L-15 (Thermo Fisher, 11415-064)	10%	7.5 w/v% Sodium Bicarbonate Solution（wako, 195-16411)	24 hr
SW948	colon	Dukes' type C, grade III, colorectal adenocarcinoma	ATCC	CCL-237	2014/2/25	L-15 (Thermo Fisher, 11415-064)	10%	7.5 w/v% Sodium Bicarbonate Solution（wako, 195-16411)	24 hr

T-24	urinary bladder	transitional cell carcinoma	ATCC	HTB-4	2013/5/23	McCoy's 5A (Wako, 16600-082)	10%		24 hr
T47D	mammary gland/breast	ductal carcinoma	ATCC	HTB-133	2001/4/10	RPMI1640 (Wako, 189-02145)	10%	1 mM Sodium Pyruvate (Thermo Fisher, 11360-070) 10 µg/ml insulin human recombinant (Thermo Fisher, 12585-014)	24 hr
T84	colon	colorectal carcinoma	ATCC	CCL-248	2013/8/20	F12/DMEM(1:1) (Thermo Fisher, 11330-032)	5%		24 hr
TF-1a	bone marrow	erythroleukemia	ATCC	CRL-2451	2014/1/22	RPMI1640 (Wako, 189-02145)	10%		24 hr
THP-1	blood	peripheral blood; monocyte; acute monocytic lukemia	ATCC	TIB-202	2010/1/13	RPMI1640 (Wako, 189-02145)	10%		24 hr
U266B1	B lymphocyte	multiple myeloma	ATCC	TIB-196	2012/7/18	RPMI1640 (Wako, 189-02145)	15%		immediately
U2OS	bone	osteosarcoma	ATCC	HTB-96	2013/6/18	McCoy's 5A (Wako, 16600-082)	10%		24 hr

Table 10. Crystallography data and refinement statistics

	CARM1 + TP-064
PDB Code	5U4X
Data collection	
Space group	$P2_12_12$
Cell dimensions	
a, *b*, *c* (Å)	75.09, 98.92, 207.55
(°)	90.00, 90.00, 90.00
Resolution (Å) (highest resolution shell)	50.00–1.88 (1.91–1.88)
Unique reflections	126636
$R_{merge(\%)}$	8.9 (102.1)
I/I	22.5
Completeness (%)	99.9 (100.0)
Redundancy	7.7 (7.3)
Refinement	
Resolution (Å)	50.00–1.88
No. reflections (test set)	123618 (2521)
R_{work}/R_{free} (%)	21.5/18.8
No. atoms	
Protein	10792
Cofactor	104
Compound	136
Water	700
B-factors (Å^2)	
Protein	28.9
Cofactor	22.6
Compound	25.6
Water	34.4
RMSD	
Bond lengths (Å)	0.009
Bond angles (°)	1.387
Ramachandran plot % residues	
Favored	96.9
Additional allowed	2.8
Generously allowed	0
Disallowed	0.3

Table 11. Binding free energy (DG) for TP-064 complexes calculated with the GBSA method*

Complex	G_{GBSA} (kcal/mol)
PRMT4 + TP-064	−64.6
PRMT3 (1F3L) + TP-064	−54.2
PRMT6 (5E8R) + TP-064	−55

*The protocol for the molecular dynamics simulations in this study are the same as that used in our previous study (DOI: 10.1021/acs.jmedchem.6b00668).

GBSA, generalized Born surface area; PRMT3/4/6, protein arginine methyltransferase 3/4/6; TP-064, N-methyl-N-((2-(1-(2-(methylamino)ethyl)piperidin-4-yl)pyridin-4-yl)methyl)-3-phenoxybenzamide.

General discussion

Epigenetic dysregulations are hypothesized as important oncogenic mechanisms in cancer cells and therefore thought to be promising target for anti-cancer drug. In this study, I focused attention on two epigenetic regulator proteins, LSD1 and PRMT4 as anti-cancer drug targets. First, a synergistic interaction between the LSD1 inhibitor T-3775440 and the NAE inhibitor pevonedistat was evaluated in AML models (part 1). Second, a potent, selective and cell-active PRMT4 inhibitor, TP-064 was developed and its anti-tumor activity was evaluated in various types of cancer cell lines (part 2).

In part 1, I demonstrated a synergistic interaction between the LSD1 inhibitor T-3775440 and the NAE inhibitor pevonedistat in specific types of AML models. Mechanistically, cotreatment with these two agents induced cell transdifferentiation of erythroid leukemia cells cooperatively, as indicated in transcriptomic analysis (Figure 11a and b). I found that GATA1 was downregulated and c-JUN was upregulated by T-3775440- and pevonedistat-treatment (Figure 11c). As GATA1 and c-JUN are known as the master regulator of megakaryocytic–erythroid lineage and granulocytic–monocytic lineage, respectively [50, 51, 52, 54, 55], the key mechanism underlying the synergistic transdifferentiation induced by the T-3775440/peconedistat combination is suggested to be executed by these lineage-restricted transcription factors. It has previously been reported that T-3775440 treatment upregulated CD86, a granulocyte/macrophage marker in TF-1a cells, and cells that expressed higher levels of CD86 exhibited more severely impaired proliferation than cells with lower levels of CD86, suggesting a close linkage between transdifferentiation and T-3775440–mediated growth inhibition [22]. Furthermore, knockdown of PU.1, which is the critical transcription factor for myeloid differentiation, reversed not only T-377540–dependent transdifferentiation but also cell growth suppression and apoptosis [22]. These observations further indicate that the transdifferentiation plays a critical role in T-3775440/pevonedistat combination–mediated cell growth inhibition/apoptosis.

Consistent with previous studies [33, 44], pevonedistat induced DNA rereplication by stabilizing CDT1 in the S phase, leading to DNA damage and apoptosis (Figure 8a). I found that this DNA rereplication-induced DNA damage and cell death were significantly augmented by T-3775440 (Figure 8a and b), suggesting that AML cells under rereplication stress are highly susceptible to T-

3775440 treatment. It was reported that LSD1 was recruited to sites of DNA damage, preferentially in late S/G2 phase, and promoted ubiquitylation of histone H2A/H2AX, thus enabling a full DNA damage response [56]. Recently, Hahm et al. [97] reported that LSD1 mediated demethylation of ubiquitin-like with PHD and RING finger domains 1 (UHRF1), a key epigenetic regulator of DNA methylation maintenance and heterochromatin formation [98, 99, 100]. It has also been reported that UHRF1 has an important role in DNA damage response [101, 102, 103]. UHRF1 is methylated by SET7 and demethylated by LSD1, and UHRF1 methylation catalyzes the conjugation of polyubiquitin chains to PCNA and promotes homologous recombination for DNA repair [97]. These observations suggest that LSD1 inhibition by T-3775440 sensitizes cells to pevonedistat-induced DNA damage by disabling the DNA repair machinery, although the exact mechanisms have yet to be clarified.

I investigated the combination effects of T-3775440 with cytarabine, daunorubicine and azacitidine, which are used for the treatment of AML and/or MDS, in addition to pevonedistat, in a round-robin manner. The result indicated that the best combination partner for T-3775440 was pevonedistat, and vice versa (Figure 3c and Figure 5). Regarding the combination with pevonedistat, cytarabine and azacitidine showed clear synergism, albeit the synergistic interaction with T-3775440/pevonedistat was stronger than them. Cytarabine is the nucleoside analog class of anti-cancer drug that is incorporated into elongating DNA strands in the S phase and generate DNA double strand breaks [104]. Nawrocki et al. reported the synergistic interaction of cytarabine and pevonedistat in AML cells [105]. Mechanistically, pevonedistat disrupted nucleotide metabolism and depleted intracellular nucleotide pools in cells, resulted in increased incorporation of cytarabine into the DNA and increased DNA damage. This suggests that the mechanisms of combination synergy of cytarabine/pevonedistat is dependent on pevonedistat-mediated cell sensitization to cytarabine-induced DNA damage. As I mentioned before, T-3775440 can sensitize cells to pevonedistat-induced anti-tumor effect via two distinct mechanisms, DNA damage response and transdifferentiation. It is possible that the synergistic interaction in transdifferentiation is one of the reasons why T-3775440/pevonedistat combination is superior to cytarabine/pevonedistat combination. Azacitidine is

the nucleoside analog class of anti-cancer drug which was developed as inhibitor of DNA methylation [106, 107, 108]. Azacitidine is thought to be incorporated into cellular DNA and/or RNA and exert anti-tumor efficacy via two major mechanisms, (a) demethylation of DNA by inhibiting DNA methyltransferases and reactivation of silenced genes; and (b) induction of DNA damage due to the formation of DNA adducts [109]. Further studies are needed how DNA methyltransferase inhibitor activity of azacitidine impact on the combination efficacy with pevonedistat, in addition to DNA damaging activity like cytarabine. On the other hand, antagonistic interaction was shown in the daunorubicine/pevonedistat combination, in consistent with previous report [110]. Daunorubicin is an anthracycline antibiotic which is intercalated into DNA strands and generate DNA double strand breaks [111]. Al-Aamri et al. reported that daunorubicine induced G2/M or G1 cell cycle arrest in acute lymphoid leukemia cell lines [112]. As pevonedistat act as rereplication inducer in S phase, it is suggested that the non-S phase arrest induced by daunorubicine cause antagonistic interaction in the combination. Of note, I demonstrated that the combination of T-3775440 with pevonedistat was the best of all other combinations. These data suggest that a T-3775440/pevonedistat combination regimen represents a novel strategy to treat resistant/refractory AML, beyond conventional induction chemotherapy.

In part 2, I described the development of a potent, selective and cell-active PRMT4 inhibitor, TP-064. To my knowledge, this is the most potent and selective PRMT4 inhibitor in *in vitro* assay and thus TP-064 can serve as a useful tool for studying the physiological and pathological functions of PRMT4. Recently, Drew et al. reported the cell-potent, orally bioavailable, and selective PRMT4 inhibitor, EZM2302 and its anti-tumor efficacy in *in vitro*/*vivo* MM model [77]. In future, evaluation of TP-064 in *in vivo* assay, such as pharmacokinetics, *in vivo* target engagement and efficacy study, and comparison study to EPZ2302 will be needed for further investigation of the pathological role of PRMT4 in MM.

The cancer cell panel screening and subsequent MM-focused cell panel growth inhibition study revealed that TP-064 inhibited the proliferation of a subset of MM cell lines (Figure 24A and B).

Previously reported *in vitro* experiments using genetic knockdown of PRMT4 have shown anti-proliferative effect of knockdown in several cancer cell lines. These results have suggested a potential role for PRMT4 in modulating WNT-induced expression of β-catenin genes in colorectal cancer [63], coactivating transcriptional activity of the androgen receptor in prostate cancer [66] and regulating estrogen-mediated transcriptional activation in breast cancer [67]. Interestingly, treatment of colorectal and breast cancer cell lines with the PRMT4 inhibitor TP-064 had no anti-proliferative effect (Figure 24A and Figure 25), suggesting that a potential non-catalytic activity of PRMT4, such as a protein scaffolding function, is involved in the proliferation in these cancer cell types. In fact, expression of a catalytically inactive PRMT4 mutant reduces but does not eliminate transcriptional coactivation, suggesting that non-catalytic mechanisms also exist [113, 114]. In this study, I showed that TP-064 bound to the substrate binding pocket of PRMT4 (Figure 23A), though its IC_{50} value was not affected by substrate peptide concentration (Figure 20B), suggesting a non-competitive mode of inhibition. These results suggest that the binding affinity of the peptide substrate is derived from regions outside of the arginine-binding pocket. Therefore, it is predicted that TP-064 could not inhibit the non-catalytic function of PRMT4, because TP-064 did not affect the protein-protein interaction of PRMT4 and its substrate proteins. Further studies with inhibitors of PRMT4 methyltransferase activity such as TP-064 will enable a more detailed study to segregate these catalytic and non-catalytic mechanisms of action to oncogenesis.

In this study, I demonstrated anti-proliferative effects of PRMT4 inhibition by TP-064 treatment in a subset of MM cell lines, although the underlying mechanisms of action is yet to be elucidated. I showed that TP-064 treatment reduced the proportion of NCI-H929 cells in S and G2/M phases while increasing the G1 phase fraction (Figure 28B), suggesting that PRMT4 inhibition by TP-064 induced G1 cell cycle arrest. It has been reported that PRMT4 positively regulates the expression of Cyclin E1 and E2, well-known G1/S checkpoint molecules, by methylating arginines 17 and 26 of histone H3 in the promoter region of these genes [63, 115]. These evidences suggest that anti-proliferative activity of TP-064 is, at least in part, dependent on the TP-064 treatment-induced G1 cell

cycle arrest, which is mediated by inhibition of CCNE1/2 transcription. In addition, though PRMT4 is demonstrated to be involved in cell proliferation in a subset of MM cells, PRMT4 mRNA expression itself is not correlated to the sensitivity to TP-064 treatment (Figure 24C). This suggests that TP-064 exert its anti-proliferative effect in cells with specific context other than PRMT4 expression. Further mechanistic analysis should be needed for understanding of the mode of action of PRMT4 in MM cell proliferation. Given that PRMT4 is known to be involved in multiple biological functions and has a wide range of substrates, comprehensive analyses such as the transcriptome, proteome, and methylome and chromatin immunoprecipitation sequencing in TP-064-treated cells can provide insight into the regulation of PRMT4-mediated growth and survival in MM cells as well as biomarkers for evaluating the efficacy of PRMT4 inhibitors.

In conclusion, the findings described in part 1 demonstrate that a synergistic interaction between the LSD1 inhibitor T-3775440 and the NAE inhibitor pevonedistat yielded significant anti-AML effects including complete remission in preclinical erythroid leukemia models. As described in part 2, a potent, selective and cell-active PRMT4 inhibitor, TP-064 was developed. Treatment with TP-064 resulted in anti-proliferative activity in MM cell lines. TP-064 is a tool compound that can be used to further explore the biological/pathological role of PRMT4 in multiple myeloma and other oncology indications. These findings indicate that the LSD1/NAE inhibitor combination strategy and PRMT4 inhibition are worth consideration for the treatment of AML and MM, respectively.

Acknowledgements

I am most grateful to Professor Kentaro Nakano (University of Tsukuba) for being in charge of this dissertation, and for his valuable guidance and encouragement.

Also, I am sincerely grateful to Professor Tomoki Chiba and Associate Professors Hidekazu Kuwayama and Ryuhei Harada (University of Tsukuba) for their appropriate advice during the preparation of this dissertation.

I also thank Dr. Kazuhide Nakamura (Takeda Pharmaceutical Company Limited) and Dr. Peter J. Brown (University of Toronto) for their encouragement and helpful guidance in my research work.

Acknowledgements are also made to Dr. Yoshinori Ishikawa, Dr. Daisuke Tomita, Dr. Atsushi Kiba (Takeda Pharmaceutical Company Limited), Dr. Magdalena M. Szewczyk and Dr. Carlo dela Sena (University of Toronto) for their kind cooperation and advice in my research work.

Further, I thank Dr. Akira Hayashi and Dr. Yoshiaki Kassai, current supervisors in Takeda Pharmaceutical Company Limited, for endorsement of participation in the graduate program.

Finally, I would like to thank my colleagues at Oncology Drug Discovery Unit and T-CiRA research in Takeda Pharmaceutical Company Limited, and at Structural Genomics Consortium in University of Toronto, for their encouragement during the preparation of this dissertation.

References

1. Park JW, Han JW. Targeting epigenetics for cancer therapy. Arch Pharm Res. 2019; 42: 159-170.
2. Moore LD, Le T, Fan G. DNA methylation and its basic function. Neuropsychopharmacology. 2013; 38: 23-38.
3. Prachayasittikul V, Prathipati P, Pratiwi R, Phanus-Umporn C, Malik AA, Schaduangrat N, Seenprachawong K, Wongchitrat P, Supokawej A, Prachayasittikul V, Wikberg JE, Nantasenamat C. Exploring the epigenetic drug discovery landscape. Expert Opin Drug Discov. 2017; 12: 345-362.
4. Audia JE, Campbell RM. Histone modifications and cancer. Cold Spring Harb Perspect Biol. 2016; 8: a019521.
5. WHO Cancer profile 2020, https://www.paho.org/hq/index.php?option=com_docman&view=download&category_slug=4-cancer-country-profiles-2020&alias=51561-global-cancer-profile-2020&Itemid=270&lang=fr
6. Vogelstein B, Papadopoulos N, Velculescu VE, Zhou S, Diaz LA Jr, Kinzler KW. Cancer genome landscapes. Science. 2013; 339: 1546-58.
7. Kandoth C, McLellan MD, Vandin F, Ye K, Niu B, Lu C, Xie M, Zhang Q, McMichael JF, Wyczalkowski MA, Leiserson MDM, Miller CA, Welch JS, Walter MJ, Wendl MC, Ley TJ, Wilson RK, Raphael BJ, Ding L. Mutational landscape and significance across 12 major cancer types. Nature. 2013; 502: 333-339.
8. Shen H, Laird PW. Interplay between the cancer genome and epigenome. Cell. 2013; 153: 38-55.
9. Esteller M. Epigenetics in cancer. N Engl J Med. 2008; 358: 1148-59.
10. Flavahan WA, Gaskell E, Bernstein BE. Epigenetic plasticity and the hallmarks of cancer. Science. 2017; 357: eaal2380.
11. Ganesan A, Arimondo PB, Rots MG, Jeronimo C, Berdasco M. The timeline of epigenetic drug discovery: from reality to dreams. Clin Epigenetics. 2019; 11: 174.
12. American Cancer Society Cancer Facts & Figures 2016, https://www.cancer.org/research/cancer-facts-statistics/all-cancer-facts-figures/cancer-facts-figures-2016.html.

13. Shi Y, Lan F, Matson C, Mulligan P, Whetstine JR, Cole PA et al. Histone demethylation mediated by the nuclear amine oxidase homolog LSD1. Cell 2004; 119: 941–953.
14. Metzger E, Wissmann M, Yin N, Muller JM, Schneider R, Peters AH et al. LSD1 demethylates repressive histone marks to promote androgen-receptor-dependent transcription. Nature 2005; 437: 436–439.
15. Lee MG, Wynder C, Cooch N, Shiekhattar R. An essential role for CoREST in nucleosomal histone 3 lysine 4 demethylation. Nature 2005; 437: 432–435.
16. Saleque S, Kim J, Rooke HM, Orkin SH. Epigenetic regulation of hematopoietic differentiation by Gfi-1 and Gfi-1b is mediated by the cofactors CoREST and LSD1. Mol Cell 2007; 27: 562–572.
17. Niebel D, Kirfel J, Janzen V, Holler T, Majores M, Gutgemann I. Lysine-specific demethylase 1 (LSD1) in hematopoietic and lymphoid neoplasms. Blood 2014; 124: 151–152.
18. Lynch JT, Harris WJ, Somervaille TC. LSD1 inhibition: a therapeutic strategy in cancer? Expert Opin Ther Targets 2012; 16: 1239–1249.
19. Harris WJ, Huang X, Lynch JT, Spencer GJ, Hitchin JR, Li Y et al. The histone demethylase KDM1A sustains the oncogenic potential of MLL-AF9 leukemia stem cells. Cancer Cell 2012; 21: 473–487.
20. Mohammad HP, Smitheman KN, Kamat CD, Soong D, Federowicz KE, Van Aller GS et al. A DNA hypomethylation signature predicts antitumor activity of LSD1 inhibitors in SCLC. Cancer Cell 2015; 28: 57–69.
21. McGrath JP, Williamson KE, Balasubramanian S, Odate S, Arora S, Hatton C et al. Pharmacological inhibition of the histone lysine demethylase KDM1A suppresses the growth of multiple acute myeloid leukemia subtypes. Cancer Res 2016; 76: 1975–1988.
22. Ishikawa Y, Gamo K, Yabuki M, Takagi S, Toyoshima K, Nakayama K et al. A novel LSD1 inhibitor T-3775440 disrupts GFI1B-containing complex leading to transdifferentiation and impaired growth of AML cells. Mol Cancer Ther 2017; 16: 273–284.

23. Schenk T, Chen WC, Gollner S, Howell L, Jin L, Hebestreit K et al. Inhibition of the LSD1 (KDM1A) demethylase reactivates the all-trans-retinoic acid differentiation pathway in acute myeloid leukemia. Nat Med 2012; 18: 605–611.
24. Fiskus W, Sharma S, Shah B, Portier BP, Devaraj SG, Liu K et al. Highly effective combination of LSD1 (KDM1A) antagonist and pan-histone deacetylase inhibitor against human AML cells. Leukemia 2014; 28: 2155–2164.
25. Soucy TA, Smith PG, Milhollen MA, Berger AJ, Gavin JM, Adhikari S et al. An inhibitor of NEDD8-activating enzyme as a new approach to treat cancer. Nature 2009; 458: 732–776.
26. Nawrocki ST, Griffin P, Kelly KR, Carew JS. MLN4924: a novel first-in-class inhibitor of NEDD8-activating enzyme for cancer therapy. Expert Opin Investig Drugs 2012; 21: 1563–1573.
27. Nakayama KI, Nakayama K. Ubiquitin ligases: cell-cycle control and cancer. Nat Rev Cancer 2006; 6: 369–381.
28. Skaar JR, Pagan JK, Pagano M. SCF ubiquitin ligase-targeted therapies. Nat Rev Drug Discov 2014; 13: 889–903.
29. Swords RT, Kelly KR, Smith PG, Garnsey JJ, Mahalingam D, Medina E et al. Inhibition of NEDD8-activating enzyme: a novel approach for the treatment of acute myeloid leukemia. Blood 2010; 115: 3796–3800.
30. Swords RT, Erba HP, DeAngelo DJ, Bixby DL, Altman JK, Maris M et al. Pevonedistat (MLN4924), a first-in-class NEDD8-activating enzyme inhibitor, in patients with acute myeloid leukaemia and myelodysplastic syndromes: a phase 1 study. Br J Haematol 2015; 169: 534–543.
31. Kee Y, Huang M, Chang S, Moreau LA, Park E, Smith PG et al. Inhibition of the Nedd8 system sensitizes cells to DNA interstrand cross-linking agents. Mol Cancer Res 2012; 10: 369–377.
32. Blank JL, Liu XJ, Cosmopoulos K, Bouck DC, Garcia K, Bernard H et al. Novel DNA damage checkpoints mediating cell death induced by the NEDD8-activating enzyme inhibitor MLN4924. Cancer Res 2013; 73: 225–234.

33. Milhollen MA, Narayanan U, Soucy TA, Veiby PO, Smith PG, Amidon B. Inhibition of NEDD8-activating enzyme induces rereplication and apoptosis in human tumor cells consistent with deregulating CDT1 turnover. Cancer Res 2011; 71: 3042–3051.
34. Khalife J, Radomska HS, Santhanam R, Huang X, Neviani P, Saultz J et al. Pharmacological targeting of miR-155 via the NEDD8-activating enzyme inhibitor MLN4924 (Pevonedistat) in FLT3-ITD acute myeloid leukemia. Leukemia 2015; 29: 1981–1992.
35. Garcia K, Blank JL, Bouck DC, Liu XJ, Sappal DS, Hather G et al. Nedd8-activating enzyme inhibitor MLN4924 provides synergy with mitomycin C through interactions with ATR, BRCA1/BRCA2, and chromatin dynamics pathways. Mol Cancer Ther 2014; 13: 1625–1635.
36. Minto CF, Schnider TW, Short TG, Gregg KM, Gentilini A, Shafer SL. Response surface model for anesthetic drug interactions. Anesthesiology 2000; 92: 1603–1616.
37. Chou TC, Talalay P. Quantitative analysis of dose-effect relationships: the combined effects of multiple drugs or enzyme inhibitors. Adv Enzyme Regul 1984; 22: 27–55.
38. Berenbaum MC. The expected effect of a combination of agents: the general solution. J Theor Biol 1985; 114: 413–431.
39. Peterson JJ, Novick SJ. Nonlinear blending: a useful general concept for the assessment of combination drug synergy. J Recept Signal Transduct Res 2007; 27: 125–146.
40. Subramanian A, Tamayo P, Mootha VK, Mukherjee S, Ebert BL, Gillette MA et al. Gene set enrichment analysis: a knowledge-based approach for interpreting genome-wide expression profiles. Proc Natl Acad Sci USA 2005; 102: 15545–15550.
41. Novershtern N, Subramanian A, Lawton LN, Mak RH, Haining WN, McConkey ME et al. Densely interconnected transcriptional circuits control cell states in human hematopoiesis. Cell 2011; 144: 296–309.
42. Saleque S, Cameron S, Orkin SH. The zinc-finger proto-oncogene Gfi-1b is essential for development of the erythroid and megakaryocytic lineages. Genes Dev 2002; 16: 301–306.

43. Vassen L, Fiolka K, Mahlmann S, Moroy T. Direct transcriptional repression of the genes encoding the zinc-finger proteins Gfi1b and Gfi1 by Gfi1b. Nucleic Acids Res 2005; 33: 987–998.
44. Lin JJ, Milhollen MA, Smith PG, Narayanan U, Dutta A. NEDD8-targeting drug MLN4924 elicits DNA rereplication by stabilizing Cdt1 in S phase, triggering checkpoint activation, apoptosis, and senescence in cancer cells. Cancer Res 2010; 70: 10310–10320.
45. Tenen DG. Disruption of differentiation in human cancer: AML shows the way. Nat Rev Cancer 2003; 3: 89–101.
46. Liao H, Liu XJ, Blank JL, Bouck DC, Bernard H, Garcia K et al. Quantitative proteomic analysis of cellular protein modulation upon inhibition of the NEDD8-activating enzyme by MLN4924. Mol Cell Proteomics 2011; 10: M111.009183.
47. Nateri AS, Riera-Sans L, Da Costa C, Behrens A. The ubiquitin ligase SCFFbw7 antagonizes apoptotic JNK signaling. Science (New York, NY) 2004; 303: 1374–1378.
48. Sarantopoulos J, Shapiro GI, Cohen RB, Clark JW, Kauh JS, Weiss GJ et al. Phase I study of the investigational NEDD8-activating enzyme inhibitor pevonedistat (TAK-924/MLN4924) in patients with advanced solid tumors. Clin Cancer Res 2016; 22: 847–857.
49. Shimizu R, Engel JD, Yamamoto M. GATA1-related leukaemias. Nat Rev Cancer 2008; 8: 279–287.
50. Zhang P, Behre G, Pan J, Iwama A, Wara-Aswapati N, Radomska HS et al. Negative cross-talk between hematopoietic regulators: GATA proteins repress PU.1. Proc Natl Acad Sci USA 1999; 96: 8705–8710.
51. Rekhtman N, Radparvar F, Evans T, Skoultchi AI. Direct interaction of hematopoietic transcription factors PU.1 and GATA-1: functional antagonism in erythroid cells. Genes Dev 1999; 13: 1398–1411.
52. Burda P, Laslo P, Stopka T. The role of PU.1 and GATA-1 transcription factors during normal and leukemogenic hematopoiesis. Leukemia 2010; 24: 1249–1257.

53. Tan M, Li Y, Yang R, Xi N, Sun Y. Inactivation of SAG E3 ubiquitin ligase blocks embryonic stem cell differentiation and sensitizes leukemia cells to retinoid acid. PLoS ONE 2011; 6: e27726.
54. Behre G, Whitmarsh AJ, Coghlan MP, Hoang T, Carpenter CL, Zhang DE et al. c-Jun is a JNK-independent coactivator of the PU.1 transcription factor. J Biol Chem 1999; 274: 4939–4946.
55. Burda P, Curik N, Kokavec J, Basova P, Mikulenkova D, Skoultchi AI et al. PU.1 activation relieves GATA-1-mediated repression of Cebpa and Cbfb during leukemia differentiation. Mol Cancer Res 2009; 7: 1693–1703.
56. Mosammaparast N, Kim H, Laurent B, Zhao Y, Lim HJ, Majid MC et al. The histone demethylase LSD1/KDM1A promotes the DNA damage response. J Cell Biol 2013; 203: 457–470.
57. Zhou L, Chen S, Zhang Y, Kmieciak M, Leng Y, Li L et al. The NAE inhibitor pevonedistat interacts with the HDAC inhibitor belinostat to target AML cells by disrupting the DDR. Blood 2016; 127: 2219–2230.
58. Fuhrmann J, Clancy KW, Thompson PR. Chemical biology of protein arginine modifications in epigenetic regulation. Chem Rev. 2015; 115: 5413–5461.
59. Bedford MT, Richard S. Arginine methylation an emerging regulator of protein function. Mol Cell. 2005; 18: 263–272.
60. Schurter BT, Koh SS, Chen D, Bunick GJ, Harp JM, Hanson BL, Henschen-Edman A, Mackay DR, Stallcup MR, Aswad DW. Methylation of histone H3 by coactivator-associated arginine methyltransferase 1. Biochemistry. 2001; 40: 5747–5756.
61. An W, Kim J, Roeder RG. Ordered cooperative functions of PRMT1, p300, and CARM1 in transcriptional activation by p53. Cell. 2004; 117: 735–748.
62. Cheng D, Cote J, Shaaban S, Bedford MT. The arginine methyltransferase CARM1 regulates the coupling of transcription and mRNA processing. Mol Cell. 2007; 25: 71–83.
63. El Messaoudi S, Fabbrizio E, Rodriguez C, Chuchana P, Fauquier L, Cheng D, Theillet C, Vandel L, Bedford MT, Sardet C. Coactivator-associated arginine methyltransferase 1 (CARM1) is a positive regulator of the Cyclin E1 gene. Proc Natl Acad Sci U S A. 2006; 103: 13351–13356.

64. Lee YH, Stallcup MR. Roles of protein arginine methylation in DNA damage signaling pathways is CARM1 a life-or-death decision point? Cell Cycle. 2011; 10: 1343–1344.

65. Chen SL, Loffler KA, Chen D, Stallcup MR, Muscat GE. The coactivator-associated arginine methyltransferase is necessary for muscle differentiation: CARM1 coactivates myocyte enhancer factor-2. J Biol Chem. 2002; 277: 4324–4333.

66. Hong H, Kao C, Jeng MH, Eble JN, Koch MO, Gardner TA, Zhang S, Li L, Pan CX, Hu Z, MacLennan GT, Cheng L. Aberrant expression of CARM1, a transcriptional coactivator of androgen receptor, in the development of prostate carcinoma and androgen-independent status. Cancer. 2004; 101: 83–89.

67. Kim YR, Lee BK, Park RY, Nguyen NT, Bae JA, Kwon DD, Jung C. Differential CARM1 expression in prostate and colorectal cancers. BMC Cancer. 2010; 10: 197.

68. Ou CY, LaBonte MJ, Manegold PC, So AY, Ianculescu I, Gerke DS, Yamamoto KR, Ladner RD, Kahn M, Kim JH, Stallcup MR. A coactivator role of CARM1 in the dysregulation of beta-catenin activity in colorectal cancer cell growth and gene expression. Mol Cancer Res. 2011; 9: 660–670.

69. Frietze S, Lupien M, Silver PA, Brown M. CARM1 regulates estrogen-stimulated breast cancer growth through up-regulation of E2F1. Cancer Res. 2008; 68: 301–306.

70. Vu LP, Perna F, Wang L, Voza F, Figueroa ME, Tempst P, Erdjument-Bromage H, Gao R, Chen S, Paietta E, Deblasio T, Melnick A, Liu Y, Zhao X, Nimer SD. PRMT4 blocks myeloid differentiation by assembling a methyl-RUNX1-dependent repressor complex. Cell Rep. 2013; 5: 1625–1638.

71. Wang L, Zhao Z, Meyer MB, Saha S, Yu M, Guo A, Wisinski KB, Huang W, Cai W, Pike JW, Yuan M, Ahlquist P, Xu W. CARM1 methylates chromatin remodeling factor BAF155 to enhance tumor progression and metastasis. Cancer Cell. 2014; 25: 21–36.

72. Hu H, Qian K, Ho MC, Zheng YG. Small molecule inhibitors of protein arginine methyltransferases. Expert Opin Investig Drugs. 2016; 25: 335–358.

73. Sack JS, Thieffine S, Bandiera T, Fasolini M, Duke GJ, Jayaraman L, Kish KF, Klei HE, Purandare AV, Rosettani P, Troiani S, Xie D, Bertrand JA. Structural basis for CARM1 inhibition by indole and pyrazole inhibitors. Biochem J. 2011; 436: 331–339.

74. Ferreira de Freitas R, Eram MS, Smil D, Szewczyk MM, Kennedy S, Brown PJ, Santhakumar V, Barsyte-Lovejoy D, Arrowsmith CH, Vedadi M, Schapira M. Discovery of a potent and selective coactivator associated arginine methyltransferase 1 (CARM1) inhibitor by virtual screening. J Med Chem. 2016; 59: 6838–6847.

75. Eram MS, Shen Y, Szewczyk MM, Wu H, Senisterra G, Li F, Butler KV, Kaniskan HU, Speed BA, dela Sena C, Dong A, Zeng H, Schapira M, et al. A potent, selective, and cell-active inhibitor of human type I protein arginine methyltransferases. ACS Chem Biol. 2016; 11: 772–781.

76. Uhlen M, Fagerberg L, Hallstrom BM, Lindskog C, Oksvold P, Mardinoglu A, Sivertsson A, Kampf C, Sjostedt E, Asplund A, Olsson I, Edlund K, Lundberg E, et al. Proteomics. Tissue-based map of the human proteome. Science. 2015; 347: 1260419.

77. Drew AE, Moradei O, Jacques SL, Rioux N, Boriack-Sjodin AP, Allain C, Scott MP, Jin L, Raimondi A, Handler JL, Ott HM, Kruger RG, McCabe MT, et al. Identification of a CARM1 Inhibitor with Potent *In Vitro* and *In Vivo* Activity in Preclinical Models of Multiple Myeloma. Sci. Rep. 2017 Dec 21;7(1):17993.

78. Ferreira de Freitas R, Eram MS, Szewczyk MM, Steuber H, Smil D, Wu H, Li F, Senisterra G, Dong A, Brown PJ, Hitchcock M, Moosmayer D, Stegmann CM, et al. Discovery of a potent class I protein arginine methyltransferase fragment inhibitor. J Med Chem. 2016; 59: 1176–1183.

79. Smil D, Eram MS, Li F, Kennedy S, Szewczyk MM, Brown PJ, Barsyte-Lovejoy D, Arrowsmith CH, Vedadi M, Schapira M. Discovery of a dual PRMT5-PRMT7 inhibitor. ACS Med Chem Lett. 2015; 6: 408–412.

80. Siarheyeva A, Senisterra G, Allali-Hassani A, Dong A, Dobrovetsky E, Wasney GA, Chau I, Marcellus R, Hajian T, Liu F, Korboukh I, Smil D, Bolshan Y, et al. An allosteric inhibitor of protein arginine methyltransferase 3. Structure. 2012; 20: 1425–1435.

81. Shen Y, Szewczyk MM, Eram MS, Smil D, Kaniskan HU, Ferreira de Freitas R, Senisterra G, Li F, Schapira M, Brown PJ, Arrowsmith CH, Barsyte-Lovejoy D, Liu J, et al. Discovery of a potent, selective, and cell-active dual inhibitor of protein arginine methyltransferase 4 and protein arginine methyltransferase 6. J Med Chem. 2016; 59: 9124–9139.
82. Barsyte-Lovejoy D, Li F, Oudhoff MJ, Tatlock JH, Dong A, Zeng H, Wu H, Freeman SA, Schapira M, Senisterra GA, Kuznetsova E, Marcellus R, Allali-Hassani A, et al. (R)-PFI-2 is a potent and selective inhibitor of SETD7 methyltransferase activity in cells. Proc Natl Acad Sci U S A. 2014; 111: 12853–12858.
83. Kaniskan HU, Szewczyk MM, Yu Z, Eram MS, Yang X, Schmidt K, Luo X, Dai M, He F, Zang I, Lin Y, Kennedy S, Li F, et al. A potent, selective and cell-active allosteric inhibitor of protein arginine methyltransferase 3 (PRMT3). Angew Chem Int Ed Engl. 2015; 54: 5166–5170.
84. Vedadi M, Niesen FH, Allali-Hassani A, Fedorov OY, Finerty PJ, Jr., Wasney GA, Yeung R, Arrowsmith CH, Ball LJ, Berglund H, Hui R, Marsden BD, Nordlund P, et al. Chemical screening methods to identify ligands that promote protein stability, protein crystallization, and structure determination. Proc Natl Acad Sci U S A. 2006; 103: 15835–15840.
85. Otwinowski Z and Minor W. Processing of X-ray diffraction data collected in oscillation mode. Methods Enzymol. 1997; 276: 307–326.
86. Murshudov GN, Vagin AA, Dodson EJ. Refinement of macromolecular structures by the maximum-likelihood method. Acta Crystallogr D Biol Crystallogr. 1997; 53:240–255.
87. Emsley P and Cowtan K. Coot: model-building tools for molecular graphics. Acta Crystallogr D Biol Crystallogr. 2004; 60: 2126–2132.
88. Davis IW, Murray LW, Richardson JS, Richardson DC. MOLPROBITY: structure validation and all-atom contact analysis for nucleic acids and their complexes. Nucleic Acids Res. 2004; 32: 615–619.
89. Zhang X, Zhou L, Cheng X. Crystal structure of the conserved core of protein arginine methyltransferase PRMT3. EMBO J. 2000; 19: 3509–3519.

90. Brown JI, Koopmans T, van Strien J, Martin NI, Frankel A. Kinetic analysis of PRMT1 reveals multifactorial processivity and a sequential ordered mechanism. Chembiochem. 2018; 19: 85-99.
91. Liu L, Zhen XT, Denton E, Marsden BD, Schapira M. ChromoHub: a data hub for navigators of chromatin-mediated signalling. Bioinformatics. 2012; 28: 2205-6.
92. Mitchell LH, Boriack-Sjodin PA, Smith S, Thomenius M, Rioux N, Munchhof M, Mills JE, Klaus C, Totman J, Riera TV, Raimondi A, Jacques SL, West K, et al. Novel oxindole sulfonamides and sulfamides: EPZ031686, the first orally bioavailable small molecule SMYD3 inhibitor. ACS Med Chem Lett. 2015; 7: 134–138.
93. Wang L, Zeng H, Wang Q, Zhao Z, Boyer T, Bian X, Xu W. MED12 methylation by CARM1 sensitizes human breast cancer cells to chemotherapy drugs. Sci Adv. 2015; 1: e1500463.
94. Chen J, Archer TK. Regulating SWI/SNF subunit levels via protein-protein interactions and proteasomal degradation: BAF155 and BAF170 limit expression of BAF57. Mol Cell Biol. 2005; 25: 9016–27.
95. Schrödinger Release 2017-2: Glide, Schrödinger, LLC, New York, NY, 2017.
96. Han K, Jeng EE, Hess GT, Morgens DW, Li A, Bassik MC. Synergistic drug combinations for cancer identified in a CRISPR screen for pairwise genetic interactions. Nat Biotechnol. 2017; 35: 463–474.
97. Hahm JY, Kim JY, Park JW, Kang JY, Kim KB, Kim SR, Cho H, Seo SB. Methylation of UHRF1 by SET7 is essential for DNA double-strand break repair. Nucleic Acids Res. 2019; 47: 184-196.
98. Arita K, Isogai S, Oda T, Unoki M, Sugita K, Sekiyama N, Kuwata K, Hamamoto R, Tochio H, Sato M, Ariyoshi M, Shirakawa M. Recognition of modification status on a histone H3 tail by linked histone reader modules of the epigenetic regulator UHRF1. Proc. Natl. Acad. Sci. U.S.A. 2012; 109:12950–12955.
99. Avvakumov GV, Walker JR, Xue S, Li Y, Duan S, Bronner C, Arrowsmith CH, Dhe-Paganon S. Structural basis for recognition of hemi-methylated DNA by the SRA domain of human UHRF1. Nature. 2008; 455:822–825.

100. Babbio F, Pistore C, Curti L, Castiglioni I, Kunderfranco P, Brino L, Oudet P, Seiler R, Thalman GN, Roggero E, Sarti M, Pinton S, Mello-Grand M, Chiorino G, Catapano CV, Carbone GM, Bonapace IM. The SRA protein UHRF1 promotes epigenetic crosstalks and is involved in prostate cancer progression. Oncogene. 2012; 31:4878–4887.

101. Tien AL, Senbanerjee S, Kulkarni A, Mudbhary R, Goudreau B, Ganesan S, Sadler KC, Ukomadu C. UHRF1 depletion causes a G2/M arrest, activation of DNA damage response and apoptosis. Biochem. J. 2011; 435:175–185.

102. Mistry H, Tamblyn L, Butt H, Sisgoreo D, Gracias A, Larin M, Gopalakrishnan K, Hande MP, McPherson JP. UHRF1 is a genome caretaker that facilitates the DNA damage response to gamma-irradiation. Genome Integr. 2010; 1:7.

103. Tian Y, Paramasivam M, Ghosal G, Chen D, Shen X, Huang Y, Akhter S, Legerski R, Chen J, Seidman MM, Qin J, Li L. UHRF1 contributes to DNA damage repair as a lesion recognition factor and nuclease scaffold. Cell Rep. 2015; 10:1957–1966.

104. Grant S. Ara-C: cellular and molecular pharmacology. Adv Cancer Res. 1998; 72: 197-233.

105. Nawrocki ST, Kelly KR, Smith PG, Keaton M, Carraway H, Sekeres MA, Maciejewski JP, Carew JS. The NEDD8-activating enzyme inhibitor MLN4924 disrupts nucleotide metabolism and augments the efficacy of cytarabine. Clin Cancer Res. 2015; 21: 439-47.

106. Bender CM, Zingg JM, Jones PA. DNA methylation as a target for drug design. Pharm Res 1998; 15: 175–87.

107. Taylor SM, Constantinides PA, Jones PA. 5-Azacytidine, DNA methylation, and differentiation. Curr Top Microbiol Immunol 1984; 108: 115–27.

108. Jones PA, Taylor SM, Wilson VL. Inhibition of DNA methylation by 5-azacytidine. Recent Results Cancer Res 1983; 84: 202–11.

109. Szafraniec SI, Stachnik KJ, Skierski JS. New nucleoside analogs in the treatment of hematological disorders. Acta Pol Pharm 2004; 61: 223–32.

110. Garcia K, Blank JL, Bouck DC, Liu XJ, Sappal DS, Hather G, Cosmopoulos K, Thomas MP, Kuranda M, Pickard MD, Liu R, Bandi S, Smith PG, Lightcap ES. Nedd8-activating enzyme inhibitor MLN4924 provides synergy with mitomycin C through interactions with ATR, BRCA1/BRCA2, and chromatin dynamics pathways. Mol Cancer Ther. 2014; 13: 1625-35.

111. Al-Aamri HM, Ku H, Irving HR, Tucci J, Meehan-Andrews T, Bradley C. Time dependent response of daunorubicin on cytotoxicity, cell cycle and DNA repair in acute lymphoblastic leukaemia. BMC Cancer. 2019; 19: 179.

112. Al-Aamri HM, Ku H, Irving HR, Tucci J, Meehan-Andrews T, Bradley C. Time dependent response of daunorubicin on cytotoxicity, cell cycle and DNA repair in acute lymphoblastic leukaemia. BMC Cancer. 2019; 19: 179.

113. Baek SH, Ohgi KA, Nelson CA, Welsbie D, Chen C, Sawyers CL, Rose DW, Rosenfeld MG. Ligand-specific allosteric regulation of coactivator functions of androgen receptor in prostate cancer cells. Proc Natl Acad Sci U S A. 2006; 103: 3100-5.

114. Koh SS, Li H, Lee YH, Widelitz RB, Chuong CM, Stallcup MR. Synergistic coactivator function by coactivator-associated arginine methyltransferase (CARM) 1 and beta-catenin with two different classes of DNA-binding transcriptional activators. J Biol Chem. 2002; 277: 26031-5.

115. Wu D, He J, Zhang W, Wang K, Jin S, Li J, Gao W. CARM1 promotes non-small cell lung cancer progression through upregulating CCNE2 expression. Aging (Albany NY). 2020; 12: 10578-10593.